An Experimental Investigation of the Burn Rates of Naturally Aspirated Spark Assisted Compression Ignition Combustion in a Single Cylinder Engine with Negative Valve Overlap

by

Laura Katherine Olesky

A dissertation submitted in partial fulfillment
of the requirements for the degree of
Doctor of Philosophy
(Mechanical Engineering)
in The University of Michigan
2013

Doctoral Committee:

Professor Margaret S. Wooldridge, Co-Chair
Provost Dionissios N. Assanis, Co-Chair, Stony Brook University
Professor André L. Boehman
Professor James F. Driscoll
Research Scientist George A. Lavoie
Assistant Research Scientist Jason B. Martz

For my family

Acknowledgments

First and foremost, I would like to thank Provost Dennis Assanis for having the original vision for the highly advanced engine test facility and for giving me the opportunity to conduct unique and interesting research. I would also like to thank Professor Margaret Wooldridge for her valuable guidance and support during the past year and for acting as co-chair of my commmittee. I am also grateful to Professor Jim Driscoll and Professor André Boehman for their insight and feedback.

During his two years at The University of Michigan, Dr. Jiri Vavra from Czech Technical University in Prague was an indispensable member of the Auto Lab team. I am grateful to him for sharing his technical knowledge and troubleshooting skills and for assisting in the collection of experimental data. I would like to thank Dr. George Lavoie and Dr. Aristotelis Babajimopoulos for the countless hours of productive and insightful discussion. Their support throughout this process has been instrumental. I would also like to thank Dr. Jason Martz for his unwavering guidance in the final stages of my degree. This work would not have been possible without his valuable input.

My fellow students have been an amazing source of support throughout my time at Michigan. I would especially like to thank Jeremy Spater and Peter Andruskiewicz, who took part in constructing the engine test cell, as well as Eric Bumbalough and Luke Hagen for their assistance in collecting data and in maintaining the experimental equipment. I am also grateful to Elliott Ortiz-Soto for his valuable improvements to the heat release code and Robert Middleton for his assistance in analyzing the experimental data. This work has been a real team effort, and I could not have done it without the selfless contributions of so

many others. Lastly, I would like to thank my family and friends for constantly believing in me, and my wonderful husband and best friend, Sam, for his steadfast love and support over the past six years.

Funding for this work was provided by the U.S. Department of Energy under contract DE-EE0000203, “A University Consortium on Efficient and Clean High Pressure Lean Burn (HPLB) Engines.”

Contents

List of Tables

Table

List of Figures

Figure

List of Abbreviations

η_{comb} in-cylinder combustion efficiency

η_{th} thermal efficiency

γ ratio of specific heats

ϕ 'fuel-to-air' equivalence ratio

ϕ' 'fuel-to-charge' equivalence ratio

φ 'fuel-to-O_2' equivalence ratio

AIT after (spark) ignition timing

BDC bottom dead center

BMEP brake mean effective pressure

c_p constant pressure specific heat capacity

CA crank angle

CA50 combustion phasing, crank angle at 50% MFB

CAD crank angle degree

CIDI compresssion ignition direct injection

COV coefficient of variation

DAQ data acquisition system

EGR exhaust gas recirculation

eEGR external EGR

iEGR internal EGR

EIVC early intake valve closing

EOC end of combustion

EVO/EVC exhaust valve opening/closing

FFVA fully-flexible valve actuation

HC hydrocarbon emissions

HCCI homogeneous charge compression ignition

$IMEP_g$ gross indicated mean effective pressure

$IMEP_n$ net indicated mean effective pressure

$ISFC_n$ net indicated specific fuel consumption

IVO/IVC intake valve opening/closing

m_{air} mass of air in-cylinder

m_{eEGR} mass of eEGR in-cylinder

m_{fuel} mass of fuel in-cylinder

m_{iEGR} mass of iEGR in-cylinder

MFB mass fraction burned

MMCD multi-mode combustion diagram

NO_x oxides of nitrogen

NVO negative valve overlap

PM particulate matter

PRR pressure rise rate

PVO positive valve overlap

RGF residual gas fraction

RI ringing intensity

RoHR rate of heat release

RTD resistance temperature detector

S_L laminar flame speed

SA spark advance

SACI spark assisted compression ignition

SI spark ignition

T_b burned gas temperature

T_{IVC} temperature at intake valve closing

T_u unburned gas temperature

TDC top dead center

aTDC after top dead center

bTDC before top dead center

TWC three-way catalyst

X_{EGR} mole fraction of EGR

X_{SCP} mole fraction of stoichiometric combustion products

Abstract

Homogeneous charge compression ignition (HCCI) combustion has received much attention in recent years due to the ability to reduce both fuel consumption and NO_x emissions compared to conventional spark-ignited (SI) combustion. However, the implementation of HCCI remains a challenge due to the limited operating range and lack of a direct ignition timing control mechanism. Spark assisted compression ignition (SACI) has been shown by several research groups, including the work presented here, to provide such a mechanism, helping to control the phasing and stability of a primarily auto-igniting charge, as well as providing a means of extending the high load limit of HCCI while maintaining high thermal efficiency. The approach used in this study is unique in that flexible engine valve timing allowed for independent control of the thermal/compositional stratification associated with a large internal residual fraction, allowing its effect to be isolated from other thermophysical parameters.

In these experiments, a single-cylinder research engine equipped with fully-flexible valve actuation was used to explore the effects of spark assist in controlling peak heat release rates. With spark assist, a small portion of the heat release occurred via flame propagation, increasing the overall duration of the combustion event and dramatically reducing peak rates of heat release. As a result, charge energy content and load were increased far beyond the limits of HCCI ($\sim$4 bar $IMEP_n$), up to $\sim$7.5 bar $IMEP_n$, while avoiding high rates of pressure rise. At each load level, pressure rise rates were modified through the careful control of spark advance, internal residual content of the charge (via negative valve overlap), and external exhaust gas recirculation (EGR) rates, thereby balancing the portions

of heat release due to flame propagation and heat release from auto-ignition. At higher load operation, the portion of flame propagation heat release was increased, resulting in a heat release profile that resembled traditional spark-ignited combustion.

Spark assist was also effective at modifying the heat release rates of stoichiometric SACI at constant load and combustion phasing with only slight changes in thermal efficiency. Peak heat release rates were dramatically reduced (up to $\sim$40%) by controlling spark timing and unburned gas temperature (T_u) via changes in internal and external EGR rates. Internal EGR was adjusted by varying the duration of negative valve overlap (NVO); for the range of NVO investigated, potential variations in in-cylinder mixing and thermal/compositional stratification were found to have a weak effect on burn characteristics, confirming the hypothesis that temperature and spark timing are the primary variables affecting SACI burn rates for a fixed mixture composition.

Other experiments focused on burn rate modification by controlling the unburned temperature and composition of the mixture (via changes in external EGR rates) at a constant spark advance. Variations in burn duration resulted primarily from the effect of deflagrative heat release on the rates of end-gas auto-ignition, contributing to a $\sim$24% reduction in peak heat release rates. In the experiments, heat release analysis showed that the behavior of SACI was consistent with the theoretical kinetics associated with turbulent flame propagation and auto-ignition, supporting the hypothesis that SACI is essentially two distinct energy release events coupled by the compression heating from an expanding flame front.

The results of this work provide new insights on the physical and chemical mechanisms important during low temperature combustion. The results confirm proposed representations of SACI, and therefore, provide direction for developing new advanced low temperature engine strategies.

Chapter 1
Introduction

This chapter reviews several low temperature combustion concepts to identify gaps within the literature and to discuss the benefits and shortcomings of previous studies. Recent experiments involving these concepts are summarized and current challenges are presented. Finally, the objectives for the work presented in this thesis are given.

1.1 HCCI Background

Homogeneous charge compression ignition (HCCI) is a novel combustion strategy being developed for use in future production-level internal combustion engines. In recent years, HCCI has received much attention due to its ability to reduce fuel consumption and emissions compared to premixed spark ignition (SI) and compression ignition direct injection (CIDI) combustion. Under stable operating conditions, premixed low temperature HCCI combustion results in high thermal efficiency with ultra-low emissions of nitrogen oxides (NO_x) and particulate matter (PM) [1, 2].

HCCI refers to the controlled auto-ignition of a highly dilute fuel-air mixture inside a relatively unmodified gasoline engine. As in an SI engine, the fuel and air are well mixed, and the mixture is compressed to its point of auto-ignition and burns without the aid of a spark discharge event, similar to a CIDI engine. Auto-ignition typically begins near top dead center (TDC) and the combustion process occurs rapidly, approaching ideal constant volume behavior. Optimal combustion phasing is achieved just after TDC, where maximum expansion work is obtained while minimizing compression work and heat transfer losses

[3]. Properly phased HCCI auto-ignition results in small cycle-to-cycle variations, whereas in SI engines, larger cyclic variations occur since the early flame growth period is subject to inhomogeneities in the vicinity of the spark plug and variations in flow conditions [4, 5].

In stoichiometric SI operation, the incoming equivalence ratio is held constant ($\phi = 1$) and load is controlled by throttling the intake flow to regulate the trapped masses of both fuel and air. This strategy results in elevated pumping losses and poor thermal efficiency, particularly at low loads. In contrast, dilute HCCI operates unthrottled and controls load by regulating only the injected fuel mass, allowing equivalence ratio to vary. Therefore, the pumping losses associated with throttled operation are avoided, increasing the net work output and efficiency of the cycle [6].

Although HCCI auto-ignition occurs rapidly, peak in-cylinder temperatures remain relatively low through high levels of charge dilution with excess air and/or recirculated combustion products, depending on engine design [7]. The lower peak temperatures elevate the ratio of specific heats (γ) of the burned mixture, leading to substantial gains in thermal efficiency. Heat loss through the cylinder walls is also reduced, providing further efficiency improvements [8]. In addition, thermal efficiency is enhanced by the use of an increased compression ratio (relative to spark-ignited engines) to promote auto-ignition and by the fact that combustion occurs at nearly constant volume due to the fast burn rates associated with auto-ignition [9].

The absence of high temperature regions in HCCI combustion also greatly reduces engine-out NO_x concentrations, allowing the engine to meet emissions regulations without NO_x after-treatment [6, 10]. High temperature regions and, hence, significant NO_x formation are unavoidable in conventional SI and CIDI due to near stoichoimetric conditions within the premixed and diffusion flames, respectively. However, when combined with a three-way catalyst (TWC) capable of treating the emissions from a stoichiometric fuel-air mixture, SI engines emit extremely low levels of NO_x, CO, and HC. At higher load HCCI operation, where peak temperatures increase and NO_x begins to form in significant concen-

trations, the fuel-air mixture can be made stoichiometric through the addition of external EGR, allowing for after-treatment with a standard three-way catalyst. The addition of EGR itself also aids in lowering the rate of NO_x formation by reducing both peak burned gas temperatures (due to its elevated heat capacity compared to air) and the concentration of O_2 in the reactant mixture [11]. HCCI also offers negligible levels of particulate emissions due to increased charge homogeneity and the absence of localized fuel-rich regions [12]. In CIDI, locally rich regions within the fuel jet lead to high levels of soot formation.

The first imaging experiments involving HCCI reported combustion occurring simultaneously at multiple locations throughout the combustion chamber, resulting in fast burn rates even at high levels of dilution. It was, therefore, established that the onset of combustion was dictated by chemical kinetics and lacked the reaction fronts seen in more conventional modes of operation [1, 2, 13–15]. Other studies reported a more sequential auto-ignition process, in which combustion began in the hotter core regions of the cylinder and was completed in the cool thermal boundary layer region near the cylinder wall [16, 17]. This sequential ignition behavior became even more pronounced as the wall temperature was decreased, resulting in an increased thermal gradient near the boundary layer [17]. It was thought that the rapid expansion of the initial burning zones promoted auto-ignition in the less reactive zones through compression heating, resulting in a very fast burn rate (5-15 crank angle degrees) despite its non-instantaneous nature [18]. In some cases, this sequential auto-ignition process can resemble reaction front-like structures propagating outward from the center of the combustion chamber [16].

1.2 Challenges of HCCI Combustion

1.2.1 Combustion Phasing Control

As mentioned previously, HCCI combustion phasing is not directly controlled by a spark or main fuel injection event as in SI and CIDI combustion, respectively. Rather, the on-

set of combustion is determined indirectly by the local thermodynamic state and reaction kinetics of the mixture [19]. Therefore, ignition timing and burn rate are often difficult to control, even for steady state operation. The thermodynamic state near TDC, which is extremely important in determining the phasing of HCCI combustion, depends greatly on the thermal state at intake valve closing (IVC) and the temperature-time history throughout the compression process. Depending on the compression ratio, additional preheating may be necessary to achieve the temperatures required for ignition and to avoid misfire.

Typically, the onset of auto-ignition is controlled by directly heating the intake charge [20] and/or by implementing advanced valve control strategies to retain hot combustion products in-cylinder [21]. However, due to the slow response time of heaters, the latter method is often preferred for systems which operate in a transient manner. The most common method of residual gas retention is a negative valve overlap (NVO) strategy, in which the exhaust valves close early during the exhaust displacement stroke, retaining hot residuals within the cylinder for the following cycle [22]. As the internal residual fraction increases, so does the initial temperature at IVC, leading to an earlier onset of auto-ignition.

The rates and overall behavior of HCCI auto-ignition are heavily tied to combustion phasing. As HCCI occurs earlier in the cycle, burn rates increase resulting in increased peak cylinder pressures and temperatures, rates of pressure rise, ringing, and NO_x emissions [23, 24]. In addition, if the mixture combusts too early, a majority of the pressure rise will occur during the compression stroke, heat transfer will increase, and the net work output will be reduced. Late combustion, on the other hand, leads to decreased burn rates, lower rise rates of pressure and temperature, and a reduction in the effective expansion work and thermal efficiency. Late ignition can also lead to unstable combustion, partially burned cycles, and engine misfire [25].

1.2.2 Side Effects of Negative Valve Overlap

From a practical standpoint, NVO is an attractive option for achieving elevated temperatures at IVC to promote HCCI auto-ignition. However, significant levels of NVO have also been shown to influence the combustion process by increasing the in-cylinder thermal and compositional stratification and the level of cycle-to-cycle variability, especially near the stability limit. For engines that use a large degree of NVO to control combustion phasing, the incoming charge and the residual gases are not necessarily well mixed. In an optical engine experiment by Rothamer et al. [26], it was shown that relative to HCCI combustion with conventional valve events and intake air preheating, the use of an NVO strategy produced a greater degree of in-cylinder thermal and compositional stratification due to insufficient mixing of the residual gases with the fresh charge. The local temperature was higher in the zones of greater residual concentration and auto-ignition began in these hotter regions. A comparable modeling study by Babajimopoulos et al. [27] drew similar conclusions. A greater level of thermal stratification could also increase the time between the ignition of various zones, resulting in longer burn durations for the HCCI cases under NVO operation [28]. Rothamer et al. [26], however, did not report how the observed changes in the in-cylinder stratification levels affected HCCI burn rates.

In a recent study, NVO was thought to contribute to engine instability by introducing a complex level of cycle-to-cycle feedback [29]. In a real engine, cycle-to-cycle variations are unavoidable. Even if the charge temperature at IVC is precisely controlled, cyclic variations in the charge temperature near TDC still occur due to turbulence, heat transfer, and differing levels of charge mixing [30]. In an engine operating with a large NVO, slight variations in the compositional and/or thermal state at IVC resulting from variations in residual gas temperature can significantly affect the phasing of subsequent cycles [31].

With larger amounts of NVO, the onset of ignition becomes increasingly affected by the properties of the residual gases and less so by the incoming conditions, which can be controlled more directly. This is especially true at the limits of combustion stability, where

an increased sensitivity to small variations in intake temperature was seen by Persson et al. [22]. For unstable HCCI combustion with a large NVO, combustion tends to oscillate between early and late phasings due to variations in residual gas temperature and composition, sometimes resulting in misfire [32]. Partially burned cycles are often followed by an advanced, heavily ringing cycle which is likely due to partially reacted fuel and excess oxygen contained in the residual of the partially burned cycle [29]. As such, it is preferable to avoid the stability limit (i.e. late combustion phasing) when operating HCCI with high levels of NVO. However, this leads to an even more limited window of HCCI operation, as discussed in the following section.

1.2.3 High Load Limitations

As mentioned previously, the ringing and instability constraints associated with excessively early or late combustion, respectively, result in a relatively narrow operating range for HCCI. As load increases, peak pressures and rates of pressure rise increase as well, and combustion must be retarded to comply with ringing limits [33, 34]. However, as load increases, the ringing and instability constraints converge, establishing a high load limit for this HCCI combustion mode, as seen in Figure 1.1 [25]. Beyond this limit, slight changes in in-cylinder conditions can lead to excessive pressure rise rates or misfire [35]. According to several experimental studies, the maximum achievable load for naturally-aspirated HCCI is about 4-5 bar $IMEP_g$ [35–38]. At this load condition, burned gas temperatures are typically high enough to form excessive NO_x emissions ($>$1 g/kg-fuel). On the other hand, at very low load operation, burned gas temperatures are too low for complete combustion, resulting in instability, misfire, and excess CO and HC emissions. Sjöberg and Dec [39] showed that peak temperatures must exceed 1500 K for completion of the CO to CO_2 conversion reactions.

In order to fully benefit from the efficiency gains provided by HCCI, the operating range must be expanded from that shown in Figure 1.1 to cover an increased portion of the speed-

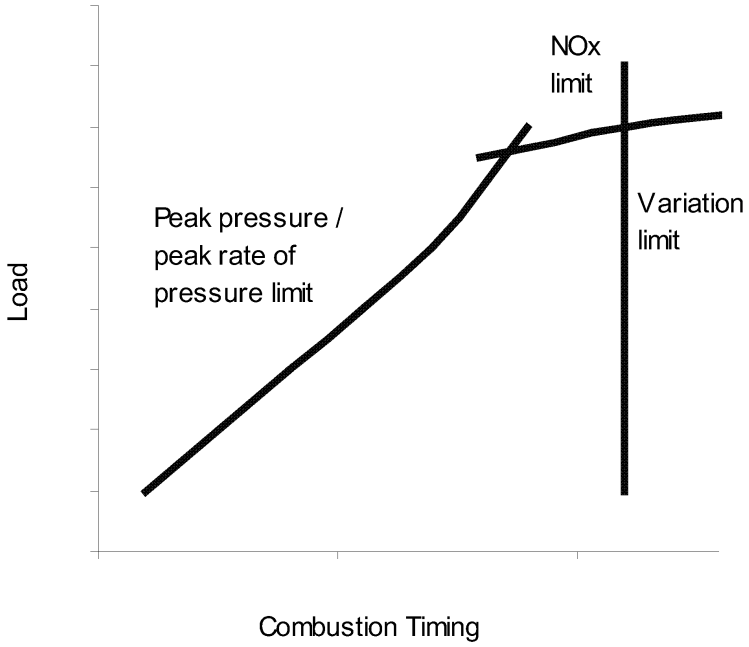

Figure 1.1: The pressure rise rate, combustion stability, and NO_x emissions limits of HCCI operation as depicted by Olsson et al. [25]

load map. In particular, the high load limit must be extended by reducing the maximum pressure rise rates at these conditions. To a certain extent, this can be accomplished by retarding combustion to lengthen the burn duration [30]. However, at the high load limit of HCCI, combustion cannot be retarded further without becoming severely unstable and/or misfiring, as shown conceptually in Figure 1.1.

Several HCCI load extension strategies have been attempted with varying levels of success, including the use of elevated intake pressures [35, 40, 41], thermal stratification [30], charge composition stratification [42], external EGR addition [11], and spark assisted compression ignition [43]. With boosted strategies, mixture dilution rates are elevated, resulting in low combustion temperatures and low exhaust temperatures that decrease the work output of the compressor, thus prohibiting further increases in intake manifold pressure. To compensate for the reduced enthalpy of the exhaust gases, the turbine nozzle flow area can be decreased, resulting in higher backpressures and increased pumping losses [44]. Despite this drawback, boosting is still quite effective at improving the high load capabilities

of HCCI, albeit at an efficiency cost. Olsson et al. [3] were able to achieve 16 bar BMEP in a multi-cylinder turbocharged HCCI engine with an absolute intake manifold pressure of 300 kPa. However, the same engine in a Diesel configuration produced 21 bar BMEP with an absolute thermal efficiency improvement of 5-10%. From a controllability standpoint, boosted HCCI is also at a disadvantage since it relies primarily on the state of the mixture near TDC to trigger ignition.

Sjöberg et al. [30] attempted to decrease the rates of HCCI combustion by lowering the coolant temperature, thereby increasing the in-cylinder thermal gradient near the wall. At a constant combustion phasing, it was found that lowering the coolant temperature from 100°C to 50°C lengthened the overall burn duration by less than 1° CA and decreased ringing intensity by 15%. However, due to increased heat losses, fuel consumption was increased by 0.5% in order to maintain $IMEP_g$. Retarding combustion phasing by 1° CA provided a greater reduction in ringing (23%) without the associated fuel penalty. This result indicated that combustion retard was a better potential means of HCCI load extension; however, it would require extremely precise control of the charge temperature at IVC to prevent unstable combustion, which could become particularly problematic during transient engine operation.

Cooled external EGR has also been evaluated as a potential mechanism for HCCI load extension. Dec [7] showed through simulation that the primary effect of external EGR on HCCI combustion rates was a thermal one. The elevated heat capacity (c_p) of EGR compared to air dilution produced lower end-of-compression temperatures, phasing combustion later in the cycle. At constant combustion phasing, EGR dilute mixtures exhibited slightly slower burn rates than air dilute mixtures. This behavior was attributed to the lower oxygen concentrations which slowed initial chemical reaction rates. Despite the burn lengthening effects of external EGR, the potential for load extension was minimal [11]. With EGR addition, a less than 10 kPa increase in the HCCI high load limit was observed. At intermediate load conditions, Olsson et al. [33] showed a negligible difference in the combustion rates

between EGR and air dilute mixtures at constant combustion phasing. Dec and Yang [35] recently used external EGR in conjunction with intake boosting to increase HCCI loads up to 16.3 bar $IMEP_g$ at an absolute intake manifold pressure of 325 kPa. Without external EGR, the compression temperatures could not be cooled sufficiently to retard combustion and, hence, ringing constraints were encountered once intake manifold pressures exceeded 180 kPaa. Sufficient charge cooling was only encountered through the implementation of external EGR.

Charge stratification studies have shown varying levels of success for increasing HCCI load limits. Aroonsrisopon et al. [42] reported marginal load improvements ($\sim$10%) for an optimized fuel injection timing at 90° before TDC. At this condition, emissions were slightly improved compared to a more homogeneous case. In another study, charge stratification effectively lengthened the high load limit to 16 bar BMEP, but at the cost of elevated particulate emissions [45].

Previous studies have shown varying levels of success in increasing overall burn durations (and hence load) in a purely auto-igniting combustion mode. Boosting the intake pressure appears to be highly effective at extending the high load limit of HCCI, yet this method is still limited in terms of controllability. An additional strategy has recently been considered for improving the controllability and usable load range of low temperature combustion. This strategy, known as spark assisted compression ignition (SACI), involves triggering HCCI combustion using a spark-ignited flame front. With SACI, an external ignition source controls the onset of combustion, allowing for more flexibility in the initial state of the mixture. Additionally, due to its multi-mode nature, SACI burn rates can be more effectively manipulated than those in pure HCCI.

1.3 SACI Background

Imaging studies of SACI combustion [46–48] in an engine suggest that the spark triggers SI-like flame propagation within a highly dilute, preheated mixture which then releases a portion of the available fuel energy. This flame front also introduces compression heating to the surrounding end-gas mixture (in addition to the rising piston), causing it to auto-ignite earlier that it would have without spark assist [49]. Since SI flame propagation is generally slower than bulk auto-ignition, overall burn durations increase, leading to dramatic reductions in peak rates of pressure rise and heat release rates, allowing load to be extended beyond the limits of pure HCCI auto-ignition while maintaining the high thermal efficiency of dilute low temperature combustion.

Many experimental engine studies involving SACI have focused on the aspect of load extension. Urushihara et al. [43] accomplished SACI by injecting a small amount of additional fuel near the spark plug, facilitating a propagating flame that increased cylinder pressure and temperature, thereby inducing auto-ignition in the surrounding homogeneous lean mixture. As a result, the pre-combustion temperatures necessary to achieve HCCI were reduced, and the engine was capable of operating at much higher loads (up to 6.5 bar $IMEP_g$) before the ringing limit was reached. The moderating effect of SACI on heat release was confirmed by Yun et al. [50], who found that spark assistance was crucial to reducing combustion noise at higher engine loads. Following the spark event, more gradual initial heat release (thought to be flame propagation) was seen, followed by auto-ignition of the remaining charge. Combustion noise was reduced by the increase in overall burn duration. Similar results were found by Szybist et al. [51], who used SACI to achieve loads up to 7.5 bar $IMEP_n$. Maximum cylinder pressure rise rates were controlled by spark timing, internal EGR, and late intake valve close (IVC) to reduce the effective compression ratio. Under lower load conditions, the combustion event was dominated by volumetric auto-ignition (similar to HCCI), while at higher loads, a larger portion of the heat release occurred during flame propagation, as in conventional SI. A more recent study by Yun

et al. [52] utilized a large positive valve overlap (PVO) to control residual concentration and SACI burn rates. Nearly 10 bar $IMEP_g$ was achieved by continuously retarding spark timing and combustion phasing as load increased.

Additionally, spark assist offers a more robust level of cyclic control for a primarily auto-igniting charge, increasing the applicability of advanced low temperature combustion in transient multi-mode engine operation. Production feasible engines could potentially implement stoichiometric SI at high loads and dilute SACI and HCCI at intermediate and lower loads in order to improve thermal efficiency relative to throttled SI. Wang et al. [53] also demonstrated that spark assist can improve the stability of gasoline HCCI near the misfire limit, while Hyvönen et al. [54] have shown that the spark is a valuable misfire prevention mechanism during a rapid mode transfer between HCCI and conventional SI.

1.4 The SACI Combustion Process

SACI is a process that in theory connects flame propagation and auto-ignition heat release primarily via a compression heating effect; it operates on the principle that deflagrative reaction fronts can be sustained in ultra-dilute mixtures ($\sim$30-60% dilution [36]) provided the unburned mixture temperature (T_u) is elevated by means of charge preheating (e.g. with intake heaters and/or hot residual gases) [55, 56]. Such highly dilute mixtures are not normally accessible with conventionally unheated SI combustion, as a lean limit exists at $\sim$30% air dilution ($\phi \approx 0.7$) [57]. These elevated unburned temperatures encourage auto-ignition in the end-gas, whereas high dilution rates limit adiabatic flame temperatures (T_b) and rates of end-gas combustion. This principle has been demonstrated both experimentally [50] and computationally [49].

At excessively dilute ($\sim$70%) low load conditions, it is thought that flame propagation cannot take place or the flame is too weak to have a significant impact on the phasing of HCCI combustion [49]. Several engine experiments have attempted to study the effects of

spark assist on highly dilute, pre-heated mixtures. Depending on the conditions examined, varying results were obtained on the effectiveness of spark assist. For example, Persson et al. [37] showed that the spark dramatically advanced the phasing of mid-load ($\sim$3.4 bar $IMEP_n$) HCCI operation, whereas no advance in combustion phasing was seen for lower load operation ($\sim$2.0 bar $IMEP_n$). Wang et al. [58] showed that spark assist had a drastic effect on HCCI combustion at $\sim$4.0 bar $IMEP_n$; however, the spark offered almost no benefit for lower load conditions ($\sim$2.8 bar $IMEP_n$), as seen by Weinrotter et al. [59]. Kopecek et al. [60] found that an ignition event at 40° before TDC was able to advance HCCI combustion at $\phi = 0.43$; however, the ignition source had no effect on equivalence ratios below $\phi = 0.37$. Zigler [46] also noticed that the effects of spark assist on HCCI combustion varied with equivalence ratio for mixtures diluted with preheated intake air. For a constant preheat temperature of 270°C, spark assist had little impact on engine performance when the equivalence ratio was set to $\phi = 0.56$. However, at a slightly higher equivalence ratio ($\phi = 0.62$), i.e. fueling rate, spark assist appeared to have a much larger effect on phasing. Below $\phi = 0.38$, spark assist did not appear to have much of an effect on HCCI combustion behavior. Additional imaging data confirmed that, for equivalence ratios greater than $\phi = 0.36$, reaction front-like structures were formed following a spark ignition event [59].

SACI imaging data from Zigler et al. [46] showed reaction fronts propagating outward from the spark plug at average speeds between 1.9 and 4.3 m/s. These values agreed well with the expansion rates seen in an imaging study by Persson et al. [47], who reported 2-D reaction front perimeter expansion speeds of 2.5-10 m/s. In this study, as negative valve overlap (NVO) was increased, auto-ignition occurred more readily as a result of higher temperatures in the end-gas. However, initial flame front expansion rates decreased, possibly due to the increased levels of residual dilution. Zigler [46], on the other hand, saw an increase in reaction front propagation rates as the temperature of the end-gas was increased by more intense levels of charge preheating. However, for a constant intake temperature, propagation rates decreased as the spark timing was advanced, consistent with the decrease

in temperature at the time of spark. The data also suggested that auto-ignition of the end-gas occurred as a result of compression heating by the expanding reaction front, leading to a more consistent location of auto-ignition. Local auto-ignition sites, which formed initially in the unburned volume outside the boundary of the reaction front, seemed to appear with increasing frequency as the unburned gas temperature was increased by means of intake air heating.

SACI differs from conventional SI in that elevated unburned gas temperatures (T_u) are purposely used to achieve flame propagation within a highly dilute mixture, as well as ensure end-gas auto-ignition. This multi-mode combustion behavior is reflected in the overall shape of the global heat release rate seen in typical SACI experiments [47, 48, 50, 51]. The initially slow heat release rates (characteristic of deflagration) become much more rapid near the onset of auto-ignition, once the end-gas has been compressed to its ignition temperature. Zigler et al. [46] also showed that spark-ignited reaction fronts formed well before significant heat release was observed.

1.4.1 Multi-Mode Combustion Diagram (MMCD)

A modeling study by Lavoie et al. [49] attempted to define the regions where SI flame propagation, SACI, and HCCI combustion occur, in terms of unburned (T_u) and burned (T_b) gas temperatures near top dead center. This multi-mode combustion diagram (MMCD), seen in Figure 1.2, separates these combustion regimes for an iso-octane air mixture in terms of T_u and ϕ' (defined below) at TDC. In reality, the separation between the different modes is not so discrete (for example, the HCCI and SACI zones overlap slightly as flames are sustainable for $\phi' \approx 0.4$). However, the MMCD provides a conceptual representation of the boundaries associated with each mode.

In the MMCD, unburned temperature T_u is defined as the temperature that would be achieved if the mixture was compressed isentropically to TDC. This temperature depends on the compression ratio and the properties of the mixture at intake valve closing (IVC),

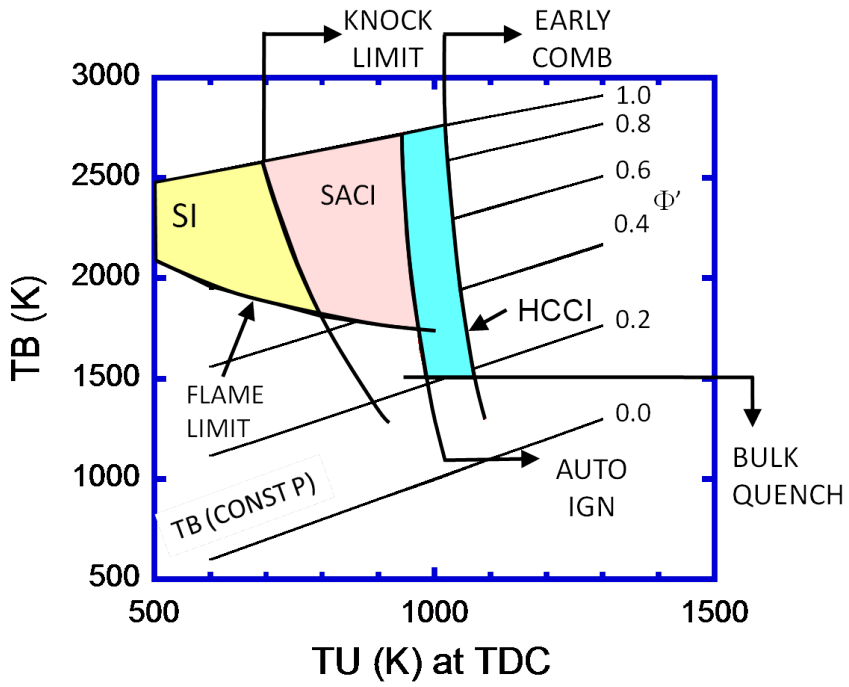

Figure 1.2: Multi-mode combustion diagram of Lavoie et al. [49] depicting the SI, SACI, and HCCI combustion regimes

including pressure, temperature, and composition (masses of fuel, air, and EGR). The MMCD is generated for a constant pressure condition, in this case TDC pressure at the end of an isentropic compression process.

The variable ϕ', also called the 'fuel-to-charge' equivalence ratio, is used as a primary load metric for air and/or EGR diluted mixtures and is defined in Equation 1.1.

$$\phi' = \frac{\frac{F}{A+R}}{\left(\frac{F}{A}\right)_{ST}} = \frac{\phi \cdot (1 - RGF)}{1 + RGF \cdot \phi \cdot \left(\frac{F}{A}\right)_{ST}} \approx \phi \cdot (1 - RGF) \tag{1.1}$$

In Eq. 1.1, the masses of fuel, air, and residual are denoted by F, A, and R respectively, and ϕ is the 'fuel-to-air' equivalence ratio, which is equal to 1 for the conditions in Figure 1.2. The subscript ST denotes stoichiometric conditions. RGF is the total residual fraction, which can include both internal and external EGR. The approximation holds because the stoichiometric fuel-air ratio is $\sim$0.07, resulting in a denominator close to 1. Essentially, ϕ'

is a measure of the specific energy of the charge (the amount of fuel compared to air and/or residual gases) and approximates $IMEP_g$ well for a naturally-aspirated engine operating under dilute conditions [49]. If ϕ is equal to 1, ϕ' provides a measure of the fraction of EGR dilution, and for purely air dilute mixtures, ϕ' is equal to ϕ. Once T_u and ϕ' are known, the corresponding T_b (i.e. the adiabatic flame temperature) is obtained from constant pressure equilibrium calculations, shown for a TDC pressure of 40 bar in Figure 1.2.

The bulk quench line corresponds to a T_b of 1500 K (about 80% dilution for the HCCI regime), below which Sjöberg and Dec [39] have noted insufficient CO to CO_2 oxidation during HCCI combustion and Huang et al. [55] have seen quenching of laminar flames due to radiative heat losses. The flame limit line is drawn for laminar burning velocities ranging from 10-15 cm/s, corresponding to experimental engine limit conditions reported by Flynn et al. [61] and Lavoie and Blumberg [62], while the knock limit line is defined as the T_u where constant volume combustion isentropically compresses the end-gas to 1000 K, the approximate temperature of auto-ignition. The auto-ignition line (corresponding to late phased HCCI combustion) and the early HCCI combustion line (corresponding to the ringing limit) are obtained with the ignition delay correlation of He et al. [63] for a combustion phasing interval of $\sim 10^\circ$ CA near TDC. These HCCI ignition boundaries fall around 1000 K and approximately define an operating region for pure auto-ignition based on the ringing and stability limitations.

As seen in Figure 1.2, HCCI requires high unburned gas temperatures to initiate auto-ignition and has relatively low burned gas temperatures up to the high load limit, which has been shown to occur at $\phi' \approx 0.45$ [35]. Conventional SI can be accomplished with lower unburned gas temperatures, but produces high burned gas temperatures given its elevated ϕ'. SACI can be used when unburned gas temperatures are too low to initiate auto-ignition through piston compression alone (but high compared to conventional SI) and the mixture is too dilute to produce the T_b necessary for conventional SI flame propagation. Under these dilute conditions, a flame can be sustained when unburned gas temperatures are increased

by means of a higher compression ratio, intake charge temperature, or internal residual fraction [64]. With SACI, flames and auto-ignition co-exist in varying proportions. The SACI regime should range from flame propagation with borderline end-gas 'knock' to auto-ignition initiated by a weak flame kernel. Limited experimental flame speed data exists within this theoretical SACI region ($T_u \geq 800$ K and $\phi' \leq 0.65$) and thus, this area is of particular interest for exploration within an engine setting.

1.4.2 Potential Efficiency Advantages of SACI

A recent computational study by Lavoie et al. [65] attempted to quantify the potential efficiency benefits of dilute combustion strategies (HCCI, SACI) over conventional SI combustion. Figure 1.3a from [65] compares the gross indicated and brake thermal efficiencies of air and EGR diluted combustion for various levels of ϕ' in a naturally-aspirated 4-cylinder gasoline direct-injected engine with a compression ratio of 12:1. For the EGR diluted cases, the 'fuel-to-air' equivalence ratio was fixed at $\phi = 1$. In terms of gross indicated thermal efficiency, an increase in dilution level (decrease in ϕ') is advantageous due to changes in chemical composition and a decrease in burned gas temperature. Both of these effects increase the ratio of specific heats (γ) of the unburned and burned mixtures, leading to gains in gross indicated thermal efficiency for increased levels of dilution. This effect is seen to be slightly greater for air dilution compared to EGR dilution. The curves drop rapidly for mixtures rich of $\phi = 1$ due to incomplete combustion.

Friction losses become important at low loads as the work done by the gas on the piston approaches the work performed to overcome friction. (Friction does not decrease proportionally with peak pressure and load, and thus becomes more dominant for highly dilute mixtures.) As a result, the inherently low mechanical efficiency of low load operation starts to outweigh the benefits of dilute operation on an indicated basis. Thus, the brake efficiency curve is low for very dilute mixtures and rises to a maximum in the mid-load range before falling again as the mixture becomes fuel-rich [65].

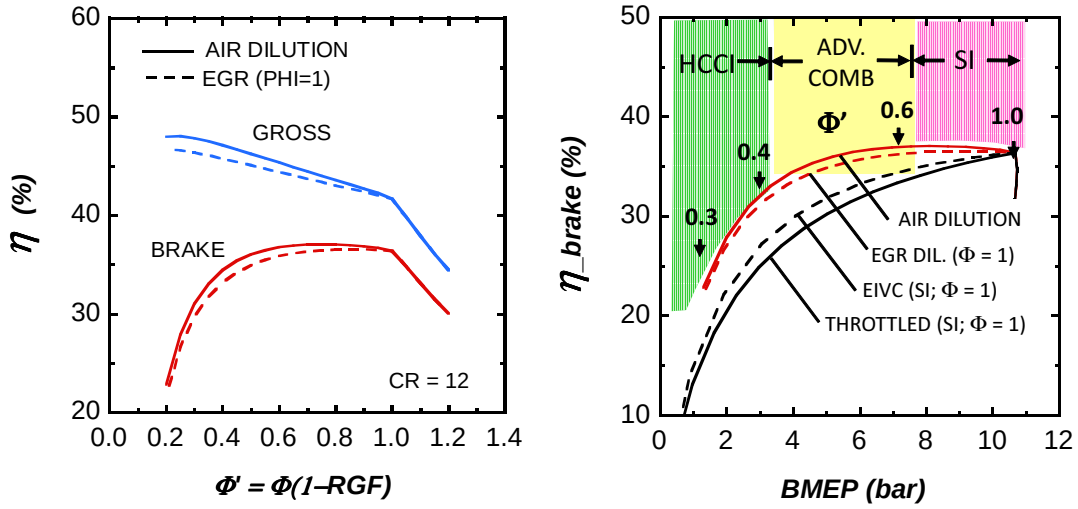

(a) Effect of ϕ' on efficiency η [65]

(b) Comparing load control methods [65]

Figure 1.3: (a) Effects of air and EGR dilution on gross indicated and brake thermal efficiencies as a function of the 'fuel-to-charge' equivalence ratio ϕ' and (b) potential gains in brake thermal efficiency for naturally-aspirated dilute multi-mode (HCCI, SACI, SI) engine operation as opposed to throttled or early IVC SI operation [65]

Figure 1.3b compares the brake thermal efficiencies for four methods of load control for a naturally-aspirated engine, including dilution with air, dilution of a $\phi = 1$ mixture with EGR, and a stoichiometric fuel-air mixture controlled by throttling or early intake valve closing (EIVC). The sharp drop in efficiency at high loads is due to the inclusion of rich conditions. Throughout the load (ϕ') range, dilute operation is predicted to be far more efficient than the other two methods, not only because pumping work is reduced, but because maximum in-cylinder temperatures are kept relatively low. These low maximum temperatures result in a higher γ mixture and, hence, greater expansion stroke work as a fraction of the available fuel energy. A lower maximum temperature also corresponds to lower heat losses to the cylinder walls. The throttling and EIVC cases maintain high peak temperatures because these methods do not involve significant dilution. In Figure 1.3b, the difference in brake thermal efficiency between the EIVC and throttled strategies is caused primarily by differences in pumping work.

An approximate scale of ϕ' is given above the topmost curve and applies only to the two

dilution cases. (For the throttled and EIVC cases, both ϕ and ϕ' are equal to 1.) This scale is used to divide the diagram into combustion mode regimes based on current knowledge. The HCCI range is limited to $\phi' < 0.4$ due to the appearance of excessive pressure rise rates and NO_x emissions at elevated fueling rates [35]. On the other hand, the lean limit for SI combustion corresponds to $\phi' < 0.7$ [57]. At higher levels of dilution, SI flame propagation becomes too slow for reliable combustion. As a result of these constraints, there is a gap between $\sim$0.4 and $\sim$0.7 in which it is difficult to operate with SI or HCCI combustion. In theory, SACI combustion can traverse this gap through careful control of unburned gas temperature for a given dilution rate. NO_x emissions in this regime will likely be too high to not go untreated; fortunately, EGR dilution at $\phi = 1$ is nearly as efficient as pure air dilution, and this strategy allows for after-treatment with a three-way catalyst.

1.4.3 Premixed Turbulent Flame Propagation

The SI combustion process in an engine takes place in a turbulent flow field. During ignition, the spark discharge produces a small flame kernel which undergoes a brief transition from a laminar flame to a turbulent flame. Turbulence affects the flame front almost immediately after the spark kernel is formed. The early flame development period lasts $\sim$1 ms following the spark event, after which fully developed flame propagation begins with turbulence acting as the primary rate control factor [66]. To gain insight into the structure of turbulent SACI flames, it is important to attempt to understand the interactions between laminar flame structure and the turbulent flow field.

The experimental literature suggests that the internal structure of thin laminar flames is not significantly altered by the turbulent flow field, provided the flames are not extinguished or quenched. For large turbulence intensities, it has been seen that the flame surface area increases, but its internal structure is not significantly altered, and the average preheat zone thickness is measured to be no larger than the laminar value [67, 68]. Reaction layers remain thin and sheet-like, even if the flame surface area is highly wrinkled, and this behavior

has been observed for a variety of fuels and equivalence ratios [69].

Filatyev et al. [70] found that increasing the turbulence level increased the global flame consumption speed by a factor of four, corresponding to approximately a fourfold increase in the ratio of the turbulent to laminar flame 2-D perimeters, $(P_T/P_L)^2$. These findings indicate that the turbulent burning velocity is directly related to the turbulent flame area through wrinkling of the laminar flame structure (i.e. S_T/S_L is approximately equal to A_T/A_L). Outside the 'thin flamelet' regime, where quenching occurs, this relationship does not necessarily hold. Ratner et al. [71] used a burner with large coflow air velocities to achieve very high turbulence intensities. The images they obtained showed thin reaction layers that became 'shredded' due to local extinctions, thus providing experimental evidence to support laminar flamelet modeling concepts. Roberts et al. [72] propagated a laminar flame over a strong vortex and found that larger eddy sizes were more effective at causing local flame extinctions than smaller ones. Very small eddies are quickly dissipated through viscous forces and are likely too weak to perturb the flame [69]. Thin flames were also found to exist at much higher levels of turbulence than previously thought [72].

Based on the available experimental flame data, the SACI flames presented in this document are assumed to have the same internal structure as thin laminar flames, wrinkled and stretched by turbulence. As such, the turbulent burning velocities of the SACI flames immediately following ignition (where wrinkling by turbulence is expected to be minimal) should exhibit the same trendwise behavior as the laminar burning velocities at similar flow field conditions. In addition, the initial turbulent flame growth rates are expected to be reflected in the early burn rates of the combustion event, as was seen by Aleiferis et al. [73]. Provided these SACI flames are not quenched by turbulence, they are expected to propagate outward from the center of the combustion chamber at a rate dictated partially by laminar flame chemistry, eventually promoting auto-ignition of the end-gas via compression heating.

1.5 Research Objectives and Document Organization

Many experimental and computational studies involving SACI and dilute flame propagation exist in the literature, yet there are still many unanswered questions regarding this combustion regime. While several experimental studies [50–52] have shown that load extension beyond the limit of HCCI is possible with SACI, few have attempted to provide fundamental insight into the primary mechanisms affecting SACI burn rates. While it is widely hypothesized that auto-ignition is triggered primarily by compression heating from the flame, few studies have attempted to directly isolate the effects of various parameters, such as thermal/compositional stratification and dilution method, on the flame/auto-ignition heat release tradeoff. Within the literature, the method of dilution has varied considerably between experimental studies. Some studies have focused on lean air dilute cases [74] while others have focused on stoichiometric EGR dilute cases [36, 50, 51]. Hence, the effect of diluent composition on SACI combustion behavior is relatively unknown.

The studies presented in this thesis expand considerably on previous efforts to gain fundamental insight into the effects of various controllable parameters (i.e. spark timing, temperature, and mixture composition) on the deflagrative and auto-ignition processes of SACI combustion. These experiments are the first to demonstrate a high level of control in isolating particular engine variables to gain a better understanding of their effects on overall SACI burn rates.

1.5.1 Objectives

The practical objectives of this research include the following:

- Experimentally demonstrate the advantages of SACI (over HCCI and SI) in terms of controllability, load extension, and thermal efficiency, and show that it can be used as a pathway of transition from low load HCCI auto-ignition to high load SI flame propagation, providing a practical means for implementing low temperature

combustion during a realistic drive cycle.

- Experimentally demonstrate independent control of SACI combustion phasing and burn rate through the simultaneous variation of *only* two engine control parameters (e.g. spark timing, unburned gas temperature, and/or mixture composition), thereby addressing one of the major shortcomings of HCCI.

Additional scientific objectives include identifying the fundamental mechanisms important during SACI combustion, as well as:

- Provide a more quantitative understanding of the physical and chemical processes governing the rates of SACI flame propagation and auto-ignition and, hence, overall burn durations.

- Isolate and understand the effects of potential temperature and compositional non-uniformities associated with the use of NVO and internal EGR on SACI burn rates.

- Gain insight into the effects of diluent composition (air vs. EGR) on the rates of SACI combustion.

The approach used to accomplish these objectives involves the careful control of experimental variables that affect flame propagation and auto-ignition in an engine setting. SACI burn rates are analyzed in terms of the tradeoff between flame propagation and auto-ignition heat release and the fundamental mixture properties obtained from an advanced two-zone heat release analysis.

1.5.2 Organization

The document is organized as follows:

- Chapter 2 introduces the experimental engine setup and outlines the two-zone heat release code used for data analysis. Primary sources of error and the expected magnitudes of experimental variation are discussed.

- Chapter 3 demonstrates how the combined deflagrative/bulk heat release of SACI can be used to extend engine load far beyond the limits of naturally-aspirated HCCI by manipulating overall burn duration and pressure rise rates at a constant combustion phasing. Load extension is accomplished via careful control of T_u (using a combination of internal and external EGR) and spark timing as the 'fuel-to-charge' equivalence ratio ϕ' increases. Combustion phasing is manipulated via spark advance.

- In Chapter 4, the ratio of flame propagation to auto-ignition heat release is manipulated at constant combustion phasing and load through the simultaneous variation of T_u and spark timing, thereby decreasing overall SACI burn rates and peak heat release rates. Changes in SACI behavior at these conditions are consistent with variations in estimated laminar flame speed near the time of spark and a nearly constant unburned gas temperature at the onset of end-gas auto-ignition. It is shown that potential changes in thermal and compositional stratification provided by varying levels of NVO have little effect on overall SACI heat release rates.

- In Chapter 5, the effect of mixture composition on SACI burn rates is studied. The ratio of flame propagation to auto-ignition heat release is manipulated at constant phasing through the simultaneous variation of EGR fraction and unburned gas temperature T_u. Despite an elevated T_u, mixtures with a higher EGR fraction exhibit slower initial heat release rates, consistent with a decrease in estimated laminar flame speed near the time of spark. Estimated unburned gas temperatures at the onset of auto-ignition are approximately constant, affirming temperature as the primary factor controlling bulk heat release rates.

- Finally, summaries and conclusions, contributions, and recommendations for future work are presented in Chapter 6.

1.6 Relevant Publications

The topics in this dissertation have also been reported in the following publications:

1. **L. Manofsky**, J. Vavra, D. Assanis, and A. Babajimopoulos. "Bridging the Gap between HCCI and SI: Spark-Assisted Compression Ignition". *SAE Technical Paper 2011-01-1179*. 2011.

2. J. Vavra, S. V. Bohac, **L. Manofsky**, G. Lavoie, and D. Assanis. "Knock in Various Combustion Modes in a Gasoline-Fueled Automotive Engine". *Journal of Engineering for Gas Turbines and Power* 134 (2012), 082807.

3. **L. M. Olesky**, J. Vavra, D. Assanis, and A. Babajimopoulos. "Effects of Charge Preheating Methods on the Combustion Phasing Limitations of an HCCI Engine with Negative Valve Overlap". *Journal of Engineering for Gas Turbines and Power* 134 (2012), 112801.

4. **L. M. Olesky**, J. B. Martz, G. A. Lavoie, J. Vavra, D. N. Assanis, and A. Babajimopoulos. "The effects of spark timing, unburned gas temperature, and negative valve overlap on the rates of stoichiometric spark assisted compression ignition combustion". *Applied Energy* 105 (2013), 407-417.

Chapter 2

Experimental Setup and Analytical Methods

This chapter introduces the FFVA single-cylinder research engine and its unique capabilities. The enormous flexibility of this setup is critical for designing experiments that will provide fundamental insight into the behavior of SACI combustion. Key experimental hardware, instrumentation, and analysis methods are described along with the results of repeatability analysis.

2.1 Experimental Setup

All experiments are performed on a single-cylinder gasoline direct-injected research engine with a Ricardo Hydra crankcase. The engine is equipped with a fully-flexible valve actuation (FFVA) system, allowing a large fraction of internal EGR to be retained using negative valve overlap (NVO). The engine also has an external EGR loop through which cooled exhaust gases are recirculated into the intake manifold. A detailed schematic of the engine is seen in Figure 2.1.

The engine geometry is listed in Table 2.1. The compression ratio for this engine (12.5:1) is higher than that for a typical spark-ignited engine. This feature creates higher in-cylinder pressures and temperatures, aiding in the implementation of HCCI auto-ignition. The piston contains an asymmetrical bowl for increased cylinder turbulence and reciprocates below a pent-roof type combustion chamber. Fuel is delivered via a gasoline direct

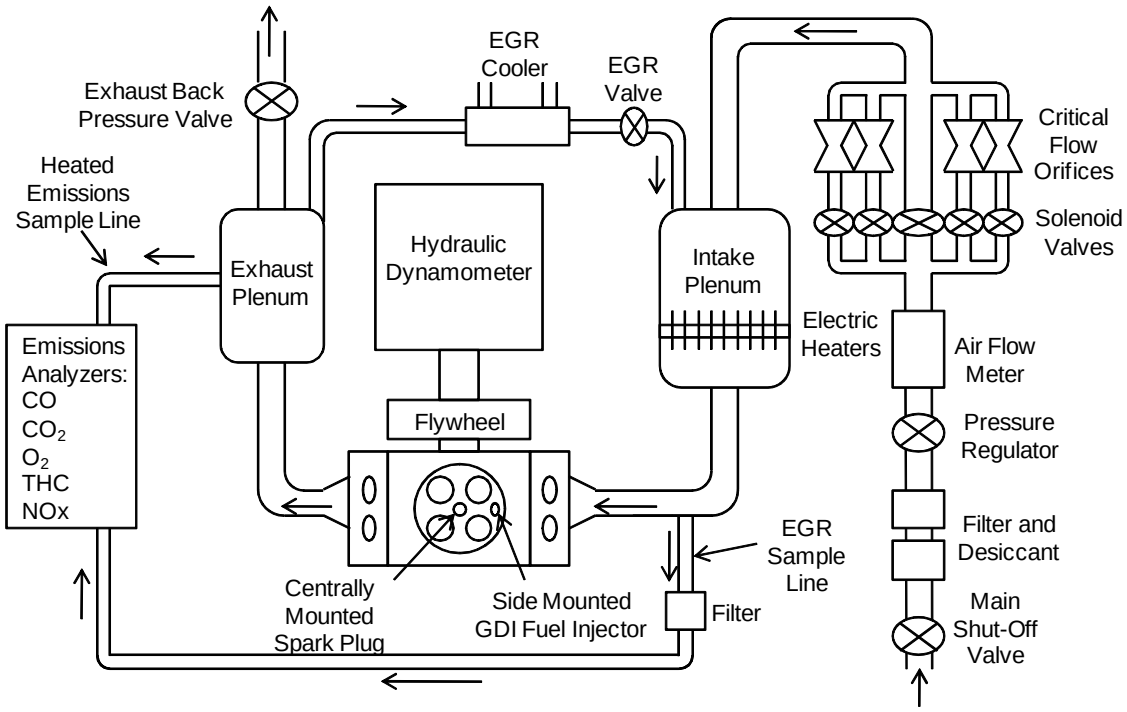

Figure 2.1: FFVA engine schematic

Parameter	*Value*
Displaced volume (cm^3)	550
Number of cylinders	1
Stroke (mm)	94.6
Bore (mm)	86.0
Connecting rod length (mm)	156.5
Piston pin offset (mm)	0.8
Compression ratio	12.5:1
Number of valves	4

Table 2.1: Engine geometry

injector mounted between the two intake valves and aimed into the piston bowl. A spark plug is centrally mounted in the cylinder head.

2.1.1 FFVA System

The electro-hydraulic valve actuation system (designed by Sturman Industries) allows the lift, timing, and duration of each valve event to be controlled independently. The system is capable of running two intake events and two exhaust events per engine cycle, at lifts up to 10.0 mm. The range of possible valve timings is limited only by physical interference between the piston and the valves, preventing large amounts of positive valve overlap (PVO) from being achieved. Specifications for the FFVA system are given in Table 2.2.

Specification	*Details*
Manufacturer	Sturman Industries
Principle of operation	Electro-hydraulic
Number of valves	4
Maximum lift (mm)	10.0
Resolution of lift control (mm)	0.1
Resolution of timing control (CAD)	1.0
Maximum number of valve events per cycle	2
Variation in valve events (CAD)	$\pm$ 2

Table 2.2: Electro-hydraulic valvetrain specifications

The lift of the primary valve event is controlled by an internal hard stop mechanism which gives the valve profiles a trapezoidal shape, atypical of conventional cam-driven systems. Due to physical limitations, the position of the hard stop cannot be changed mid-cycle, so valve lift and timing can only be varied on a cycle-resolved basis. In all experiments, a recompression valve strategy was used. Recompression relies on a high degree of negative valve overlap (NVO) to retain hot residual gases in the cylinder. For these experiments, the NVO is controlled by adjusting EVC and IVO symmetrically around TDC, which allows for maximum recovery of the compression work with minimal gas forced inside the intake manifold [75]. Throughout the experiments, the locations of IVC

and EVO are held constant, allowing the effective compression and expansion ratios to remain fixed. Sample valve traces with the resulting recompression pressures are depicted in Figure 2.2, where the arrows represent the direction of increasing NVO.

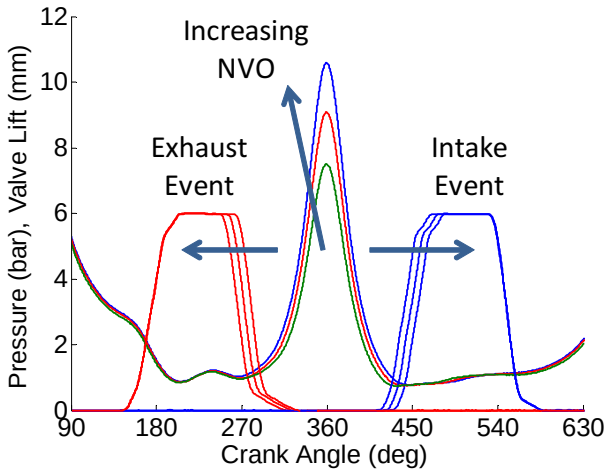

Figure 2.2: Valve lift and cylinder pressure traces for a recompression (i.e. NVO) valve strategy

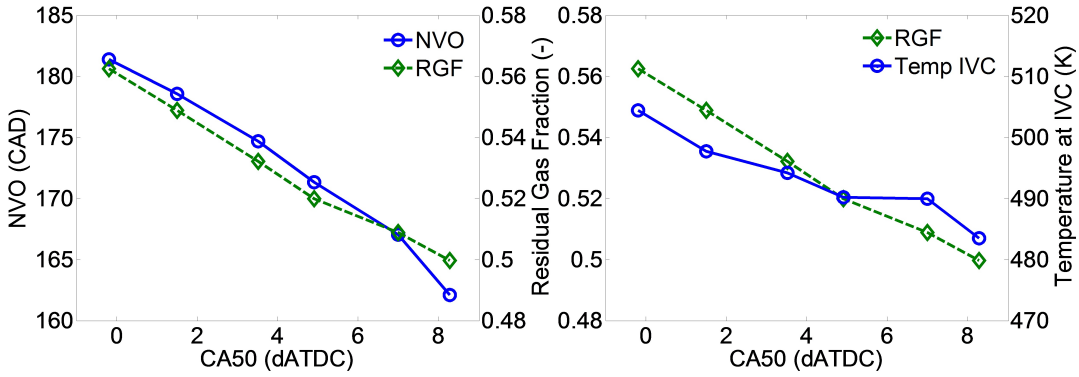

Figure 2.3: Variation in residual gas fraction and cylinder temperature at IVC as NVO decreases and CA50 retards

For a given intake pressure and fueling rate, an increase in NVO increases the fraction of residual gases in the cylinder. These hot residuals increase the compression temperature of the mixture and its tendency to auto-ignite, thus advancing the timing of ignition. As a result, the location at which 50% of the fuel mass is burned (CA50), also known as the

combustion phasing, advances. Figure 2.3 show this advance in CA50 for an increase in NVO, residual gas fraction, and temperature at IVC for HCCI combustion at $\sim$3 bar $IMEP_g$ and a fueling rate of 10 mg/cycle.

2.1.2 Fuel and Air

The fuel used in the experiments was 87-octane research-grade gasoline. Fuel specifications are listed in Table 2.3. The fuel system consists of a solenoid-type direct injector and a large bladder accumulator which is pressurized with nitrogen up to $\sim$100 bar. Fuel flow is regulated by specifying the fuel injector driver pulse width duration within LabView-based engine control software. Start of injection is set to 330° before TDC, giving the charge sufficient time to mix before ignition.

Parameter	*Value*
Research octane number (RON)	90.5
Motor octane number (MON)	82.6
Antiknock index (R+M)/2	86.6
Carbon (Wt. %)	86.38
Hydrogen (Wt. %)	13.62
Oxygen (Wt. %)	0.0
H/C atomic ratio	1.879
Stoichiometric air-fuel ratio	14.61
Lower heating value (MJ/kg)	43.043
Specific gravity	0.7448
Grabner vapor pressure (kPa)	48.1
Molecular weight (g/mol)	93.039

Table 2.3: Fuel specifications

The engine is supplied with compressed shop air which is regulated upstream of the intake plenum to achieve the desired intake pressure (measured in the intake runner). The system is capable of running slightly boosted pressures; however, intake pressure is typically limited to an unthrottled 1.0 bar absolute. Three electric heaters inside the intake plenum can be used to heat the intake charge to a maximum temperature of $\sim$130°C. A butterfly valve downstream of the exhaust plenum, seen in Figure 2.1 is used to regulate

the exhaust manifold pressure and the flow of external EGR into the intake manifold. The exhaust pressure is typically maintained at $\sim$5 kPa above the intake pressure. Large adjustments in EGR flow rate are made by opening/closing a needle valve in the EGR line. A water-cooled heat exchanger in the EGR line regulates the temperature of the incoming exhaust gases. The EGR coolant temperature is typically set to 55-60°C, while the engine coolant temperature is set to 90°C using a separate cooling system.

An array of critical flow orifices and a thermal mass flowmeter are used to measure the air mass flow rate into the engine. Fuel flow rate is measured with a piston-type positive displacement flow meter. A Bosch LA4 wide range oxygen sensor mounted in the exhaust manifold is used to determine the 'fuel-to-air' equivalence ratio ϕ.

Full exhaust constituents are measured with a Horiba MEXA emissions analysis system. Gases are probed in the exhaust plenum and transferred to the various analyzers via a heated line, where molar fractions of NO_x (chemiluminescence), HC (flame ionization), CO, CO_2 (non-dispersive infrared), and O_2 (paramagnetic) are measured. The 'fuel-to-air' equivalence ratio ϕ is also determined from calculations involving these quantities [76] and good agreement ($<$ 2-3%) is typically seen with the LA4 sensor. In addition, the CO_2 concentration within the intake manifold is measured and the external EGR fraction is calculated from the ratio of volumetric CO_2 in the intake and exhaust manifolds. In these experiments, the external EGR is introduced upstream of the intake plenum and thus, the incoming air and external EGR are expected to be well mixed.

2.1.3 Engine Control and Data Acquisition

A hydraulic dynamometer from Electro-Mechanical Associates is used to provide load and regulate engine speed. The engine's crankshaft is mechanically connected to a hydraulic motor which is connected to a large pump via hydraulic lines. A Hall effect sensor is used to measure the engine speed; for all experiments, the engine speed was held constant at 2000 rpm. The engine controller is composed of hardware from National Instruments and

Drivven, Inc. LabView-based software provided by Drivven was developed for the current setup. Spark dwell, spark timing, and fuel injection timing and duration are controlled by Drivven spark and fuel injector drivers.

The spark plug is fired by a MoTeC M DEN-580 inductive smart coil, which is capable of only one ignition event per cycle. The coil is mounted just above the engine head, and a short spark plug wire and boot connect the coil to the plug terminal. The maximum energy storage of the coil is $\sim$70 mJ, and for all experiments, the maximum coil energy was implemented. A current transformer surrounding the spark plug wire is used to measure current flow and to determine the timing and duration of the ignition event. The current trace indicates that the duration of the spark plasma is approximately 10° CA at 2000 rpm. The low-speed data acquisition system (DAQ), also based on National Instruments hardware and LabView, provides signal conditioning for flow rates and temperatures measured with thermocouples and RTD sensors. Measured parameters include oil and coolant temperatures, fuel and air mass flow rates, and gas temperatures at the intake and exhaust ports.

Cylinder pressure data is typically sampled at 0.1° CA resolution for 200 consecutive cycles using a Kistler model 6125A piezoelectric pressure transducer with a perforated flame shield which is pegged once per cycle near bottom dead center (BDC) from a dynamic piezoresistive absolute pressure sensor (Kistler model 4007B) mounted near the intake port. It has been shown experimentally that the use of a flame shield improves the sensor thermal characteristics by preventing hot burned gases from contacting the transducer face [77]. Absolute exhaust pressures are measured with an additional dynamic piezoresistive sensor (Kistler model 4045A) positioned in the exhaust runner. This sensor is mounted in a cooled switching adapter which helps to protect it from overexposure to high exhaust temperatures. These pressure signals, as well as the valve lift signals from the Sturman controller unit, are recorded by an AVL high-speed combustion analysis system. A Kistler model 2613B crank angle encoder allows the high-speed system to maintain synchronization with the engine crank position.

2.2 Heat Release Analysis

Heat release analysis of the experimentally measured cylinder pressure data is necessary to gain further insight into the effects of engine control parameters and initial conditions on combustion characteristics, including heat release profiles and average in-cylinder temperatures. To analyze the experimental data presented in this document, a new heat release analysis routine was developed by Ortiz-Soto [78] in order to account for features of advanced combustion strategies, including high levels of internal residual dilution (in some cases, up to 50% of the total cylinder mass) and multi-mode combustion behavior. The analysis employs techniques for estimating residual gas fraction [79] and for determining parameters of interest for multi-mode combustion strategies including SACI, such as the timing of auto-ignition, the heat release fractions of deflagration and auto-ignition, and the unburned/burned gas properties throughout the cycle. The remainder of this section is a description of the heat release analysis routine developed by Ortiz-Soto [78] and implemented in analyzing the experimental data reported in this document.

2.2.1 First Law Approach

The heat release routine uses a basic First Law of Thermodynamics approach to determine the heat release profile [9]. The gross chemical heat release rate from combustion ($dQ_{hr,ch}/dt$) can be expressed as

$$\frac{dQ_{hr,ch}}{dt} = mc_v\frac{dT}{dt} + P\frac{dV}{dt} + \dot{Q}_{wall} \tag{2.1}$$

where m, c_v, and T are the estimated mass, specific heat at constant volume, and mean gas temperature, respectively, P is the measured cylinder pressure, and V is the cylinder volume, computed from the engine geometry. The first two terms on the right-hand side of Equation 2.1 equal the net apparent heat release rate ($dQ_{hr,net}/dt$), which accounts for changes in sensible internal energy and piston work. The burned mass fraction x_b is com-

puted by normalizing the cumulative gross chemical heat release $Q_{hr,ch}$ between the start and end of combustion. The start of combustion is assumed to represent the minimum value of $Q_{hr,ch}$, while the end of combustion represents the maximum value of $Q_{hr,ch}$. The rate of heat release ($RoHR$) can then be obtained via numerical differentiation of the cumulative gross heat release ($Q_{hr,ch}$) with respect to crank angle.

The mean gas temperature required for properties estimations and heat release calculations is computed from the ideal gas equation of state, Eq. 2.2,

$$T = \frac{PV}{mR} \tag{2.2}$$

where P and V are the instantaneous cylinder pressure and volume, respectively, and m is the total trapped mass, discussed in section 2.2.7. The gas constant R is a function of the average composition in-cylinder, discussed in section 2.2.6, which varies throughout the combustion process as reactants are converted into products. Based on the interdependence of T, R, and the combustion profile, the analysis must follow an iterative approach to allow for variable mixture properties.

2.2.2 Potential Sources of Error

Several factors can strongly affect the accuracy of the heat release results, both on an absolute basis as well as trend-wise. For engine experiments, these factors are a) cylinder pressure filtering, b) cylinder pressure pegging, c) analysis of mean vs. cyclic pressure traces, d) estimation of mixture properties, e) total mass estimation, f) in-cylinder combustion efficiency, and g) estimations of heat transfer. These factors pose additional sources of error to the inherent inaccuracies in the experimental measuring devices. As such, it is important to understand the relative sensitivities of the heat release results to systematic errors in the above listed parameters. Ortiz-Soto et al. [78] performed a detailed comparison of this heat release analysis to KIVA computational results and observed very good

agreement. For further details involving the heat release analysis and its implementation, please refer to [78].

Significant errors in measured data or in the above assumptions will directly influence $Q_{hr,ch}$ computed at the end of combustion (EOC). To test the accuracy of this value, an overall energy balance can be computed from the ratio of the gross chemical heat release at EOC to the expected fuel energy released.

$$EnergyBalance = \frac{Q_{hr,ch}(EOC)}{\eta_{comb} m_{fuel} Q_{LHV}} \tag{2.3}$$

In Equation 2.3, the denominator is the expected fuel energy release, defined as the product of the in-cylinder combustion efficiency η_{comb}, total mass of fuel m_{fuel}, and the lower heating value of the fuel Q_{LHV}. For the data points presented in this thesis, the energy balance ratios calculated in Eq. 2.3 fall within $\pm$ 2% of 1.0.

2.2.3 Filtering of Cylinder Pressure Data

The high-speed crank-angle resolved cylinder pressure measurements generally display some noise, and this can be problematic when trying to compute certain values based on numerical derivatives, such as the rate of heat release. Filtering the cylinder pressure data is a fairly standard practice; however, the filter should be selected properly to avoid excluding important features of the pressure trace. For heavily ringing cases, an improperly chosen low-pass filter can greatly reduce peak rates of heat release. For the data reported in this thesis, a 2nd order low-pass Butterworth digital filter with a cutoff frequency of 2.5 kHz is used. This frequency provides substantial smoothing of the pressure trace while minimizing changes to critical features including peak cylinder pressures and heat release rates.

2.2.4 Pegging of Cylinder Pressure Data

In-cylinder pressure is normally measured on a relative (gage) basis using piezoelectric pressure transducers, so accurate pegging of the pressure signal is critical. While the high-speed data acquisition system is configured to provide cyclic pegging of the real-time pressure trace, this process is repeated during the first steps of the heat release analysis to minimize cylinder pressure errors near IVC. The pegging procedure relies on the instantaneous absolute pressure in the intake manifold, which is measured by a Kistler 4007B piezoresistive sensor mounted in the intake port. Before spinning the engine, this sensor is calibrated to the ambient pressure. The pegging method assumes that at a given point, usually around BDC, the intake manifold and cylinder pressures are equal, as gas velocities are near zero. Of course, this assumption only applies if the intake valve is open at BDC. For all reported experiments, the closing of the intake valve occurs well after BDC, at $\sim$150° before firing TDC. In the heat release routine, the average intake pressure over a 1° CA window before and after intake BDC is used to compute a pressure offset value that is then applied to the entire cylinder pressure signal. This procedure is repeated for each of the 200 recorded cycles. Since the intake manifold pressure sensor likely has combined linearity and hysteresis errors of less than $\sim$0.3%, any substantial error in the pressure offset determined by this method is derived from the assumptions of the method rather than the measuring device itself.

2.2.5 Mean vs. Cyclic Analysis

The experiments reported in this thesis were performed under steady state conditions and 200 consecutive cycles of pressure data were recorded to obtain statistically significant results. In lieu of averaging the cyclic pressure traces and processing only the ensemble average pressure trace, heat release analysis of the full 200 pressure traces has been incorporated into the heat release code. This is the preferred method of analysis since the

ensemble average may not provide an entirely accurate representation of the combustion behavior for highly variable HCCI and SACI conditions. Throughout this thesis, reported curves of cylinder pressure, cylinder mass-averaged temperature, rate of heat release, and mass fraction burned have been averaged from the 200 processed cycles. In addition, parameters such as CA50, ringing intensity, and peak temperature were calculated on a cyclic basis and then averaged over all 200 cycles of data.

2.2.6 Mixture Properties Estimation

Determining the ratio of specific heats, γ, is particularly important since the First Law (Eq. 2.1) can also be expressed in terms of this property, as seen in Equation 2.4 [9].

$$\frac{dQ_{hr,ch}}{dt} = \frac{\gamma}{\gamma-1}P\frac{dV}{dt} + \frac{1}{\gamma-1}V\frac{dP}{dt} + \dot{Q}_{wall} \tag{2.4}$$

To estimate γ throughout the combustion process, it is assumed that the reactants are converted to products of complete combustion (CO_2, H_2O, N_2, and O_2). It has been shown by Ortiz-Soto [78] that this assumption gives almost identical results to a far more complex 15-species equilibrium model for lean and stoichiometric fuel-air mixtures. The routines for estimating γ incorporate thermodynamic databases [80, 81] and allow for multi-component fuels, including gasoline surrogates. If the actual molecular weight and the atomic H/C ratio of the fuel are available, a gasoline surrogate can be created to match these values. In the present model, the gasoline surrogate is composed of iso-octane (44.7% by volume), n-pentane (20.2%) and benzene (35.1%).

The mean gas composition is assumed to be a mixture of unburned and burned gases, weighted by the burned mass fraction x_b. The mass fraction of each individual species is determined by Equation 2.5.

$$Y^k = (1-x_b)\,Y_u^k + x_b Y_b^k \tag{2.5}$$

In this expression, Y^k is the mass fraction of the k^{th} species. The unburned species Y_u^k include a mixture of fresh reactants Y_{reac}^k determined from the measured 'fuel-to-air' equivalence ratio ϕ and combustion products Y_{EGR}^k determined from the estimated EGR mass fraction, as seen in Eq. 2.6. The composition of the EGR mixture (Y_{EGR}^k) is assumed to be composed of complete combustion products (Y_{prod}^k) and fresh reactants (Y_{reac}^k) weighted by the cycle combustion efficiency (η_{comb}), seen in Eq. 2.7. While this assumption does not take into account the individual species measured by the emissions bench (CO, NO_x, etc.), the error in the estimated properties is expected to be minor. The burned gas species Y_b^k in Eq. 2.5 are assumed to be complete combustion products at the measured equivalence ratio, seen in Eq. 2.8.

$$Y_u^k = (1 - EGR)\, Y_{reac}^k + EGR \cdot Y_{EGR}^k \tag{2.6}$$

$$Y_{EGR}^k = (1 - \eta_{comb})\, Y_{reac}^k + \eta_{comb} Y_{prod}^k \tag{2.7}$$

$$Y_b^k = Y_{prod}^k \tag{2.8}$$

2.2.7 Estimating the Trapped Mass

Adequate estimation of the trapped cylinder mass is crucial when calculating quantities such as mean gas temperature (which affects mixture properties) and overall energy balance. The total mass includes the incoming fuel, air, and external EGR (eEGR), as well as the internal EGR (iEGR) retained in-cylinder from the previous cycle.

$$m_{tot} = m_{fuel} + m_{air} + m_{eEGR} + m_{iEGR} \tag{2.9}$$

In Eq. 2.9, m_{fuel} is the injected fuel mass, m_{air} is the inducted air mass, m_{eEGR} is the EGR introduced externally, and m_{iEGR} is the internal EGR or residual mass.

In this engine setup, redundant methods are used to measure the fuel and air mass flow rates into the cylinder, including direct fuel metering and an oxygen sensor mounted in

the exhaust manifold. The air-fuel ratio is also computed from the emissions data using the standard Brettschneider formula [82] and atomic balance expressions for carbon and oxygen [76]. For lean fuel-air mixtures, good agreement ($<$ 2-3%) is typically seen for the different measurement techniques. Due to higher measurement accuracy, the fuel mass flow rate is used in conjunction with the measured air-fuel ratio from the exhaust gases to obtain the mass of air. The volumetric fraction of external EGR is determined from CO_2 measurements in the intake and exhaust manifolds, and the external EGR mass is then calculated from the total incoming mass.

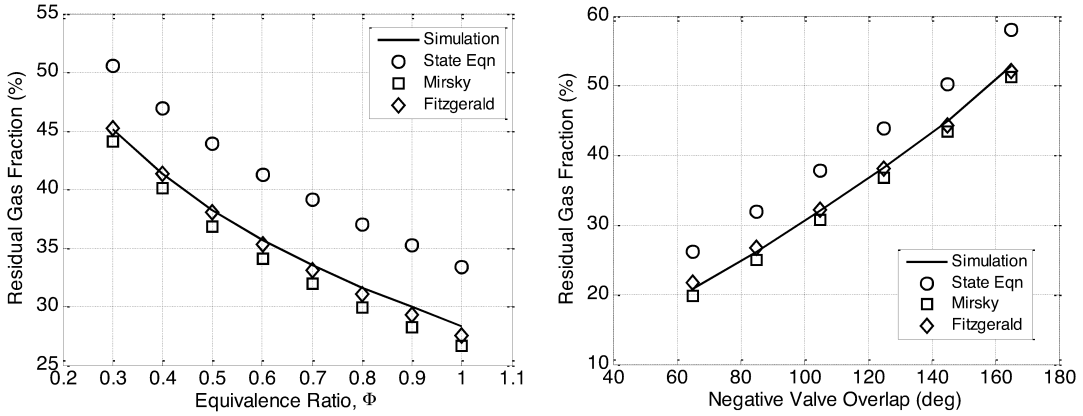

(a) Estimating RGF for varying ϕ [83] (b) Estimating RGF for varying NVO [83]

Figure 2.4: Results from Ortiz-Soto et al. [83] comparing three residual mass estimation techniques (State Equation method, Yun and Mirsky method, and Fitzgerald method) against a one-dimensional gas dynamics simulation performed using GT-Power software. The analysis was performed for varying levels of ϕ in Figure 2.4a and NVO in Figure 2.4b

A major uncertainty in the trapped mass calculation arises in the estimation of the residual mass, and this uncertainty can be particularly large for combustion strategies that employ a large degree of negative valve overlap (NVO). In SACI engines, the internal EGR can be as high as 50% of the total in-cylinder mass [36]. In this heat release routine, a method of residual gas fraction (RGF) estimation developed by Fitzgerald et al. [79] was chosen based on its improved accuracy when compared to two other residual estimation techniques: the State Equation method [83] and the Yun and Mirksy method [84]. In [83], the Fitzgerald method showed the best agreement with one-dimensional GT-Power gas dy-

namic calculations for naturally-aspirated engine operation, as seen in Figures 2.4a and 2.4b, which compare predictions of residual gas fraction for various equivalence ratios and levels of NVO, respectively. For the NVO sweep in Figure 2.4b, the State Equation method and the Yun and Mirsky method resulted in relative RGF errors of 10% and 3%, respectively, while the relative errors associated with the Fitzgerald method were about 1.5% [83].

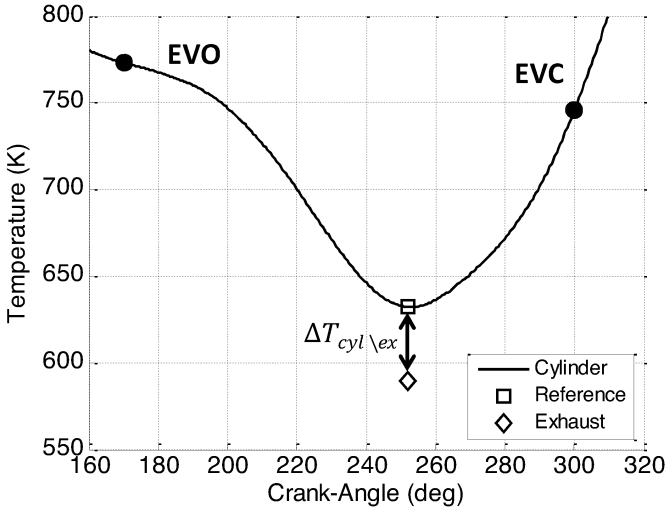

Figure 2.5: Determination of calibration factor ($\Delta T_{cyl\backslash ex}$) for Fitzgerald method [83]

The Fitzgerald method attempts to model the average in-cylinder temperature from EVO to EVC using the measured exhaust temperature and the instantaneous cylinder pressure while also accounting for heat loss during the exhaust process. A reference point for temperature calibration is selected at the minimum pressure between EVO and EVC, as seen in Figure 2.5. The temperature at the reference point T_{ref} is given by Eq. 2.10 (Eq. 11 in [79]) where T_{exh} is the exhaust temperature and $\Delta T_{cyl\backslash ex}$ is the temperature calibration factor, which is chosen as 45 K based on engine simulations at various conditions [83].

$$T_{ref} = T_{exh} + \Delta T_{cyl\backslash ex} \tag{2.10}$$

The in-cylinder masses at EVO and EVC (the residual mass) are determined using

the following series of equations which involve the principles of mass conservation and polytropic expansion and compression.

$$c_{p,BD}\left(T_{ref}-T_{EVO}\right)-R\frac{T_{ref}+T_{EVO}}{2}\ln\left(\frac{P_{ref}}{P_{EVO}}\right)= C_{BD/RC}\left[c_{p,RC}\left(T_{EVC}-T_{ref}\right)-R\frac{T_{EVC}+T_{ref}}{2}\ln\left(\frac{P_{EVC}}{P_{ref}}\right)\right] \tag{2.11}$$

$$m_{EVO}-m_{EVC}=\frac{P_{EVO}V_{EVO}}{RT_{EVO}}-\frac{P_{EVC}V_{EVC}}{RT_{EVC}}=m_{fuel}+m_{air}+m_{eEGR} \tag{2.12}$$

$$\frac{T_{EVO}}{T_{ref}}=\left(\frac{P_{EVO}}{P_{ref}}\right)^{n_{BD}} \tag{2.13}$$

$$\frac{T_{EVC}}{T_{ref}}=\left(\frac{P_{EVC}}{P_{ref}}\right)^{n_{RC}} \tag{2.14}$$

Equation 2.11 is determined from the 2nd Law of Thermodynamics to describe the exhaust blowdown (EVO to Reference) and recompression (Reference to EVC) processes. In this expression, (P_{EVO}, T_{EVO}), (P_{ref}, T_{ref}), and (P_{EVC}, T_{EVC}) represent the states at EVO, the reference point, and EVC, respectively. The gas constant R is assumed constant over the exhaust process and $c_{p,BD}$ and $c_{p,RC}$ are the average specific heat capacities during blowdown and recompression. The blowdown to recompression heat transfer ratio, $C_{BD/RC}$, is computed iteratively from the convective heat transfer equation (Eq. 2.16) and the heat transfer coefficient h is calculated using the Woschni correlation (Eq. 2.17 and Eq. 2.18), as discussed in section 2.2.9.

Equation 2.12 is formulated from the Ideal Gas Law to solve for the two unknowns in Eq. 2.11, T_{EVO} and T_{EVC}. The left-hand side of Eq. 2.12 is known from measurements of m_{fuel}, m_{air}, and m_{eEGR}. Once T_{EVO} and T_{EVC} are determined, the masses m_{EVO} and m_{EVC} (i.e. the residual mass, m_{iEGR}) can be computed.

The instantaneous cylinder temperature needed to calculate the convective heat transfer throughout the exhaust process to determine $C_{BD/RC}$ is obtained by assuming polytropic blowdown and recompression. The polytropic coefficients n_{BD} and n_{RC} are computed from Equations 2.13 and 2.14, respectively. Once the mass at EVC is computed, the internal

residual gas fraction (RGF) and total EGR fraction (internal + external) can be determined. The total EGR fraction is calculated in Equation 2.15.

$$EGR = \frac{m_{iEGR} + m_{eEGR}}{m_{total}} \tag{2.15}$$

The coupling between pressure, temperature, mixture properties, and mass requires that the Fitzgerald method be implemented iteratively. For heat release analysis on a cycle-by-cycle basis, the residual masses for individual cycles are computed using the measured gas exchange pressure data from the previous cycle.

Errors in residual mass estimation manifest themselves most prominently in the calculation of mass-averaged cylinder temperature. The Fitzgerald method relies heavily on the measured in-cylinder pressures during the exhaust process to estimate the residual fraction. Assuming a $\pm$ 5% error in cylinder pressure during the gas exchange process, the corresponding error in residual gas fraction is approximately $\pm$ 2-3% internal EGR, while the associated error in cylinder temperature is approximately $\pm$ 30 K near TDC. Over the range of conditions explored in this thesis, this error is expected to be systematic and should not drastically affect the observed trends. Overall, the reported residual fractions and corresponding peak temperatures are in agreement with values reported in the literature [65].

2.2.8 Combustion Efficiency

The in-cylinder combustion efficiency is computed from exhaust emissions measurements using the equations presented by Stivender [76], corrected to account for the retained unburned fuel in the residual. Based on the principle of mass conservation, the product of the measured exhaust combustion efficiency ($\eta_{comb,exh}$) and the injected fuel mass (i.e. the burned fuel mass) should equal the product of the in-cylinder combustion efficiency (η_{comb}) and the total in-cylinder fuel mass (including both the injected fuel mass and the estimated retained unburned fuel mass). Any amount of unburned fuel in the residual will

cause the in-cylinder combustion efficiency to be less than the measured exhaust combustion efficiency. This in-cylinder combustion efficiency is used in conjunction with the total in-cylinder fuel mass (m_{fuel}) when computing the denominator of Eq. 2.3 to yield a value for the total fuel energy released during the combustion event.

2.2.9 Heat Transfer Estimations

Calculating the gross heat release from cylinder pressure data requires an estimation of the heat loss to the cylinder wall. As this quantity is not typically measured in engine experiments, global heat transfer correlations are used. The heat transfer rate to the cylinder wall is the sum of the individual contributions from the cylinder head, liner, and piston, seen in Eq. 2.16.

$$\dot{Q}_{wall} = \sum hA_i (T - T_i) \tag{2.16}$$

In this expression, the subscript i denotes the various combustion chamber boundary regions. The cylinder head area (A_{head}) and the piston area (A_{pist}) are constant for a given engine geometry, and the cylinder liner area (A_{liner}) is computed from crank-slider relations. The temperature at the wall for these three regions is prescribed as a constant 450 K, and the mean cylinder temperature T is calculated throughout the cycle. The global convective heat transfer coefficient h (W/m^2/K) is a function of the instantaneous pressure, temperature, and cylinder volume. This value is calculated from the commonly used Woschni correlation [85] in Equations 2.17 and 2.18,

$$h = 3.26 B^{-0.2} P^{0.8} T^{-0.55} w^{0.8} \tag{2.17}$$

where B (m) is the engine bore, P (kPa) is the cylinder pressure, T (K) is the mean in-cylinder temperature, and w (m/s) is the characteristic gas velocity, calculated from the

following expression.

$$w = C_1 \bar{S}_P + C_2 V_d \left(\frac{T_r}{P_r V_r} \right) (P - P_{mot}) \tag{2.18}$$

The characteristic gas velocity w is proportional to the mean piston speed $\bar{S}_P$ (m/s), which effects in-cylinder flow motions, and a 'flame enhancement' term given as a function of the instantaneous firing pressure (P) and motoring pressure (P_{mot}), the displaced cylinder volume (V_d), and the temperature (T_r), pressure (P_r), and volume (V_r) at some reference condition, e.g. intake valve closing (IVC). This term accounts for heat transfer enhancements due to flame-induced convection [85]. As suggested by Woschni [85], $C_1 = 2.28$ and $C_2 = 3.24 \times 10^{-3}$ for the closed portion of the cycle.

Within the heat release routine, the Woschni correlation is slightly modified depending on combustion mode. Due to the absence of a flame in purely auto-igniting HCCI combustion, the 'flame enhancement' term in Eq. 2.18 is reduced by $1/6$ for HCCI combustion, as suggested by Chang et al. [86], in order to match experimentally measured heat fluxes in an HCCI engine. For SACI operation, this reduction factor is only applied after the predicted onset of auto-ignition. Ortiz-Soto has attempted to validate this modified Woschni correlation against KIVA simulation data with relative success [78]. Compared to KIVA models of HCCI and SACI combustion, the proposed modified Woschni correlation gives the lowest energy balance (Eq. 2.3) errors ($\sim$2%) compared to other published heat transfer correlations [85–88]. Still, heat transfer remains one of the largest sources of error in engine modeling, and uncertainties can be high when analyzing non-conventional combustion regimes, such as SACI, for which no new heat transfer correlations have been developed. As such, the existing correlations are the best available tools for analyzing and understanding the SACI combustion process.

2.3 Two-Zone Heat Release Analysis

For advanced combustion modes like SACI, which involve both auto-ignition and flame propagation, an additional two-zone heat release routine is employed. This two-zone model assumes that, following the spark event, the cylinder volume can be divided into an unburned (end-gas) zone and a burned product zone. The unburned gas temperature (T_u) refers to the temperature of the mixture ahead of the flame, which is composed of fresh charge and residual gas from the previous cycle. Prior to spark ignition, the unburned temperature is equal to the average in-cylinder temperature. For a given compression ratio, intake pressure, and mixture composition (masses of fuel, air, and EGR), an increase in the unburned temperature corresponds to an increase in the temperature at IVC and at every crank angle prior to spark ignition.

Following spark ignition, the end-gas is consumed at a rate dictated by the mass fraction burned curve. At each time step, changes in end-gas enthalpy associated with piston and flame compression, mass transfer to the burned zone, and heat loss to the wall are calculated. This enthalpy change is primarily used to predict the temperature in the unburned zone leading up to the start of end-gas auto-ignition.

$$\dot{m}^k_{u,FL} = -mY^k_u \dot{x}_{b,FL} \tag{2.19}$$

$$\frac{dH_u}{dt} = V_u \frac{dP}{dt} - \dot{Q}_{wall,u} + \sum \dot{m}^k_{u,FL} h^k_u \tag{2.20}$$

During the first part of the SACI combustion process, the unburned (end-gas) species Y^k_u are converted into constant pressure equilibrium products at the mass burning rate for flame propagation $\dot{x}_{b,FL}$, seen in Eq. 2.19. The end-gas energy conservation equation (Eq. 2.20) is formulated in terms of the total enthalpy H_u. In Eq. 2.20, V_u is the volume, $\dot{Q}_{wall,u}$ is the volume scaled heat transfer, and $\sum \dot{m}^k_{u,FL} h^k_u$ is the enthalpy out-flow due to mass consumption by the flame. At each new time step, the end-gas temperature is obtained from the gas properties routines using the updated end-gas species, calculated specific enthalpy,

and cylinder pressure [78].

Within the two-zone routine, combustion reactions are assumed to occur at constant pressure through the flame. As such, the burned gas temperature (T_b) is computed by converting the end-gas species into constant pressure and enthalpy equilibrium products. This T_b is also known as the adiabatic flame temperature. At any point during deflagrative heat release, the laminar flame speed (S_L) and T_b can also be estimated using correlations recently developed by Middleton et al. [89] and discussed in the following section. The correlations were developed using iso-octane as a gasoline surrogate as these two fuels have similar burning velocities and auto-ignition delay times.

In HCCI and SACI, the effects of engine operating conditions on the initial onset of the auto-ignition event need to be understood. In metal engine experiments, it is difficult to identify the exact point at which the end-gas initially begins reacting; in fact, optical images of SACI combustion by Zigler et al. [46] have shown concurrent heat release between flame propagation and auto-ignition, indicating that the two modes can exist simultaneously. However, by examining the heat release profile, it is possible to obtain a reasonable estimation of the time when the rates of heat release transition from slow 'flame based' rates to faster auto-ignition rates. This point is labeled as the location of auto-ignition (θ_{AI}) despite some minor heat release in the end-gas prior to the main ignition event and is used as a convenient representation of the transition from deflagration to auto-ignition.

Estimating the location of auto-ignition was previously accomplished by Persson et al. [47] by using the second derivative of the rate of heat release (*RoHR*) curve to identify the transition from Initial Slow Heat Release (*ISHR*), thought to be flame propagation, to auto-ignition, seen in Figure 2.6. Reuss et al. [48] performed low load SACI imaging experiments and found that this inflection point in the rate of heat release (separating the slow initial rates from the faster bulk rates) occurred at the same time that the end-gas chemiluminescence filled the field of view and began to exceed the intensity of the flame. This point was also estimated using the maximum second derivative of the *RoHR* curve.

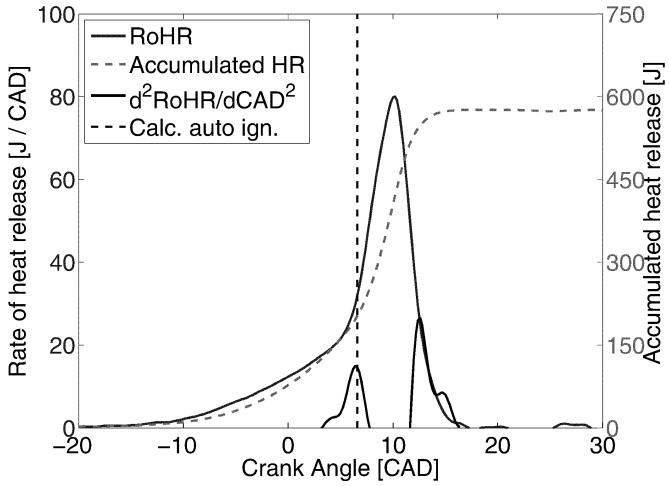

Figure 2.6: Estimating the onset of auto-ignition from the second derivative of the rate of heat release, as done by Persson et al. [47]

In the current heat release routine, the location of maximum curvature in the *RoHR* curve is used as an additional metric to define this mode transition. The curvature κ_{RoHR} is defined using the following expression.

$$\kappa_{RoHR} = \frac{RoHR''}{\left(1 + RoHR'^2\right)^{3/2}} \tag{2.21}$$

In Eq. 2.21, $RoHR'$ and $RoHR''$ are the first and second derivatives of the rate of heat release curve. The best results were obtained after normalizing the y-axis with respect to the peak rate of heat release and the x-axis with respect to crank angle within a $\pm$ 30° window around TDC. Figure 2.7 shows the *RoHR*, the second derivative of the *RoHR*, and the curvature of the *RoHR* calculated for a single SACI case [78]. Compared to the expected location for auto-ignition by visual inspection of the *RoHR*, the maximum $RoHR''$ and the maximum κ_{RoHR} occur too late and too early, respectively. However, the average of these two results, indicated with an asterisk in Figure 2.7, was found to be the most robust method for detecting the location of auto-ignition and is used in the heat release analysis routine of Ortiz-Soto [78].

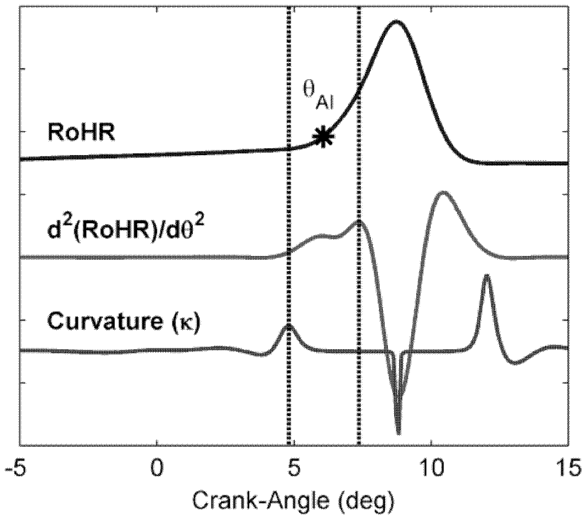

Figure 2.7: *RoHR*, *RoHR*$''$, and curvature of *RoHR* used in estimating the location of the main auto-ignition event [78]

While the transition between flame and auto-ignition occurs over a short period of time, the present heat release routine assumes an instantaneous transition between flame propagation and auto-ignition at the inflection point in the rate of heat release. Previous studies have shown that, in fact, this assumption is relatively robust. Computational work by Martz et al. [90, 91] showed that for laminar flames propagating into auto-igniting end-gases, the transition from the deflagrative to the auto-igniting combustion mode in the proximity of the flame is rapid, occurs near the end-gas ignition temperature ($\sim$1000 K), and is on the order of one flame time (i.e. the time it takes the flame to travel the distance equal to its own thickness) [90]. Locally, this implies that flame propagation is relatively insignificant at the onset of thermal runaway, and thus, a bimodal switch can usually be assumed without a significant loss in fidelity. For cases with slower auto-ignition chemistry, often characterized by a larger portion of flame based heat release, the period of transition between flame propagation and auto-ignition is expected to increase. Therefore, predictions for the onset of auto-ignition (and the corresponding fraction of deflagrative heat release) will likely have increased errors for these cases. KIVA simulations by Ortiz-Soto [78] suggest that this error in the onset of the main auto-ignition event should exceed no more than $1/4°$ CA.

2.4 Laminar Flame Speed Correlation

To gain a better understanding of the fundamental mechanisms governing the behavior of SACI flamelets, a correlation published by Middleton et al. [89] is used to estimate laminar flame speeds (S_L) near the time of spark for the engine experiments. A similar analysis has been conducted by other researchers, including Aleiferis et al. [92], who calculated density corrected flame propagation speeds from an optical SI engine shortly after (5° CA) the spark event. The experimental flame propagation rates were then compared to estimations of laminar burning velocity from correlations [93, 94] using the engine conditions at the time of spark, and remarkably similar results were obtained. This procedure was repeated for a variety of fuels, including iso-octane and gasoline, and the experimentally measured (and density corrected) burning velocities agreed rather well and showed the same trend-wise behavior as experimentally measured laminar burning velocities from a variety of sources [93–97].

This optical data suggested that flame propagation rates in the very early stages of combustion were highly affected by S_L. While this was too early for the flame to produce noticeable heat release, in general, the trends in measured flame radii shortly after spark ignition (for MFB $<$ 5-10%) were very similar to trends in the early burn rates (MFB $\geq$ 5-10%) obtained from the in-cylinder pressure measurements [92]. In Chapters 4 and 5, the S_L correlation of Middleton et al. [89] is used to infer information about the laminar flame speeds near the time of spark in order to better understand the trend-wise behavior in the early rates of SACI flame propagation (0-5% MFB). As the flame grows, the burning rate becomes increasingly affected by turbulent wrinkling of the flame surface area, in addition to S_L.

The S_L correlation [89] relies on the unburned gas temperature (T_u), pressure (P), and mixture composition at the point of interest. Cylinder pressure and unburned gas temperature are determined from the two-zone heat release analysis, while detailed compositional information is derived from direct engine measurements of the 'fuel-to-air' equivalence

ratio (ϕ) and the EGR mole fraction (X_{EGR}) or mass fraction. By considering the molar fractions of each stoichiometric product species (O_2, N_2, CO_2, and H_2O), the mixture can be divided into its 'reactive' and 'non-reactive' components. The fuel (of form C_xH_y) and O_2 (including the O_2 reinducted via EGR) are present only in the 'reactive' mixture, while CO_2 and H_2O are present only in the 'non-reactive' mixture. N_2 is present in both mixtures; $X_{N_2,Reac}$ refers to the mole fraction of N_2 associated with the molecular O_2 (in the N_2/O_2 ratio of air), and $X_{N_2,st}$ refers to the mole fraction of N_2 associated with the O_2 required to form the CO_2 and H_2O through stoichiometric combustion. Together, the CO_2, H_2O, and $X_{N_2,st}$ form the molar fraction of stoichiometric combustion products (X_{SCP}) defined in Eq. 2.24. When operating lean of stoichiometry, the EGR may contain a substantial amount of excess oxygen. As such, a more appropriate 'fuel-to-O_2' or 'non-product' equivalence ratio (φ) is derived in Eq. 2.22 [98]. The 'fuel-to-O_2' equivalence ratio φ and X_{SCP} are related by Eq. 2.23.

$$\varphi = \frac{(1 - X_{EGR})\,\phi}{1 - X_{EGR}\phi} \tag{2.22}$$

$$X_{CO_2} = \frac{X_{EGR}\phi x}{X_{EGR}\phi\left(\frac{y}{4} - 1\right) + \phi + 4.76\left(x + \frac{y}{4}\right)} \tag{2.23}$$

$$X_{SCP} = X_{CO_2} + X_{H_2O} + X_{N_2,st} = \left[1 + \frac{y}{2x} + \left(x + \frac{y}{4}\right)\frac{3.76}{x}\right] X_{CO_2} \tag{2.24}$$

The remaining species mole fractions are determined from the following expressions:

$$1 = X_{C_xH_y} + X_{O_2} + X_{N_2,Reac} + X_{CO_2} + X_{H_2O} + X_{N_2,st} \tag{2.25}$$

$$X_{C_xH_y} = \frac{\varphi(1 - X_{SCP})}{\varphi + 4.76\left(x + \frac{y}{4}\right)} \tag{2.26}$$

$$\frac{X_{N_2,Reac}}{X_{O_2}} = 3.76 \tag{2.27}$$

$$\frac{X_{N_2,st}}{X_{CO_2}} = \frac{3.76\left(x+\frac{y}{4}\right)}{x} \tag{2.28}$$

$$\frac{X_{H_2O}}{X_{CO_2}} = \frac{y/2}{x} \tag{2.29}$$

The kinetic and transport mechanisms used to develop the S_L correlation were validated against available laminar flame speed data at high temperature and high pressure conditions relevant to engine operation [95, 99, 100]. At these conditions, the burned gas temperatures (T_b) predicted by the correlation have been shown to agree with the constant pressure adiabatic flame temperatures to an average error and error standard deviation of 1.5% and 1.1%, respectively. For S_L between 20 and 200 cm/s (i.e. engine relevant conditions), the simulated burning velocities from the HCT code were reproduced by the correlation to an accuracy of about 2.4% with a standard deviation of 2.3% [89]. The resulting expression for laminar flame speed (S_L) includes terms corresponding to the 'fuel-to-O_2' equivalence ratio φ, a characteristic activation temperature for the flame chemistry (represented by the inner layer temperature T^0), and the temperature differences between T_u, T^0, and T_b. This correlation was developed for iso-octane, a common surrogate for gasoline. For the best fit parameters utilized in the following expressions, refer to Middleton et al. [89].

$$S_L = F\varphi^m \exp(-G/T^0)\left(\frac{T_u}{T^0}\right)\left(\frac{T_b-T^0}{T_b-T_u}\right)^n (1-X_{SCP})^{D_1} \tag{2.30}$$

$$T^0 = \left(\frac{-E}{\ln(P/B)}\right)\left[\varphi(1-X_{SCP})+C_7\right]^{C_8} + C_9T_u + a_1P^{a_2}\left[\left[\varphi(1-X_{SCP})\right]^{a_3}-1\right] \tag{2.31}$$

$$T_b = T_u + \varphi\left(c+d\varphi+e\varphi^2+fT_u+gP\right)(1-X_{SCP})^h \tag{2.32}$$

2.5 Variability in Measured Data

With any engine experiment, data variability is unavoidable. At best, this variation can be minimized and/or quantified. In recording experimental data, baseline engine conditions were often met before beginning a new sweep. This helped to ensure full engine break-in

and deposit conditioning. Peak motoring pressures were often recorded as well to ensure that the engine blowby had not changed significantly. For a given valve strategy, intake pressure, and intake temperature, one standard deviation in peak motoring pressure was recorded to be $\pm$ 0.8% over 10 days of engine testing.

In this thesis, each experiment was performed over one day of testing to eliminate variation associated with day-to-day changes in ambient conditions. However, it is still possible that baseline engine conditions could shift over the course of an entire day. As such, baseline conditions were often recorded at the beginning and end of each experiment to determine the variability over the course of an entire day of testing. In Table 2.4, several HCCI baseline conditions (at $\sim$4 bar $IMEP_n$) are compared over a single day of operation.

The 'Error (1σ)' column represents the percent error from one standard deviation around the mean for six sets of data (200 cycles each). These values represent the precision of the data since the engine input conditions were held as constant as possible throughout the test. A similar procedure was performed for SACI combustion at $\sim$6 bar $IMEP_n$ and the results are shown in Table 2.5. For the SACI combustion mode, a slightly higher amount of data scatter is expected (relative to HCCI) due to the inherent variability in flame kernel development.

For the range of conditions in Table 2.4 and Table 2.5, it is seen that the expected fluctuation in the averaged data (over 200 cycles) is rather small. While cycle-to-cycle variability is typically more substantial (especially for spark-ignited conditions), a conservative stability limit was used for the data presented in this thesis in order to minimize the variability on a case-by-case basis. While the reported absolute values are susceptible to errors within the assumptions of the analysis, the overall trends are expected to be repeatable if the range they traverse lies substantially outside the range of expected scatter for steady state operation. The SACI experiments presented in this thesis are well controlled and the resulting trends are repeatable on a day-by-day basis.

Combustion parameter	*Mean*	*Error (1σ)*
$IMEP_g$ (kPa)	421	$\pm$ 0.2%
Peak pressure (bar)	43.9	$\pm$ 1%
Fueling rate (mg/s)	206.5	$\pm$ 0.2%
CA50 (° aTDC)	8.4	$\pm$ 2%
CA10 (° aTDC)	3.3	$\pm$ 5%
CA90 (° aTDC)	14.6	$\pm$ 3%
Peak rate of heat release (J/CA)	60.7	$\pm$ 2.3%
Peak temperature (K)	1792	$\pm$ 0.5%
Exhaust temperature (°C)	694	$\pm$ 0.1%
Ringing intensity (MW/m^2)	1.76	$\pm$ 5%
NO_x Emissions (g/kg-fuel)	0.22	$\pm$ 2%
Temperature at IVC (K)	504	$\pm$ 0.2%
EGR mass fraction (-)	0.43	$\pm$ 0.4%

Table 2.4: Estimated scatter in measured parameters of interest over a day of testing for HCCI combustion at $\sim$4 bar $IMEP_n$. Six sets of data (with 200 recorded cycles each) are compared.

Combustion parameter	*Mean*	*Error (1σ)*
$IMEP_g$ (kPa)	650	$\pm$ 0.2%
Peak pressure (bar)	52.2	$\pm$ 1.5%
Fueling rate (mg/s)	316.4	$\pm$ 0.3%
CA50 (° aTDC)	8.7	$\pm$ 3%
CA05 (° aTDC)	-6.6	$\pm$ 2.2%
CA90 (° aTDC)	14.4	$\pm$ 4%
Location of auto-ignition (° aTDC)	5.3	$\pm$ 4%
Peak rate of heat release (J/CA)	68.5	$\pm$ 3.5%
Peak temperature (K)	2175	$\pm$ 0.6%
Exhaust temperature (°C)	514	$\pm$ 0.3%
Ringing intensity (MW/m^2)	2.75	$\pm$ 9%
NO_x Emissions (g/kg-fuel)	1.87	$\pm$ 5%
Temperature at IVC (K)	472	$\pm$ 0.2%
EGR mass fraction (-)	0.42	$\pm$ 0.3%
Fraction of flame heat release (-)	0.27	$\pm$ 0.5%
T_u at end-gas auto-ignition (K)	1037	$\pm$ 0.3%

Table 2.5: Estimated scatter in measured parameters of interest over a day of testing for SACI combustion at $\sim$6 bar $IMEP_n$. Seven sets of data (with 200 recorded cycles each) are compared.

2.6 Combustion Constraints

For the experiments presented in this thesis, engine operation is limited by excessive rates of pressure rise (ringing/knock) and unstable combustion, which leads to partial burn and/or misfire. Depending on combustion mode, the range of initial conditions that leads to acceptable engine operation can be rather small. Combustion stability is determined by the coefficient of variation (COV) of $IMEP_n$ over 200 consecutive engine cycles. For these experiments, a COV of $IMEP_n$ greater than 3-4% is regarded as unacceptable. For a faster burning combustion mode such as HCCI, a COV of $IMEP_n$ up to $\sim$5% can be tolerated.

Combustion is also limited by high rates of pressure rise which mechanically stress the engine components. These high rates of pressure rise lead to unacceptable levels of ringing intensity. The reported values of ringing intensity are calculated by averaging the values of ringing intensity for 200 consecutive cycles of engine pressure data using Equation 2.33 developed by Eng [23]. This equation shows that ringing intensity is proportional to the square of the maximum rate of pressure rise.

$$RI = \frac{1}{2\gamma} \frac{\left[0.05 \cdot \left(\frac{dP}{dt}\right)_{\max}\right]^2}{P_{\max}} \sqrt{\gamma R T_{\max}} \tag{2.33}$$

In this expression, $(dP/dt)_{\max}$ is the maximum pressure rise rate (kPa/ms), P_{max} is the peak cylinder pressure (Pa), $T_{\max}$ is the peak cylinder temperature (K), γ is the ratio of specific heats, and R is the gas constant (J/kg/K). Equation 2.33 returns the value of ringing intensity in W/m^2. For these experiments, ringing intensity is limited to 5.0 MW/m^2, corresponding to a maximum pressure rise rate of $\sim$5 MPa/ms for naturally-aspirated conditions.

Engine-out NO_x below 1.0 g/kg-fuel is roughly required for compliance with U.S. passenger car emissions regulations for systems without NO_x after-treatment [35, 49]. Excessive NO_x emissions are a concern for SACI operation since previous studies have shown that increasing engine load beyond the high-load limit of HCCI results in elevated burned

gas temperatures that lead to significant NO_x formation [50, 101]. As such, many studies within this document focus on stoichiometric SACI operation assuming that emissions can be treated effectively with a standard three-way catalyst. For air dilute mixtures that produce excessive NO_x, more costly forms of after-treatment will be required.

Chapter 3

Bridging the Gap between HCCI and SI with Spark-Assisted Compression Ignition

This chapter investigates the load extension capability of the SACI regime, which was accomplished through burn rate manipulation using the advanced features of the FFVA engine. As load increased, combustion phasing was held constant to maintain high thermal efficiency. This section summarizes these findings, setting the stage for further investigation.

3.1 Experimental Motivation

As mentioned in Chapter 1, attempts have been made to extend the upper load limit of HCCI using various strategies involving spark-assist, allowing the fueling content of a dilute mixture to be increased. In this section, a similar feat is attempted using a novel combustion control strategy to manipulate the phasing and burn rate of SACI combustion for various levels of ϕ'. The goal of this experiment is to increase engine load by traversing the dilution gap between HCCI ($\phi' \approx 0.4$) and SI ($\phi' \approx 0.7$) while maintaining high thermal efficiency, as seen in Figure 1.3b. As load is increased, a transition from primarily auto-igniting combustion to almost pure flame propagation is necessary for compliance with cylinder pressure rise rate limits.

3.2 HCCI Operating Regime

This experiment focused primarily on two combustion regimes: HCCI and SACI. Before attempting load extension via spark-assist, the engine was mapped in HCCI mode. The engine was operated at unheated naturally-aspirated conditions using both air and internal residual dilution to control load. The spark was not enabled and NVO sweeps were performed at several different fueling rates (7-11.5 mg/cycle) to vary combustion phasing. Table 3.1 lists the operating conditions for this initial HCCI experiment.

Parameter	*Value*
Engine speed (rpm)	2000
Fuel flow rate (mg/cycle)	7-11.5
Fuel pressure (bar)	$\sim$100
Intake pressure (bar)	1.0
Exhaust pressure (bar)	1.05
Intake temperature (°C)	40
Negative valve overlap (CAD)	150-205
Coolant temperature (°C)	90
Oil temperature (°C)	90
Valve lift (mm)	4.0
Fuel injection timing (° bTDC)	330
External EGR (%)	0

Table 3.1: Experimental conditions during HCCI operation

For each fueling rate the upper and lower NVO limits were set by ringing intensity (RI $>$ 5 MW/m^2) and stability (COV $>$ 5%) constraints, respectively. A larger degree of NVO phased combustion earlier by increasing the internal residual fraction, raising pre-combustion temperatures. Earlier combustion led to faster burn rates, higher rates of pressure rise, greater NO_x emissions, and a higher ringing intensity. Combustion was retarded through reduced amounts of NVO, resulting in a lower charge temperature, slower rate of pressure rise, and longer burn duration. These results are seen in the pressure, temperature, and rate of heat release curves in Figure 3.1, showcasing the effects of combustion phasing on the burn rates of HCCI. At a given fueling level, the reduced pressure rise rates from

combustion retard allowed fueling to be increased again, and the process was continued until the viable range of NVO steadily diminished and the limits of combustion were reached. Load was increased up to the maximum load limit, at which point no NVO settings were possible to achieve acceptable combustion.

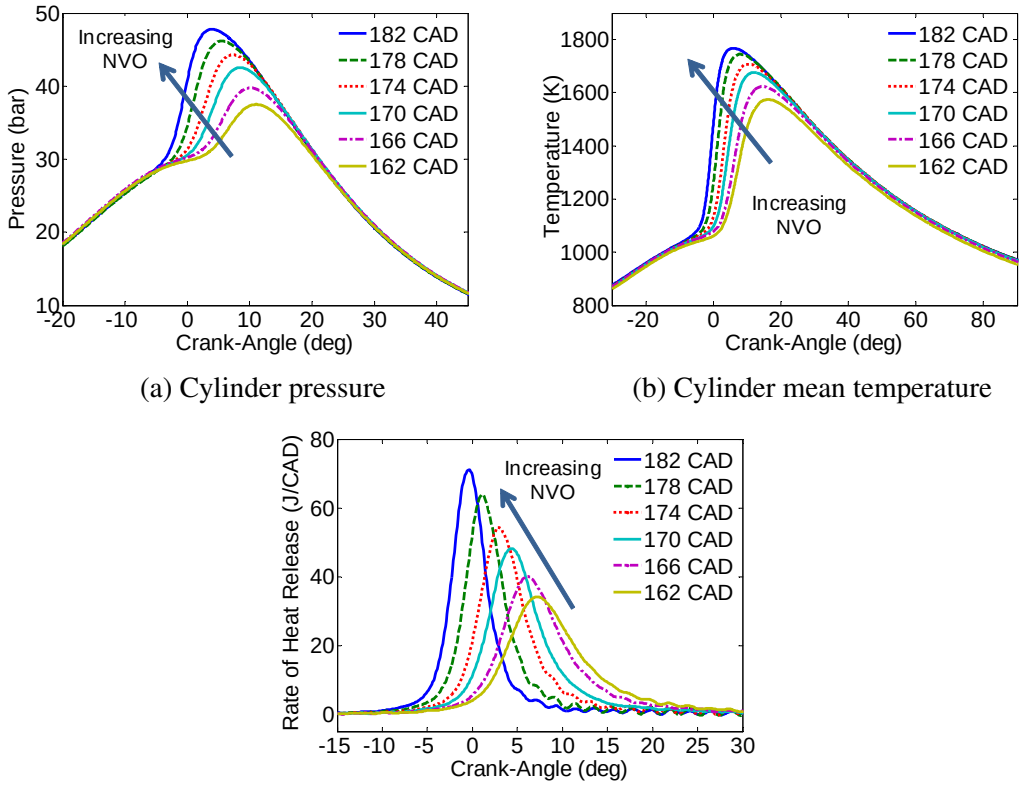

(a) Cylinder pressure

(b) Cylinder mean temperature

(c) Rate of heat release

Figure 3.1: (a) Cylinder pressure, (b) mass-averaged cylinder temperature, and (c) rate of heat release curves for HCCI combustion phased via NVO at a constant fueling rate of 10 mg/cycle

With the ringing and stability limits of combustion in mind, the usable range of HCCI was mapped in Figure 3.2. Figure 3.2a depicts load ($IMEP_n$) plotted against NVO while Figure 3.2b shows load plotted against CA50 (combustion phasing) for the usable HCCI regime. At low loads, a large range of NVO can be spanned before the limits of combustion are reached, as seen in Figure 3.2a. However, at high loads, slight changes in NVO have a large impact on combustion phasing. As fueling is increased, the limits of ring-

ing intensity and instability converge and the acceptable operating range narrows. At the maximum achievable load, only four degrees of NVO separate heavily ringing combustion from highly unstable combustion. Beyond this fueling rate, combustion phasing cannot be adjusted to mitigate ringing while still maintaining acceptable combustion stability. NO_x emissions for this entire operating regime did not exceed 1.0 g/kg-fuel.

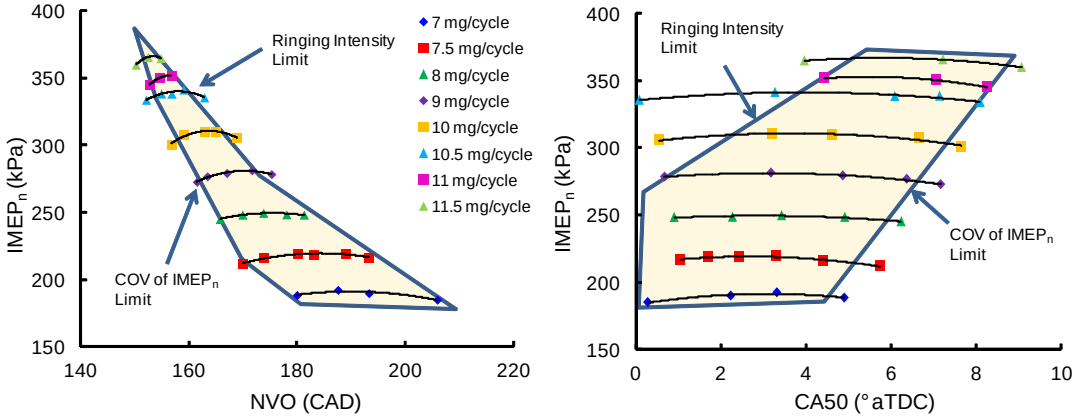

(a) IMEP$_n$ vs. NVO

(b) IMEP$_n$ vs. CA50

Figure 3.2: The HCCI operating regime, (a) IMEP$_n$ vs. NVO for several fueling rates (7-11.5 mg/cycle), and (b) IMEP$_n$ vs. combustion phasing (CA50)

With this engine, a maximum HCCI load of ∼3.7 bar IMEP$_n$ was achieved. Other researchers, notably Dec et al. [35] have managed to achieve naturally-aspirated HCCI up to ∼5.0 bar IMEP$_g$, possibly due to a different control strategy which relies on a high compression ratio and intake air heating rather than internal residual. In this experiment, a high degree of NVO could complicate the engine behavior by introducing cycle-to-cycle feedback, as discussed in Chapter 1. This feedback occurs when combustion is affected greatly by the thermal properties and combustion efficiency of the previous cycle and less by the incoming fresh charge conditions which are controlled more directly. For partially burned cycles at high loads, the NVO retains excess unburned fuel, causing advanced combustion and heavy ringing in the following cycle [29]. Thus, this setup is inherently less stable than that of Dec et al. [35].

3.3 SACI Operating Regime

Load extension into the SACI regime was achieved with stoichiometric fuel-air mixtures ($\phi = 1$) diluted with a combination of internal and external EGR, similar to previous studies [50–52, 102]. As load was increased beyond the limits of HCCI, peak combustion temperatures increased and unacceptable levels of NO_x emissions began to form, as seen in [52]. By creating stoichiometric mixtures at these higher loads through the addition of external EGR, practical after-treatment with a standard three-way catalyst (TWC) can be used. Accordingly, this SACI study focused only on stoichiometric operation so that NO_x emissions were not a concern.

To achieve higher load operation, peak heat release rates were modified using a combination of spark assist, internal EGR, and cooled external EGR. As fueling rate was increased beyond the limits of HCCI, cooled external EGR was added to decrease pressure rise rates and avoid heavy ringing; however, this also resulted in late and unstable combustion. Small amounts of internal EGR were then added (via increased NVO) to phase combustion earlier and achieve a stoichiometric mixture. External and internal EGR were finely adjusted until borderline stable, stoichiometric combustion was obtained. Finally, the spark was implemented to finely tune the combustion phasing and provide further stabilization. While Yun et al. [50] showed that SACI combustion phasing can be adjusted solely by tweaking the ratio of hot internal EGR to cooled external EGR, the spark provides easier and finer adjustment of combustion phasing, making it a valuable control parameter. These two methods of SACI combustion phasing control are compared in detail in the following sections.

This load extension strategy involving the simultaneous adjustment of internal EGR, external EGR, and spark advance differs somewhat from other previously implemented strategies. Szybist et al. [51] used only internal residual and late IVC to control the effective compression ratio and combustion timing at spark assisted high load operation; no external EGR was used. Knock mitigation was also assisted by the relatively low geometric

compression ratio of the engine (11.85:1) as well as the use of a high octane fuel. Cairns and Blaxill [6] achieved 5.5 bar brake mean effective pressure (BMEP) by modulating only internal and external EGR. Spark was implemented at a constant timing, but it was not the focus of the control strategy. The study presented here builds on these two former strategies to combine the effects of internal EGR, external EGR, and spark advance. Table 3.2 provides more details about the experimental conditions during the SACI portion of the study.

Parameter	*Value*
Engine speed (rpm)	2000
Fuel flow rate (mg/cycle)	12.5-24
Fuel pressure (bar)	$\sim$100
Intake pressure (bar)	1.0
Exhaust pressure (bar)	1.05
Intake temperature (°C)	40-50 (varies with eEGR)
Negative valve overlap (CAD)	175 to -5
Coolant temperature (°C)	90
Oil temperature (°C)	90
Valve lift (mm)	4.0-10.0
Spark advance (° bTDC)	22-43
Spark energy from the coil (mJ)	$\sim$70
Fuel injection timing (° bTDC)	330
External EGR, measured in the intake manifold (%)	12-25
EGR coolant temperature (°C)	60

Table 3.2: Experimental conditions during load extension (SACI mode)

3.3.1 SACI Phasing Control Method 1 - Spark Advance Sweep at Constant Load

The load extension strategy described in the previous section relied heavily on spark assist to control the start of ignition. At every SACI load level examined, it was apparent that spark advance affected combustion phasing, even for the most dilute mixture ($\phi' \approx 0.45$), as shown previously by Kopecek et al. [60]. Had lower load levels been explored, the

spark may not have had a noticeable effect on combustion phasing due to weak flame chemistry. To show the spark effect, a spark sweep was performed at a constant NVO of 118 crank angle degrees at ∼6 bar $IMEP_n$, well into the SACI regime. Spark timing was set to 39° before TDC and internal residual (via NVO) and external EGR levels were adjusted to establish borderline stable combustion while maintaining a stoichiometric 'fuel-to-air' equivalence ratio. Fuel flow rate was maintained at 19 mg/cycle, and the internal and external EGR fractions were held constant at 25% and 17%, respectively ($\phi' \approx 0.58$). Under these conditions, the spark timing was then advanced and its effect on combustion phasing was observed.

Figure 3.3 shows the cylinder pressure, mass-averaged cylinder temperature, rate of heat release, and mass fraction burned curves for spark timings that range from 39° to 45° before TDC. From Figure 3.3a, it is apparent that the cylinder pressure traces change noticeably as the spark is advanced. Earlier spark timings result in earlier combustion phasings (CA50 advances by ∼3°), higher rates of pressure rise, and higher peak pressures and temperatures, as seen in Figure 3.3b. Spark advance also results in higher peak rates of heat release, seen in Figure 3.3c and more rapid burn rates following auto-ignition, seen in Figure 3.3d. These results agree with Persson et al. [47], who showed that spark advance can be used to phase combustion even when the majority of the heat release contribution is from bulk auto-ignition. These SACI curves are also quite similar to the HCCI curves in Figure 3.1. In HCCI mode, combustion is phased by changing the initial state at IVC, whereas in SACI mode, the initial state is held constant and phasing is changed via spark advance. As seen in Figure 3.3b, the temperature curves prior to spark ignition are in excellent agreement, and the estimated temperatures at IVC are almost identical, fluctuating around 472 K by less than ± 1 K. Since these cases have the same composition and temperature profiles leading up to spark ignition, differences in combustion behavior are likely due to variations in spark advance and the in-cylinder conditions near the time of spark (e.g. turbulence and temperature).

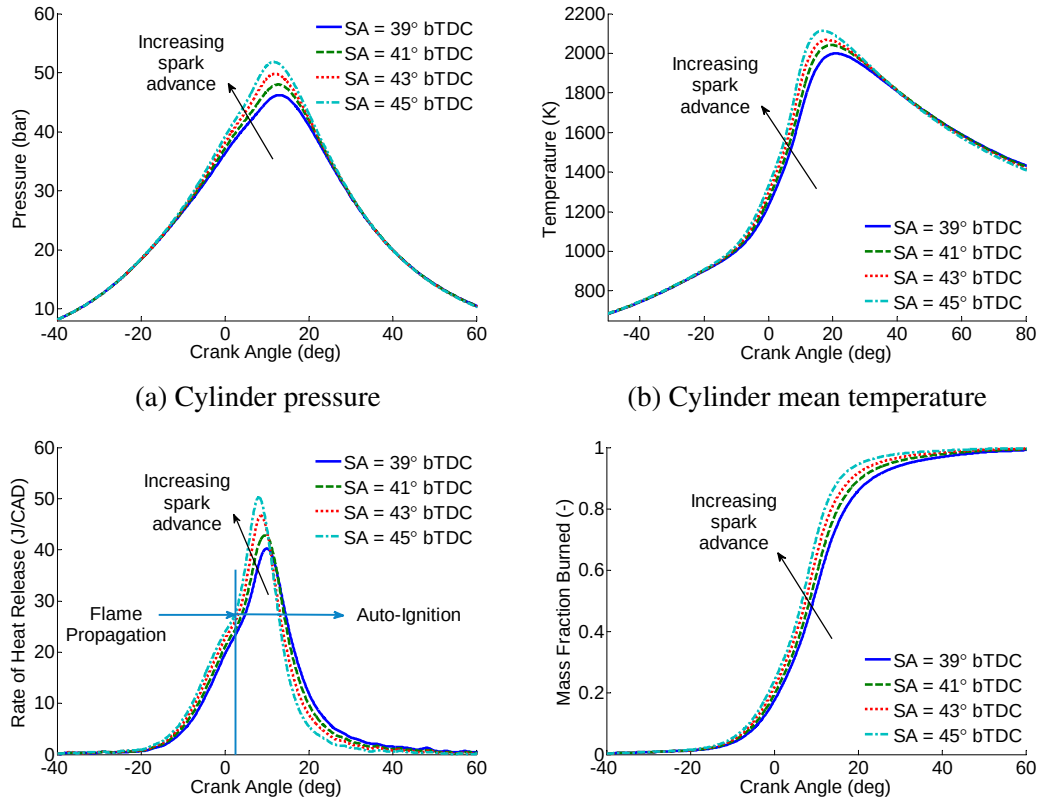

(a) Cylinder pressure

(b) Cylinder mean temperature

(c) Rate of heat release

(d) Mass fraction burned

Figure 3.3: (a) Cylinder pressure, (b) mass-averaged cylinder temperature, (c) rate of heat release, and (d) mass fraction burned curves for the SACI spark advance sweep at constant fueling rate, T_{IVC}

The heat release curves of Figure 3.3c show two distinct regions: an initial region of slow heat release, consistent with flame propagation, is followed by more rapid heat release characteristic of bulk auto-ignition. This multi-mode combustion is representative of SACI, and optical experiments have noted similar behavior within this region [103, 104]. The transition from one mode to the other is defined by a rapid change in the slope of the heat release rate, as seen by Persson et al. [47]. While dilute SACI flame propagation is perhaps slower than stoichiometric SI flame propagation (depending on the level of preheat), overall burn durations are low due to the increased burn rates associated with bulk heat release. These results show that flame propagation and auto-ignition can exist together in dilute, preheated operating conditions.

Figure 3.4a depicts the effect of spark advance on the subsequent locations of 5% mass fraction burned, 10% burned, auto-ignition (defined by the inflection point in the rate of heat release curve), 50% burned, and 90% burned. As spark is advanced, combustion is initiated earlier in the cycle and all subsequent mass burned fractions occur earlier. The location of auto-ignition also advances by ∼2 crank angle degrees. As auto-ignition occurs earlier in the cycle (where the rates of piston expansion are low), burn rates and peak rates of heat release increase, and the 5-90% burn durations decrease by ∼5 CAD (17%). Similar behavior was seen for the HCCI experiments in Figure 3.1, where CA50 was advanced by increasing NVO [29].

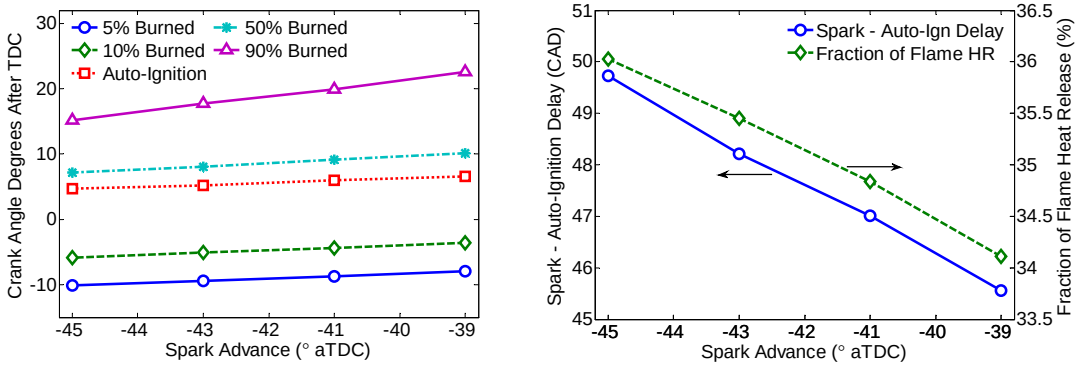

(a) Burn durations

(b) Auto-ignition delay time

Figure 3.4: (a) Locations of 5% burned, 10% burned, auto-ignition, 50% burned, and 90% burned for the points of the SACI spark timing sweep at constant fueling rate and T_{IVC} and (b) crank angle delay between spark timing and the onset of auto-ignition and the fraction of flame based heat release for each case

Although 5-90% burn durations decrease with more advanced spark timings, the 0-5% burn durations, which represent the early flame growth period [73], increase by ∼5 CAD. As seen in Figure 3.4b, the fraction of slower initial heat release (i.e. flame propagation) increases from 34% to 36% as the spark is advanced, and the time between the spark event and the onset of auto-ignition increases by ∼4 CAD. These observations indicate that the initial burn rates are lower for more advanced spark timings, possibly due to differences in in-cylinder conditions at the time of spark ignition. Optical engine experiments by Persson

et al. [47] and Zigler et al. [46] showed similar results, where the earliest detected flame expansion speeds decreased as the spark was advanced, and this behavior was attributed to a decrease in mixture temperature at the time of spark. Persson et al. [47] also suggested that differences in flow field and turbulence conditions at earlier spark timings could play a role in lowering the initial flame propagation rates. For the SACI cases in Figure 3.3, the temperatures at spark ignition decrease by $\sim$38 K between the most retarded and most advanced spark timings.

Although the initial flame expansion rates decrease for more advanced spark timings, following the spark event, these rates quickly increase as turbulence becomes the primary rate control factor [66]. By initiating the flame earlier in the cycle (via spark advance), a slightly larger mass fraction can be consumed via flame propagation before the unburned mixture reaches the conditions required for auto-ignition. This behavior is seen by the increase in the fraction of flame based heat release in Figure 3.4b. Additionally, the earlier onset of flame propagation causes the unburned mixture to reach the temperatures required for auto-ignition earlier in the cycle, even through cylinder temperatures at IVC are constant between each case. Despite the decrease in the early burn rates for the most advanced spark timing case, the combustion is actually the most stable in terms of COV of $IMEP_n$, as seen in Figure 3.5b. This stability is likely due to the fact that auto-ignition occurs earlier in the cycle, leaving the burned gas less prone to quenching by rapid piston expansion.

Figures 3.5a and 3.5b depict the effects of spark advance on NO_x emissions and ringing intensity, respectively. As spark timing and CA50 advance, the earlier onset of auto-ignition produces higher peak cylinder pressures and temperatures that result in increased NO_x emissions. Peak cylinder temperatures are consistently above 2000 K, as seen in Figure 3.5a, and thus, the NO_x limit of 1.0 g/kg-fuel is slightly exceeded, necessitating the use of a three-way catalyst for after-treatment.

As seen in Figure 3.5b, ringing intensity increases with a more advanced spark and CA50 due to an earlier onset of auto-ignition which increases pressure rise rates. How-

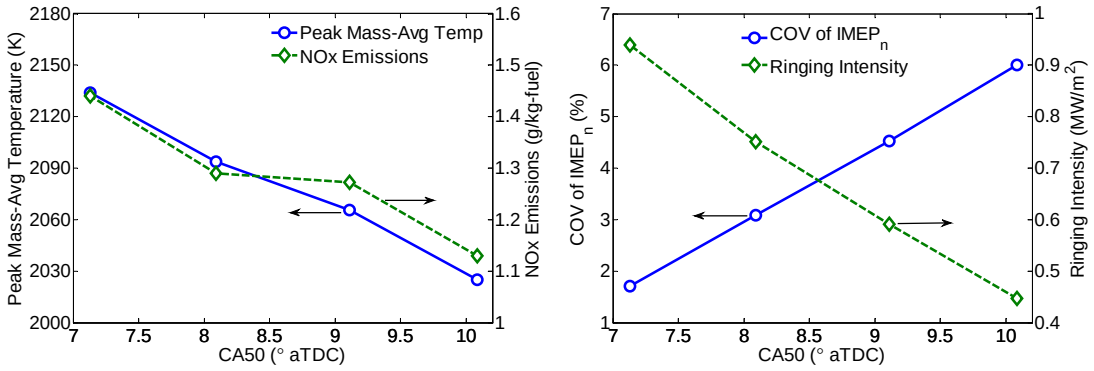

(a) Peak temperature and NO_x (b) Ringing and COV of $IMEP_n$

Figure 3.5: (a) Peak mass-averaged cylinder temperature and NO_x emissions and (b) ringing intensity and COV of $IMEP_n$ vs. CA50 for the SACI spark timing sweep at constant fueling, T_{IVC}

ever, for the range of spark timings examined, the ringing intensity remains well below the acceptable limit of $\sim$5.0 MW/m^2. By releasing a large portion of the fuel energy via deflagration, peak rates of pressure rise are substantially lowered compared to a pure auto-ignition event at a similar load (i.e. dilution level). Had the IVC temperature for these cases been elevated with increased NVO (and decreased external EGR), auto-ignition would have occurred even earlier and ringing intensity would have increased for a comparable range of spark timings.

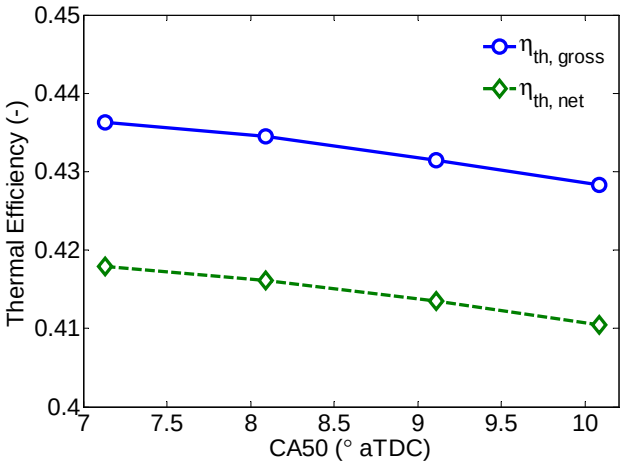

Figure 3.6: Gross and net indicated thermal efficiencies vs. CA50 for the SACI spark timing sweep at constant fueling, T_{IVC}

Figure 3.6 shows the effect of spark advance on the gross and net indicated thermal efficiencies. As spark is advanced and CA50 occurs earlier, the combustion process becomes slightly more efficient due to proper combustion phasing. As combustion retards, expansion pressures and work outputs decrease by less than 1% absolute. Had the phasing been advanced earlier than 7° after TDC, thermal efficiency would have likely decreased again due to increased heat transfer rates resulting from elevated peak cylinder temperatures.

3.3.2 SACI Phasing Control Method 2 - Unburned Gas Temperature Sweep at Constant Load

For the previous sweep, the ratio of internal to external EGR (hence, the temperature at IVC) remained fixed as spark was advanced from 39 to 45° before TDC. The study presented in this section demonstrates that SACI combustion phasing can also be altered by varying the temperature of the charge at IVC (i.e. the unburned gas temperature, T_u) at a constant spark advance. This sweep was done for the same fueling rate as the previous sweep (19 mg/cycle) and the spark advance was set to 38° before TDC. The temperature prior to spark ignition was adjusted by replacing a portion of hot internal EGR (via decreased NVO) with an equivalent portion of cooled external EGR to maintain a stoichiometric 'fuel-to-air' equivalence ratio ($\phi = 1.0$). Between each case, a mere two crank angle degree change in NVO resulted in a significant shift in combustion phasing. Between the most advanced case (heavily ringing) and the most retarded case (highly unstable), NVO decreased from 128° CA to 122° CA, as seen in Figure 3.7a, causing the temperature at IVC to decrease by $\sim$18 K and CA50 to retard by $\sim$8°. Figure 3.7b depicts the in-cylinder internal and external EGR mass fractions for each case, as well as the total dilution rate, which remained constant at $\sim$40%.

From the curves of cylinder pressure and temperature, seen in Figures 3.8a and 3.8b, it is apparent that combustion phasing is incredibly sensitive to changes in unburned gas temperature. The estimated in-cylinder temperatures at spark ignition (38° before TDC)

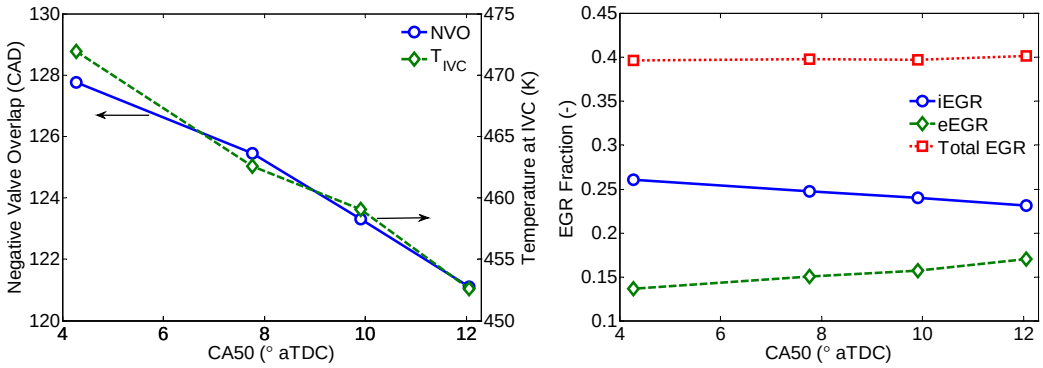

(a) NVO and T_{IVC} vs. CA50 (b) EGR mass fractions

Figure 3.7: Strategy for phasing SACI combustion at a constant spark advance (38° before TDC) - (a) decrease NVO to decrease T_{IVC} and retard CA50 and (b) replace the internal residual with cooled external EGR to maintain $\phi = 1$ and total EGR dilution rate at ∼40%

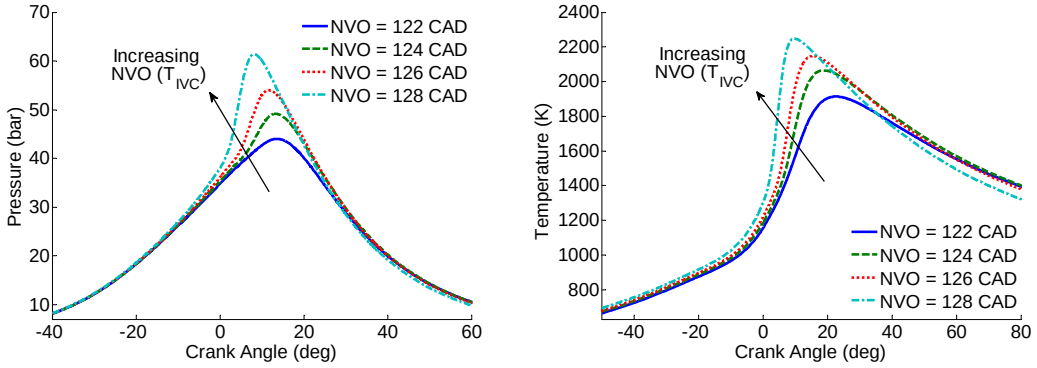

(a) Cylinder pressure (b) Cylinder mean temperature

Figure 3.8: (a) Cylinder pressure and (b) mass-averaged cylinder temperature for the SACI T_u sweep at constant fueling rate, spark advance

increase by ∼30 K between the most retarded case and the most advanced case, as seen in Figure 3.9. However, combustion phasing more than spans the acceptable operating range in terms of ringing and instability, seen in Figure 3.10. The increase in ringing is caused by a dramatic increase in peak rates of pressure rise as combustion advances and auto-ignition occurs earlier in the cycle. As this happens, combustion becomes less susceptible to high rates of piston expansion, which can lead to instability and misfire.

COV of $IMEP_n$ also increases for the case with the highest ringing intensity. This behavior may be partially related to cyclic variations in heat transfer which are caused by pressure waves that result from intense ringing [105]. As combustion phasing retards and

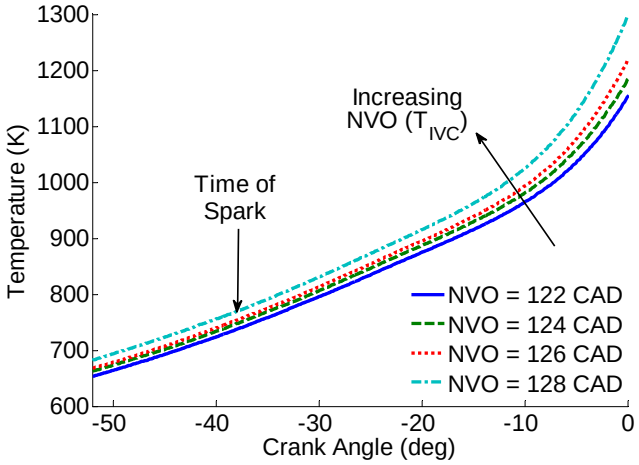

Figure 3.9: Closer view of the mass-averaged cylinder temperature at the time of spark for the SACI T_u sweep at constant fueling rate, spark advance

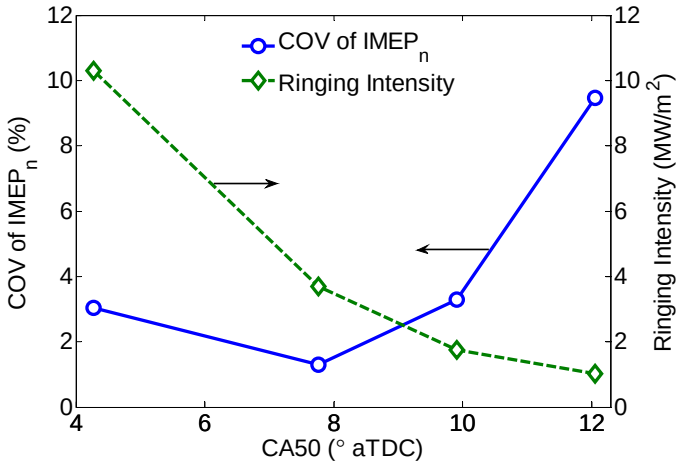

Figure 3.10: Ringing intensity and COV of $IMEP_n$ vs. CA50 for the SACI T_u sweep at constant fueling rate, spark advance

auto-ignition occurs later in the cycle, COV of $IMEP_n$ becomes unacceptably high. Peak mass-averaged cylinder temperatures also increase as combustion advances, leading to increased NO_x emissions, seen in Figure 3.11. For the most advanced case, peak temperatures exceed 2200 K, resulting in more than three times the acceptable level of NO_x. However, these emissions can still be treated with a three-way catalyst due to the stoichiometric nature of the mixture.

The locations of 5% mass burned fraction, 10% burned, auto-ignition, 50% burned, and 90% burned are plotted against combustion phasing (CA50) in Figure 3.12a. Spark timing

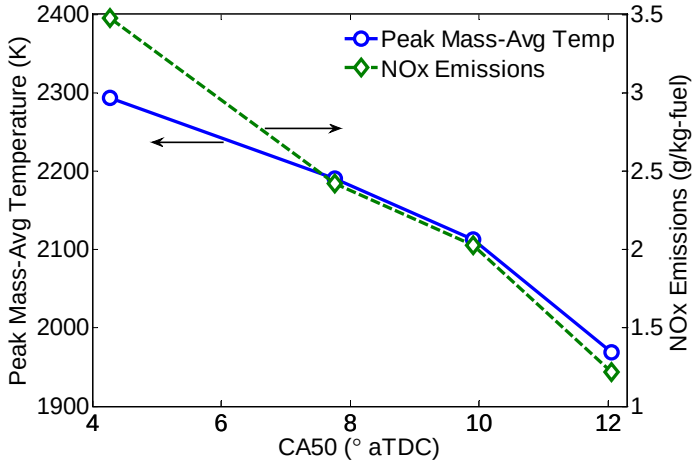

Figure 3.11: Peak mass-averaged cylinder temperature and NO_x emissions vs. CA50 for the SACI T_u sweep at constant fueling rate, spark advance

is held constant for every case as previously discussed. As the temperature at the time of spark increases, the location of every subsequent mass burned fraction occurs earlier and the 5-90% burn duration decreases by more than 14 CAD ($\sim$48%). The 0-5% burn duration also decreases for the most advanced CA50 cases, possibly due to the increased cylinder temperatures at the time of spark. As the temperature at the time of spark increases, initial flame propagation rates likely increase due to higher unburned (and hence, burned) gas temperatures. Turbulence levels are likely comparable for each case due to constant spark advance, engine speed, and valve events [92]. Additionally, a higher T_u combined with more rapid compression heating from the flame results in a shorter delay time between spark ignition and the onset of auto-ignition, as seen in Figure 3.12b. Since elevated unburned gas temperatures cause both flame propagation and auto-ignition to occur faster, a substantial change in combustion phasing results from a relatively small increase in T_u, and hence, a dramatic change in burn duration is seen. Although initial flame expansion rates are likely faster for the higher T_u cases, the fraction of flame based heat release is lower due to the more rapid onset of auto-ignition, seen in Figure 3.12b.

The advance in combustion phasing with increased T_u is clearly seen in the rate of heat release curves in Figure 3.13a, where an earlier onset of bulk auto-ignition inside a smaller

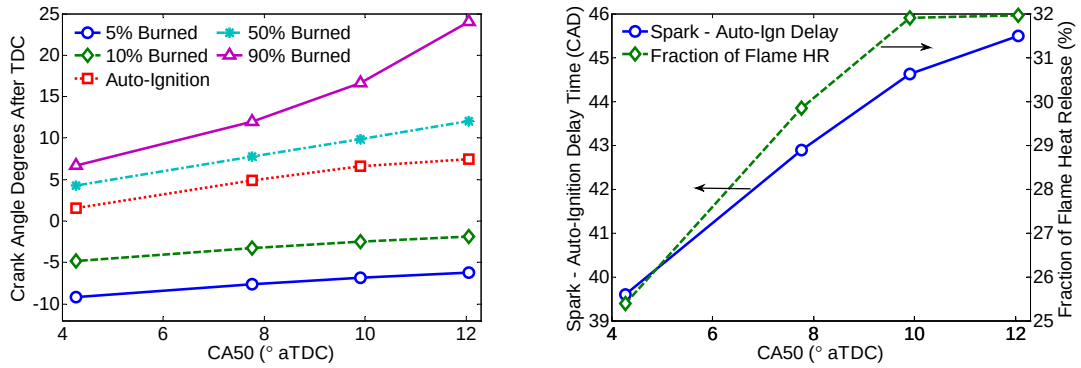

(a) Burn durations (b) Auto-ignition delay time

Figure 3.12: (a) Locations of 5% burned, 10% burned, auto-ignition, 50% burned, and 90% burned for the points of the SACI T_u sweep at constant spark advance (38° bTDC) and (b) crank angle delay between spark timing and the onset of auto-ignition and the fraction of flame based heat release for each case

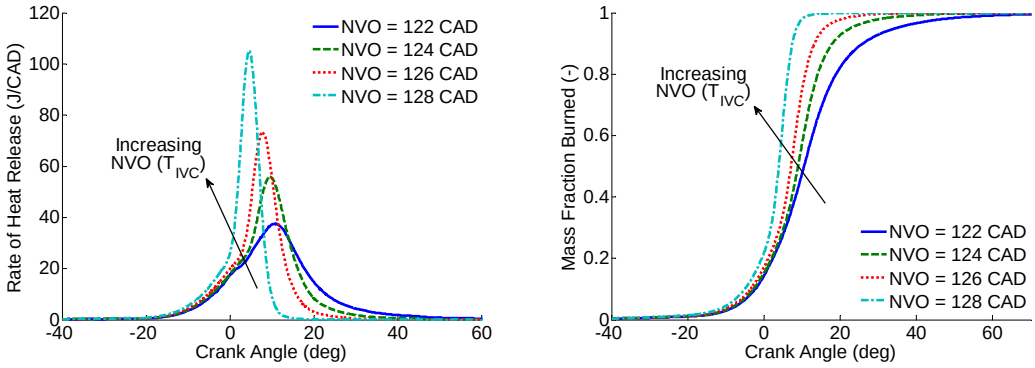

(a) Rate of heat release (b) Mass fraction burned

Figure 3.13: (a) Rate of heat release and (b) mass fraction burned curves for the SACI T_u sweep at constant fueling rate, spark advance

cylinder volume results in a substantial increase in the peak rate of heat release. The mass fraction burned curves in Figure 3.13b also show a rapid increase in burn rate as unburned gas temperature increases.

Figure 3.14 depicts the gross and net indicated thermal efficiencies for this SACI T_u sweep, which decrease as CA50 is either advanced or retarded away from the high efficiency region, which appears to occur 8-10° after TDC. A computational study by Lavoie et al. [65] showed that for adiabatic combustion (i.e. zero heat transfer), the best thermal efficiency occurs with CA50 at top dead center (0° after TDC), regardless of burn dura-

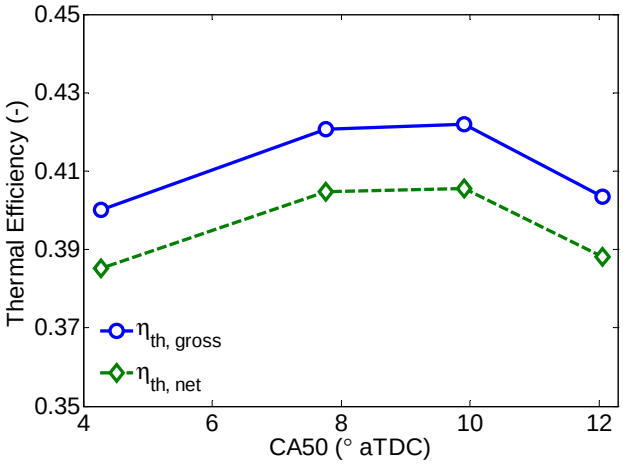

Figure 3.14: Gross and net indicated thermal efficiencies vs. CA50 for the SACI T_u sweep at constant fueling rate, spark advance

tion. As combustion retards, an efficiency penalty is incurred. However, with normal heat transfer, the optimal CA50 retards, resulting from a tradeoff between heat losses for early high-temperature combustion and expansion losses for late-phased combustion. Lavoie et al. [65] suggested that optimal CA50 occurs earlier for shorter burn duration cases resembling HCCI ($\sim$5-7° after TDC) while longer SI-like burn durations find optimal phasing at $\sim$10° after TDC. Although optimal CA50 occurs earlier for shorter burn durations, thermal efficiency is affected only minimally within this high efficiency range. Throughout this thesis, combustion phasing is typically set to 7-10° after TDC (depending on combustion mode) for experiments performed at a constant CA50.

This SACI T_u sweep in which internal EGR (via NVO) is traded for external EGR suggests that unburned gas temperature has a profound effect on SACI combustion phasing, as only a 6° CA increase in NVO ($\sim$18 K increase in IVC temperature) advanced combustion phasing from the brink of misfire to dangerously ringing conditions. In examining Figure 3.3, it becomes apparent that combustion phasing is less sensitive to small incremental adjustments in spark timing than to adjustments in NVO. A 6° CA (15% relative) advance in spark timing advanced CA50 by $\sim$3°, while a 6° CA (5% relative) increase in NVO advanced CA50 by $\sim$8°. Therefore, spark advance plays an important role in controlling

combustion phasing as load is extended into the SACI regime and T_u is manipulated to control the onset of auto-ignition and cylinder pressure rise rates.

3.3.3 SACI Load Sweep at Constant CA50

To bridge the dilution gap shown in Figure 1.3b, a sweep in which load was increased into the SACI regime while maintaining constant combustion phasing was conducted. At each load condition, internal EGR, external EGR, and spark timing were adjusted to achieve a CA50 of $\sim$8° after TDC while attempting to comply with engine stability and ringing/knock constraints. This CA50 was chosen to provide near maximum thermal efficiency, which was previously shown to decrease as CA50 moves away from this high efficiency region [9, 65]. Within the SACI regime, a maximum load of $\sim$7.5 bar IMEP_n was achieved.

Figure 3.15 depicts the valve control strategy used as both fuel and air flow rates were increased with load to maintain a stoichiometric 'fuel-to-air' equivalence ratio ($\phi = 1.0$). As fueling rate increased, the required air flow and T_u were achieved by decreasing NVO and raising the valve lift from 4 mm to 10 mm, transitioning the valve events from high NVO, low lift (typical for HCCI) to conventional high lift, full duration events. At the highest load conditions, a small amount of positive valve overlap was achieved. This decrease in NVO lowered the maximum cylinder pressure during the recompression portion of the cycle, as seen in Figure 3.15, where the arrows indicate the direction of decreasing NVO.

Figure 3.16a depicts the variation in the mass fractions of internal and external EGR with engine load. As load increased, the fraction of internal EGR (via NVO) was decreased in order to decrease compression temperatures (i.e. T_{IVC}), thereby delaying the onset of auto-ignition and mitigating ringing/knock. A portion of this internal EGR was then replaced with external EGR to maintain a stoichiometric fuel-air mixture ($\phi = 1$). This external EGR also provided further reductions in compression temperature due to an increased c_p compared to air. Despite this increase in external EGR with load, the total

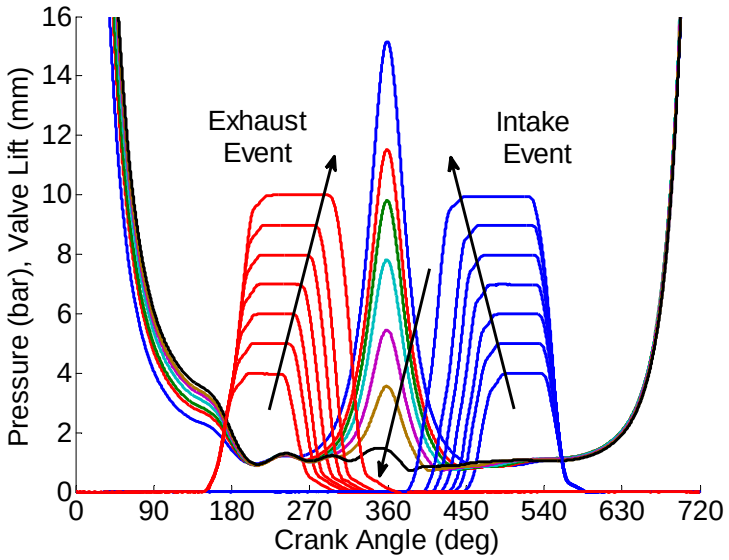

Figure 3.15: Valve control strategy for the SACI load sweep at constant CA50 ($\sim$8° after TDC); arrows indicate direction of increasing load/decreasing NVO

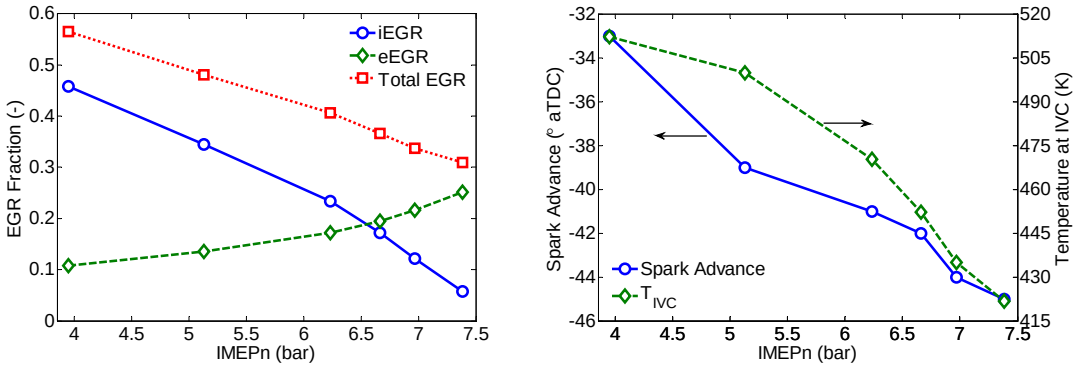

(a) EGR mass fractions

(b) SA and T_{IVC} vs. $IMEP_n$

Figure 3.16: Strategy for load extension into the SACI regime at constant CA50 - (a) decrease compression temperature (i.e. T_{IVC}) by trading internal EGR for a smaller amount of external EGR, thereby decreasing total EGR rate while maintaining $\phi = 1$ and (b) advance spark timing to compensate for the lower T_{IVC} by allowing more time for flame propagation to occur

dilution rate (i.e. the combined internal and external EGR fractions when $\phi = 1$) decreased as load increased and hence, ϕ' increased from $\sim$0.45 to $\sim$0.7 which, according to Figure 1.3b, spans the effective range of the SACI regime.

As load increased and the temperature at IVC decreased (via NVO reduction and external EGR addition), spark timing was advanced to maintain CA50 at 8° after TDC, as seen in Figure 3.16b. The lower compression temperatures required to reduce pressure rise rates resulted in a longer auto-ignition delay time, and thus, the combustion process relied more on flame propagation and required more time for completion. Had the spark not been advanced as load increased, combustion phasing would have occurred later in the cycle and combustion instability would have increased.

It should be mentioned that the internal and external EGR rates used for each load level were somewhat arbitrary, as they were chosen in order to obtain stable combustion while avoiding excessive ringing/knock. Throughout the literature, the knocking limitations for various combustion modes are defined rather inconsistently, making it difficult to evaluate the severity of knocking combustion within the SACI regime where the combustion mode varies from almost pure auto-ignition to pure deflagration. Had these knocking restrictions been better defined, a 'correct' ratio of internal to external EGR could have been implemented to achieve a similar knocking index for each load condition. As this was not the case, the severity of ringing/knock for some load conditions could be higher or lower than the severity for other load conditions. A metric that consistently defines knock during a mode transition such as this currently does not exist, and the ringing intensity metric of Eng [23] cannot be used to properly evaluate the severity of SI knock. These shortcomings are discussed further toward the end of Chapter 3.

Figure 3.17 depicts the combustion curves of the load sweep. In Figure 3.17a, as load is increased from 3.9 bar to 7.4 bar IMEP_n, combustion appears to transition from more 'HCCI-like' to more 'SI-like'. For the lowest load case, minimal flame propagation heat release is observed since T_{IVC} is sufficiently high and auto-ignition occurs shortly after

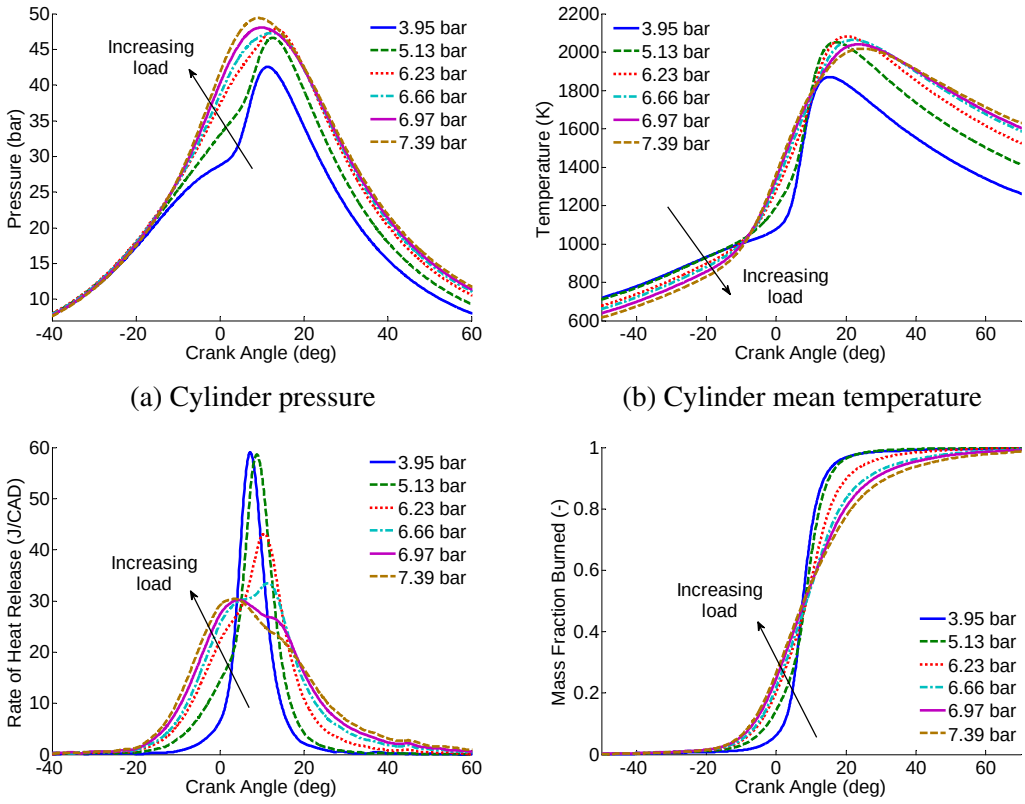

(a) Cylinder pressure

(b) Cylinder mean temperature

(c) Rate of heat release

(d) Mass fraction burned

Figure 3.17: (a) Cylinder pressure, (b) mass-averaged cylinder temperature, (c) rate of heat release, and (d) mass fraction burned curves for the SACI load sweep at constant CA50

spark ignition. From the temperature curves in Figure 3.17b, it is apparent that the compression temperatures prior to spark ignition decrease substantially as load increases due to a decreased fraction of hot internal EGR. As mentioned previously, these lower compression temperatures increase the auto-ignition delay time and prevent violent end-gas knock at higher load operation. As temperature decreases, less fuel mass is consumed via auto-ignition, peak rates of pressure rise and temperature rise decrease, and peak mass-averaged cylinder temperatures are kept relatively low, consistent with dilute operation.

From the rate of heat release curves in Figure 3.17c, it is seen that as load increases, a larger portion of the heat release occurs via flame propagation. As temperatures prior to ignition decrease, as seen in Figure 3.17b, auto-ignition is less likely to occur and more compression heating by the flame is necessary to initiate auto-ignition. Since flame prop-

agation is inherently slower than bulk auto-ignition, the overall burn duration increases, as seen in Figure 3.17d, and the spark event must occur earlier in the cycle to maintain a constant CA50. Figure 3.17c also shows that peak rates of heat release decrease as auto-ignition contributes less to the combustion process. As more of the fuel is consumed by deflagration, the fuel mass available for auto-ignition is reduced, and this auto-igniting fuel likely resides closer to the cylinder wall where it could be increasingly affected by wall cooling effects. Both of these aspects could contribute to reduced peak rates of heat release for higher load operation.

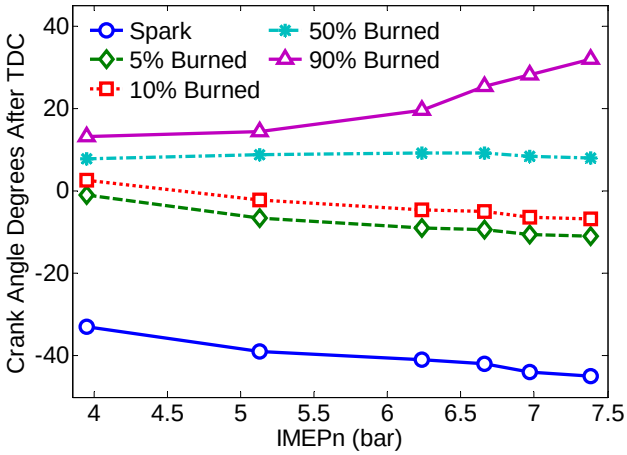

Figure 3.18: Locations of spark advance, 5% mass fraction burned, 10% burned, 50% burned, and 90% burned for the SACI load sweep at constant CA50

Figure 3.18 shows the locations of spark ignition, 5% mass fraction burned, 10% burned, 50% burned, and 90% burned. The location of auto-ignition is not included as it occurs intermittently from cycle-to-cycle for the highest load cases and therefore, its location is difficult to quantify. As load is increased, CA05 and CA10 occur earlier due to the advance in spark timing. Interestingly, the early burn durations (0-5% MFB) remain somewhat constant, indicating that flames can be sustained at lower ϕ' as long as the temperature of the unburned mixture (T_u) is elevated by means of charge preheating. CA50 is constant throughout the load sweep, in accordance with the control strategy. CA90 increases with load due to an increase in burn duration as rapid auto-ignition is replaced with

deflagrative heat release. Although the combustion process begins earlier, it ends later due to the inherently slower nature of flame propagation. This increase in overall burn duration potentially contributes to the increase in COV of $IMEP_n$ as load increases, as seen in Figure 3.19. This increase in instability could have been avoided had compression temperatures been increased slightly at each load level. However, an increase in temperature was avoided to maintain a low perceived level of knock intensity, as discussed in the following sections.

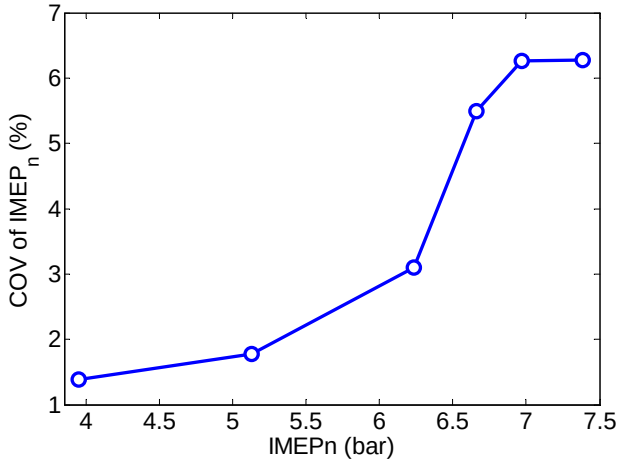

Figure 3.19: Variation in COV of $IMEP_n$ as load increases for the SACI load sweep at constant CA50

As a visual representation of the SACI operating conditions shown in Figure 3.17, the unburned (T_u) and burned (T_b) gas temperatures at TDC where calculated for every case (assuming polytropic compression) and plotted on the multi-mode combustion diagram developed by Lavoie et al. [49] and introduced in Chapter 1. To generate the diagram, a pressure of 27 bar was chosen as a fairly accurate representation of the motoring TDC pressure for each case and the flame and auto-ignition limits were estimated by assuming EGR dilute operation at $\phi = 1$.

It is seen in Figure 3.20 that the experimental SACI points agree fairly well with the predicted region. As load increases, ϕ' increases, and T_u must decrease in order to suppress ringing/knock. For a lower T_u, the mixture becomes less prone to auto-ignition (ignition delay increases) and the fraction of flame based heat release increases, causing the combustion

mode to transition from the HCCI region (pure auto-ignition) closer to the SI region (pure flame propagation). During this transition, ϕ' increases from $\sim$0.45 to $\sim$0.7, approaching the dilution limit of pure SI combustion [57].

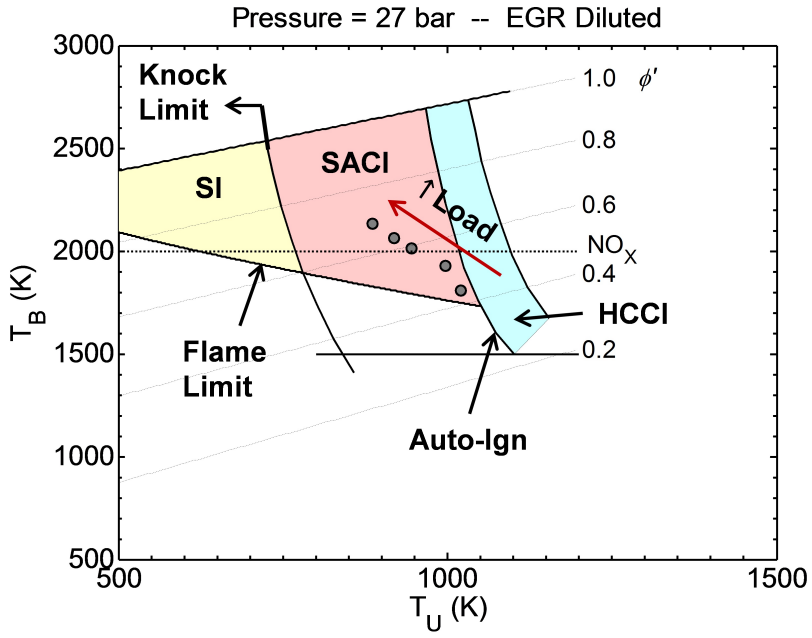

Figure 3.20: Experimental SACI points plotted on the multi-mode combustion diagram of Lavoie et al. [49] in terms of T_u and T_b at TDC and ϕ' for stoichiometric ($\phi = 1$) EGR dilute combustion

Despite the decrease in unburned temperature at TDC, estimated burned gas temperatures (T_b) increase with load due to lower levels of charge dilution at higher ϕ'. The burned gas temperatures (i.e. constant pressure adiabatic flame temperatures) were estimated using the correlation by Middleton et al. [89] introduced in Chapter 2, which relies on the pressure, unburned temperature, and composition of the mixture at the point of interest, i.e. TDC. At higher load conditions (lower ϕ'), it is seen that flames can tolerate lower unburned gas temperatures due to an increase in the burned gas temperatures. On the other hand, as dilution rate increases (ϕ' decreases), burned gas temperatures decrease and more pre-heating is required to avoid flame quench. However, a higher T_u also increases the propensity of the mixture to auto-ignite, resulting in a lower ratio of deflagrative to bulk heat release.

This increase in T_b as load (and hence, ϕ') increases is consistent with the increase in NO_x emissions seen in Figure 3.21. NO_x increases even though peak mass-averaged cylinder temperatures remain relatively low, seen in Figure 3.17b. The NO_x limit line in Figure 3.20 corresponds to a burned gas temperature of 2000 K, above which NO_x has been shown to form in significant quantities [106]. According to the MMCD, unacceptable levels of NO_x form for ϕ' above $\sim$0.5, and this observation is consistent with the measured levels of NO_x in Figure 3.21 for ϕ' above 0.5. Although these levels exceed the limit of 1.0 g/kg-fuel, they can still be treated effectively due to the stoichiometric nature of the mixture.

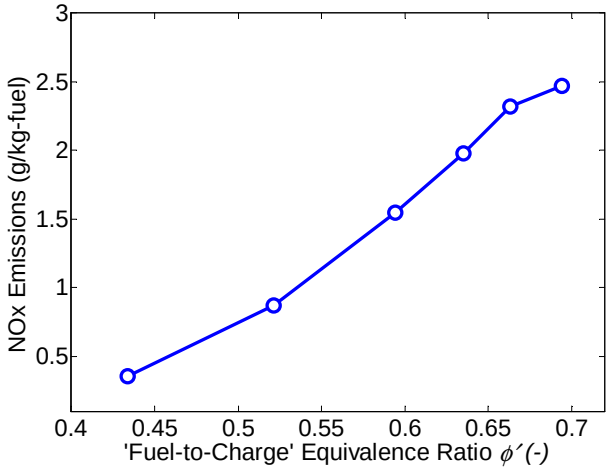

Figure 3.21: Variation in NO_x emissions as ϕ' increases for the SACI load sweep at constant CA50

Figure 3.22 depicts the ringing intensity and maximum pressure rise rate (PRR) as load increases. Ringing intensity as defined by Eng [23] in Equation 2.33 is primarily a function of the maximum PRR. At low load SACI, where the pressure and rate of heat release curves resemble HCCI, auto-ignition occurs shortly after spark ignition and peak rates of pressure rise and peak heat release rates are relatively high, as seen in Figures 3.17a and 3.17c, respectively. As load increases further and more of the fuel mass is consumed via flame propagation, peak rates of heat release and pressure rise rates decrease dramatically and

so does ringing intensity. At the highest load conditions, where dilution levels are low and spark timing is advanced, maximum pressure rise rates start to increase again; however, this increase is due to the earlier onset of flame propagation heat release coupled with piston compression, not auto-ignition.

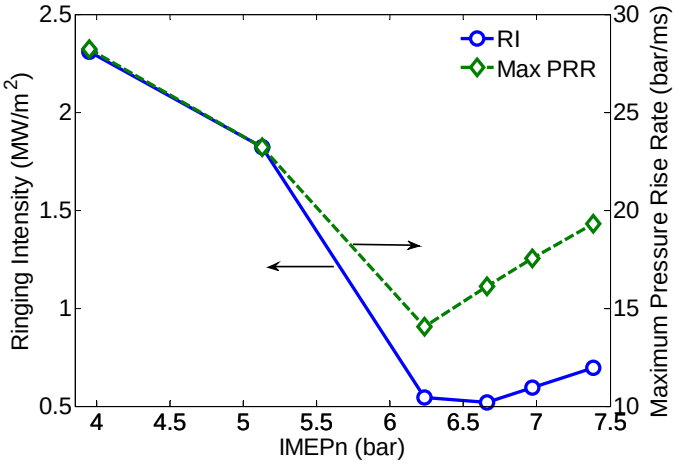

Figure 3.22: Variation in the ringing intensity of Eng [23] and maximum rates of pressure rise for the SACI load sweep at constant CA50

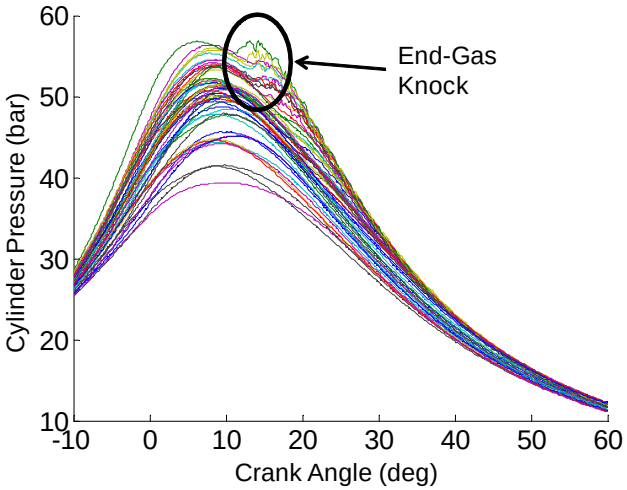

Figure 3.23: End-gas knocking behavior for high load 'SI-like' SACI at 7.39 bar IMEP$_n$, CA50 $\sim$8° after TDC

At the highest load conditions, where flame propagation consumes a majority of the charge mass, the auto-ignition event resembles conventional spark-ignited knock, as seen

in Figure 3.23. At this condition, internal residual and, hence, unburned gas temperature is minimized by the use of conventional full-duration valve events, yet audible knock is still present, likely due to the engine's high compression ratio. This knock occurs intermittently from cycle-to-cycle (only the earliest phased cycles exhibit knock), and it is not captured in the average pressure trace, as seen in Figure 3.24, where the shaded area represents the envelope of unfiltered pressure traces from 200 consecutive cycles. The smooth curve that lies within the envelope represents the filtered average cycle and the curves that lie at the upper and lower boundaries of the envelope represent the unfiltered pressure traces with the highest and lowest peak pressures, respectively.

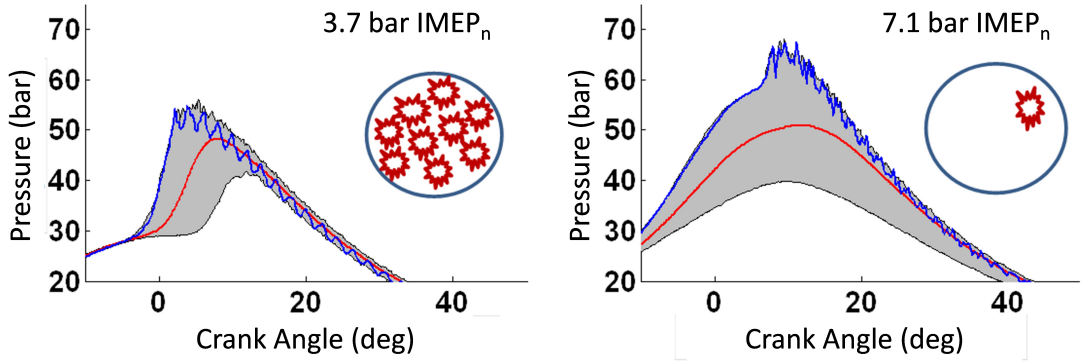

Figure 3.24: HCCI 'volumetric' knock at 3.7 bar IMEP$_n$ (left) and SI 'end-gas' knock at 7.1 bar IMEP$_n$ (right) [107]

In the HCCI case on the left-hand side of Figure 3.24, 'volumetric' knock is caused by the simultaneous onset of auto-ignition at multiple location within the cylinder, resulting in consistently high pressure rise rates seen in the average filtered pressure trace [107]. On the right, SI 'end-gas' knock is caused by an auto-ignition pocket near the wall, where the charge energy density, pressure, and burned gas temperatures are higher than those in dilute HCCI operation. However, this knock does not occur every cycle and thus, the average pressure rise rates are relatively low. At this 'SI-like' condition, the ringing intensity correlation of Eng [23] is inappropriate, and additional metrics should be evaluated to better determine the knock intensity of these higher load SACI conditions. In the fol-

lowing chapters, SACI combustion with the majority of the heat release from auto-ignition is investigated. For simplicity, the ringing intensity of Eng in 2.33 is used to quantify the knocking intensity at these conditions.

3.3.4 Mapping the SACI Regime

The SACI load extension strategy relied heavily on spark advance to control the onset of ignition and combustion phasing. At each fueling rate examined, spark timing was advanced and retarded to phase the combustion within the engine operating constraints, similar to the procedure used in Section 3.3.1. The results of this exploration are seen in Figure 3.25, plotted above the HCCI results in Figure 3.2b. For each SACI fueling rate, CA50 was controlled via spark advance, whereas for each HCCI fueling rate, CA50 was controlled via NVO. It is seen that load can be well extended above the usable range of HCCI using SACI flame based heat release to modulate the overall burn rate. As CA50 advances, the ringing intensity (for lower ϕ') and the frequency of 'SI-like' knocking combustion (for higher ϕ') increases. As phasing is retarded, combustion stability decreases.

The maximum ϕ' reached in this experiment is $\sim$0.7 which, according to the literature [57, 108], is the approximate dilution limit for SI combustion. At this point, both SI knock and unstable combustion are encountered, as seen in Figure 3.25. Had the unburned gas temperature been increased via NVO to reduce the COV of $IMEP_n$, the knocking intensity would have increased. Thus, this strategy was avoided. Additional attempts to mitigate the end-gas knock through spark retard and external EGR addition were unsuccessful and led to a greater deterioration in combustion stability. A late IVC strategy was also attempted in order to decrease the effective compression ratio, but this led to a decline in $IMEP_n$ due a potential loss in inducted mass through the open intake valve.

A similar SACI 'high-load' limit was also encountered by Weall et al. [102] on an engine with a similar compression ratio (11.85:1) and valve system. It is possible that higher loads could have been reached had the severity of the knock been properly quantified.

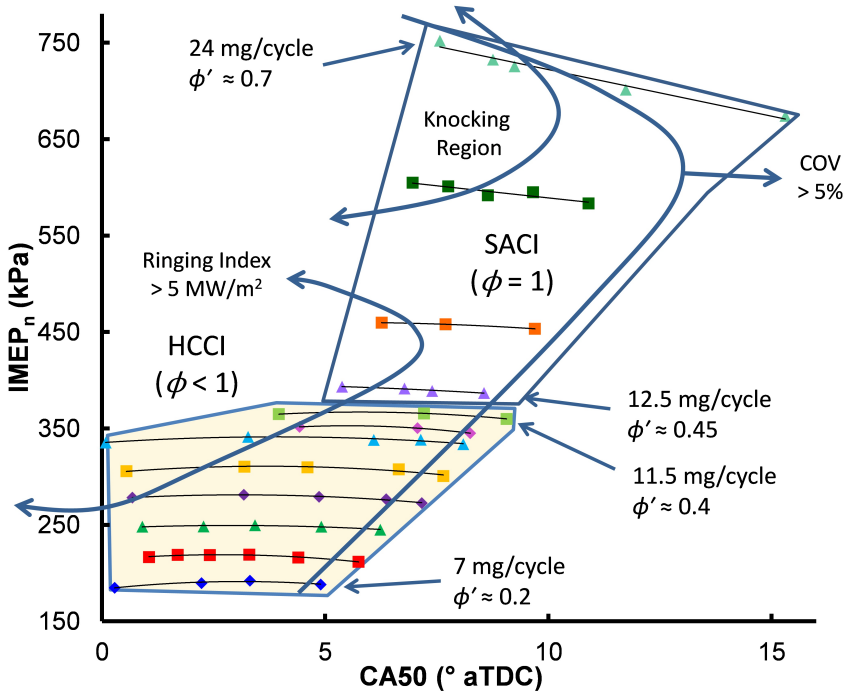

Figure 3.25: The acceptable regions of HCCI and SACI combustion, in which combustion was phased with NVO and spark advance, respectively

Depending on combustion constraints, additional pathways across the SACI regime are possible, although it is unexpected that the usable path would deviate far from that shown in Figure 3.20, as T_u and T_b would be restricted by engine stability and knock/ringing. This usable operating range is further explored in Chapters 4 and 5.

Although the high compression ratio of this engine prevents non-knocking SI at higher load conditions, a transition from low load HCCI to high load (knocking) SI has been demonstrated. SACI can, therefore, be used to bridge the gap between pure auto-ignition ($\phi' \approx 0.45$) and (almost) pure flame propagation ($\phi' \approx 0.7$) by relying on increased unburned temperatures to sustain flames in highly dilute mixtures, as seen in Figure 3.20.

Various contour plots of the SACI regime are seen in Figures 3.26, 3.27, and 3.28. Figure 3.26a shows the decrease in NVO as load increases, reducing the internal residual fraction, seen in Figure 3.26b, and hence, the tendency of the mixture to auto-ignite. In addition, this decrease in NVO allowed more air to be inducted into the cylinder to maintain a stoichiometric mixture at higher fueling rates. At the highest loads, positive valve

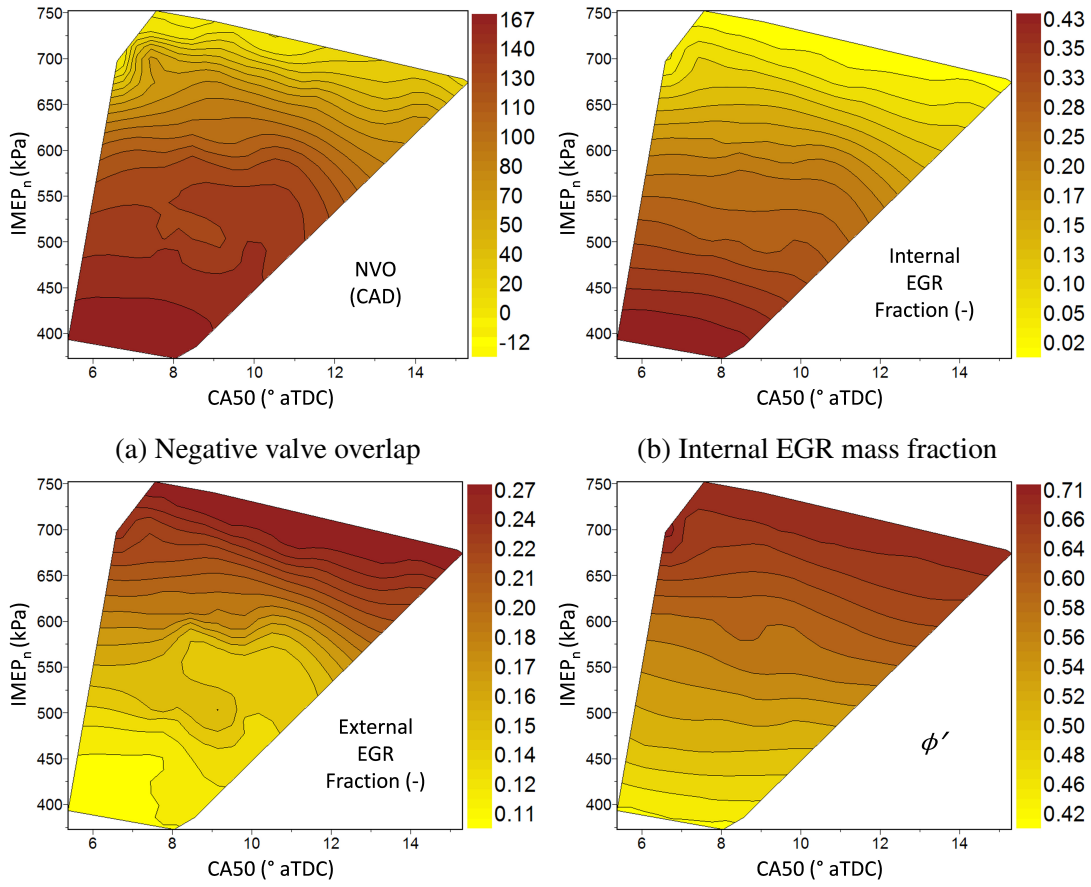

(a) Negative valve overlap

(b) Internal EGR mass fraction

(c) External EGR mass fraction

(d) 'Fuel-to-charge' equivalence ratio ϕ'

Figure 3.26: Mixture composition for SACI combustion as load is increased, (a) NVO, (b) internal EGR mass fraction, (c) external EGR mass fraction, and (d) ϕ'

overlap was achieved, resulting in a very small internal residual fraction, seen in Figure 3.26b. Figure 3.26c shows that the external EGR fraction increased with load to dilute the charge, maintain a stoichiometric mixture, and further suppress the onset of knock. While external EGR increased with load, internal EGR decreased more substantially, resulting in a reduction in the total EGR dilution level as load increased. This reduction is reflected in the increase in ϕ' with load, seen in Figure 3.26d.

The ringing intensity, evaluated using Eng's expression in Equation 2.33 [23], appears to be greatest at low load conditions with advanced CA50, as seen in Figure 3.27a. At these points, the combustion still greatly resembled HCCI due to elevated unburned gas temperatures, and the majority of the charge was consumed via auto-ignition, resulting

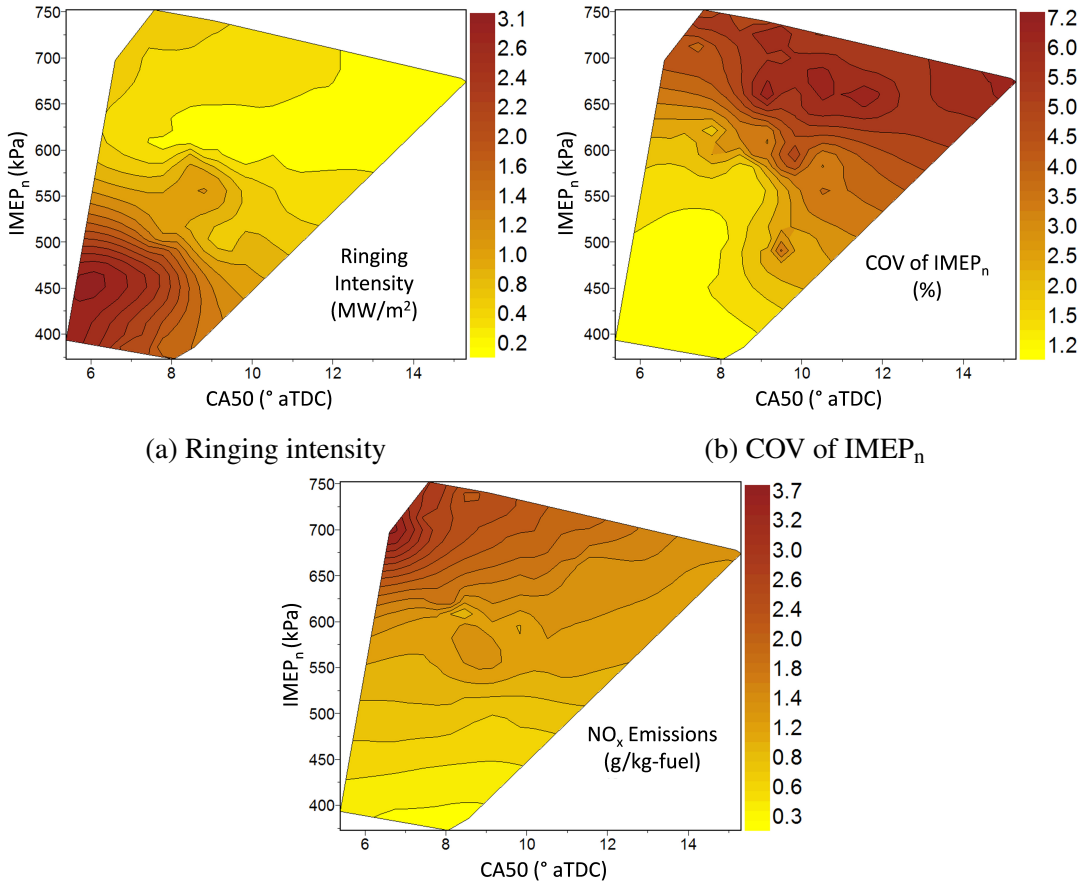

(a) Ringing intensity

(b) COV of IMEP$_n$

(c) NO$_x$ emissions

Figure 3.27: Combustion characteristics of the SACI regime, including (a) ringing intensity, (b) COV of IMEP$_n$, and (c) NO$_x$ emissions

in high rates of pressure rise. As noted earlier, as load increased and flame propagation became more prominent, end-gas knock began to occur, likely due to the engine's high compression ratio. Despite its audible nature, this type of knock is not captured by Eng's metric, as it occurs intermittently from cycle-to-cycle, resulting in relatively low average rates of pressure rise. Eng's metric appears to only be an appropriate measure of potentially harmful energy release for a dilute charge that ignites more or less simultaneously. On the other hand, end-gas knock refers to the auto-ignition of a small portion of the charge with a relatively high local energy content (ϕ'). It is clear that new metrics are required to account for features of multi-mode SACI combustion.

Figure 3.27b depicts the combustion stability as quantified by the COV of IMEP$_n$

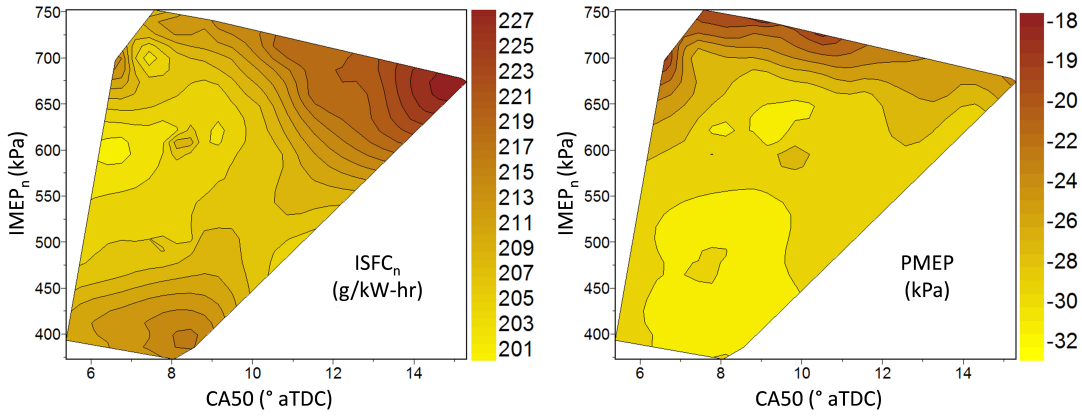

(a) ISFC$_n$ (b) PMEP

Figure 3.28: Efficiency characteristics in the SACI regime, (a) ISFC$_n$ and (b) PMEP

throughout the SACI regime. In an attempt to avoid end-gas knock at high load operation, the spark was retarded, resulting in late and unstable combustion. It is possible, however, that more stable operation could have been achieved at these high load conditions had the knocking intensity been properly quantified. In the present study, the conditions at IVC were set to completely avoid end-gas knock and potential damage to the engine structure. Figure 3.27c shows that NO_x emissions increased significantly with load, likely resulting from the increase in burned gas temperatures at lower dilution levels (higher ϕ') seen in Figure 3.20.

Figure 3.28a shows the variation in net indicated specific fuel consumption (ISFC$_n$) with load and combustion phasing. As CA50 occurs later in the cycle, ISFC$_n$ increases due to decreased expansion work. ISFC$_n$ is especially high at the highest load conditions, possibly due to the increased COV of IMEP$_n$ encountered at these points. The increase in ISFC$_n$ at low loads is explained by the increase in pumping work resulting from a high degree of negative valve overlap, seen in Figure 3.28b. As load increases and NVO decreases, PMEP decreases and ISFC$_n$ becomes increasingly affected by combustion phasing. It is seen that the contours of low ISFC$_n$ move to later CA50 as load increases and the combustion becomes more 'SI-like'. These results are consistent with the findings of Lavoie et al. [65], which suggest that optimal combustion phasing occurs slightly later as burn duration

increases.

To gage the benefits of dilute combustion (HCCI, SACI) over conventional throttled SI for a given load level, it is convenient to compare differences in gross thermodynamic efficiency, defined as the gross engine work output divided by the total fuel energy release (i.e. the injected fuel multiplied by the combustion efficiency). Figure 3.29 compares experimentally measured gross thermodynamic efficiencies (from FFVA engine data) to model predictions from Lavoie et al. [65] for a naturally-aspirated 4-cylinder gasoline direct injected engine with a compression ratio of 12:1. Simulations were run at optimal combustion phasing (CA50) for a burn duration of 25° CA [65]. The model predicts efficiencies for three different methods of load control: air dilution, EGR dilution, and conventional throttling, shown in Figure 3.29. Efficiency is plotted against $IMEP_g$.

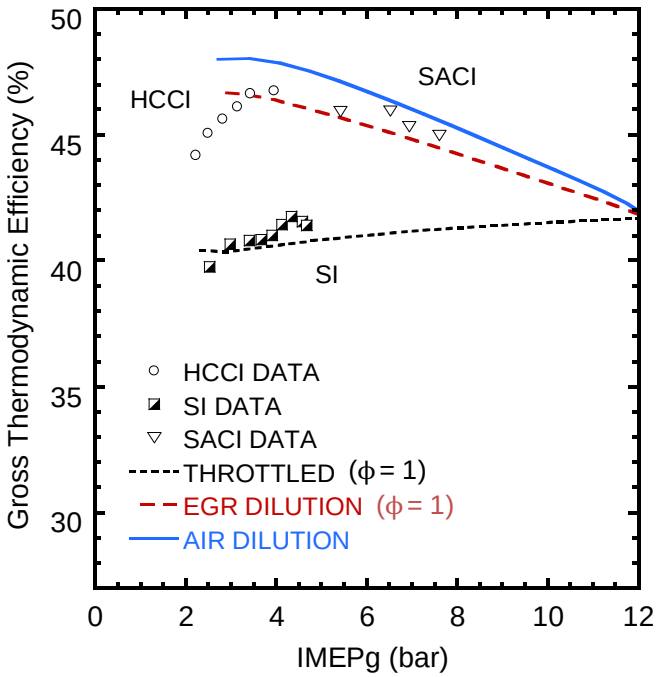

Figure 3.29: Gross indicated thermodynamic efficiency vs. $IMEP_g$ for measured HCCI, SACI, and low load SI combustion data, along with model predictions from Lavoie et al. [65] for various methods of load control

The HCCI points were taken from Figure 3.2b at a CA50 of 3.5° after TDC, while the SACI points were taken from Figure 3.17. Several conventionally throttled SI points

were also collected and included in the diagram for comparison. For these SI points, CA50 was held constant at 10° after TDC (to achieve near maximum efficiency), and less than 5 bar $IMEP_n$ was reached before severe knock was encountered. As such, stoichiometric SI with little to no dilution (ϕ and $\phi' = 1$) is severely limited on this engine due to its high compression ratio.

Overall, the model is in good agreement with the experiments and confirms the relative thermodynamic benefit of dilute mixtures compared to throttled stoichiometric SI combustion. This effect is caused by changes in mixture properties since pumping losses do not directly affect gross efficiency. The HCCI points exhibit substantial thermodynamic efficiency gains over the throttled SI points due to dilute operation (with a combination of air and residual gas) and a higher γ. However, the low load HCCI region exhibits a decrease in efficiency compared to the predicted values. Thermodynamic analysis of these HCCI data points suggests that the drop-off in efficiency is likely due to increased unburned temperatures provided by a very large internal residual fraction, resulting in a decrease in γ and cycle efficiency [65]. Additionally, cylinder blowby could be contributing to this behavior, as the blowby mass becomes a larger fraction of the total mass for lower load operation.

When transitioning into the SACI region, ϕ is purposely made equal to 1 (for NO_x after-treatment) through the addition of external EGR. The calculated efficiencies of the SACI points are within $\pm$ 2% of the predicted values for EGR dilute operation and remain above 45% absolute for the maximum load level achieved ($\sim$7.6 bar $IMEP_g$). Although throttled SI data were not attainable at the same high load conditions as the SACI data, the SACI data appear to demonstrate a 4-5% absolute ($\sim$12% relative) increase in gross thermodynamic efficiency compared to throttled SI at 5 bar $IMEP_g$.

3.4 Summary and Conclusions

Load extension into the SACI regime was accomplished using a combination of spark assist, internal EGR, and cooled external EGR to control rates of pressure rise and heat release at a given fueling level. With SACI, it was seen that 'slow' flame propagation and 'fast' auto-ignition can exist together in dilute, preheated conditions, offering substantial increases in burn duration that are unattainable with purely auto-igniting combustion at constant phasing. Stable, dilute, and efficient combustion was achieved with SACI at loads significantly above the allowable limits of naturally-aspirated HCCI, providing a pathway of transition from pure HCCI auto-ignition at low loads to pure SI flame propagation at high loads. Although NO_x emissions exceeded 1.0 g/kg-fuel, throughout most of the SACI regime, conventional after-treatment could be used due to the stoichiometric nature of the fuel-air mixture. At high load operation, the ringing intensity of Eng [23] was inappropriate for evaluating the ringing/knock intensity, and other metrics should be evaluated to better understand the dangers of end-gas 'knock' at high load SACI conditions.

The single variable sweeps of spark advance and T_{IVC} simultaneously modified the combustion phasing and burn duration of SACI, similar to sweeping NVO with pure HCCI. An advance in spark timing and/or T_{IVC} increased the ringing/knocking potential of SACI combustion, whereas stability was decreased via spark retard and/or a decrease in T_{IVC}. It was shown that CA50 responded more sensitively to changes in T_{IVC} (via NVO) than to changes in spark advance. Spark timing is a valuable control parameter, allowing the phasing of a primarily auto-igniting charge to be varied without changing the initial state at IVC, as is necessary in HCCI combustion.

Chapter 4

The Effects of Spark Timing, Unburned Gas Temperature, and Negative Valve Overlap on SACI Burn Rates

A more fundamental study of SACI burn rates was performed for stoichiometric EGR dilute SACI at constant combustion phasing and load ($\sim$6.5 bar $IMEP_n$). In this chapter, it is shown that the ratio of flame deflagration to auto-ignition heat release (and hence, overall burn duration) can be altered by controlling both spark timing and unburned gas temperature (T_u) via changes in internal and external EGR rates. Internal EGR was controlled by varying the degree of negative valve overlap (NVO). For the range of NVO investigated, potential variations in thermal and compositional stratification were found to have a weak effect on SACI burn characteristics.

4.1 Experimental Objective

From previous studies in Chapter 3, it is apparent that SACI combustion phasing at a constant fueling rate can be manipulated by several variables, including spark advance and temperature at IVC. As combustion phasing is advanced, overall burn duration decreases and ringing intensity increases. On the other hand, as phasing is retarded, burn duration increases and combustion becomes more unstable. By adjusting only one variable at a time (i.e. spark advance [36, 109] *or* temperature at IVC [50]), independent control over combustion phasing and burn duration cannot be demonstrated. In order to modify SACI heat

release behavior at a constant phasing and fueling rate, both spark advance and temperature at IVC must be varied simultaneously.

Yun et al. [50] showed that maximum pressure rise rates within the SACI regime could be controlled at a constant CA50 by simultaneously varying spark timing and adjusting the ratio of internal (via NVO) to external EGR. As spark advanced, the ratio of internal to external EGR was reduced to lower the temperature at IVC and maintain phasing, and the initial heat release rates (thought to represent flame propagation) became more gradual. This effect led to an increase in overall burn duration, causing both peak rates of pressure rise and combustion stability to decrease.

While Yun et al. [50] noted the effects of this approach on combustion rates, their study lacked detail on the key thermodynamic properties affecting and resulting from the combustion process, such as the cylinder temperature prior to spark ignition, locations of spark and end-gas ignition, and peak burned gas temperatures, along with the resulting impact of the combustion process on indicated thermal efficiency and emissions. In addition, this study did not decouple the potential effects of thermal and compositional stratification associated with NVO variations from the spark timing and unburned gas temperature variations. In this chapter, many of these shortcomings are addressed for SACI operation at constant CA50 and various spark timings and unburned gas temperatures. Detailed analysis of the experimental data is conducted to better understand the interplay between the unburned temperatures near the time of spark, the onset of auto-ignition, and the resulting tradeoff between deflagrative and auto-ignition combustion modes.

4.2 Experiments with Varying Spark Advance and Unburned Gas Temperature at Constant Combustion Phasing

For this study, SACI experiments were performed at a constant fueling rate and combustion phasing (CA50) by varying both spark timing and unburned gas temperature (T_u). Fueling was maintained at 19 mg/cycle, corresponding to a load of ∼6.5 bar $IMEP_n$, well beyond the high load limit of HCCI. Intake temperature and engine speed were also held constant at 45°C and 2000 rpm, respectively. Table 4.1 lists the operating conditions for this spark/T_u sweep.

Parameter	*Value*
Engine speed (rpm)	2000
Fuel flow rate (mg/cycle)	19.0
Fuel-to-air equivalence ratio, ϕ	1.0
Fuel pressure (bar)	∼100
Intake pressure (bar)	1.0
Exhaust pressure (bar)	1.05
Intake temperature (°C)	45
Negative valve overlap (° CA)	114-136
Intake valve closing (° bTDC)	150
Exhaust valve opening (° aTDC)	150
Valve lift (mm)	6.0
Coolant temperature (°C)	90
Oil temperature (°C)	90
Spark advance (° bTDC)	25-44
Spark energy from the coil (mJ)	70
Start of fuel injection (° bTDC)	330
External EGR, measured in intake manifold (%)	17.4-23.1
EGR coolant temperature (°C)	55

Table 4.1: Experimental conditions during the spark/T_u sweep

Unburned gas temperature was increased by trading cooled external EGR for an equal fraction of hot internal residual (via NVO) to maintain a stoichiometric equivalence ratio (ϕ = 1.0). Although the ratio of internal to external EGR varied, the total residual fraction

remained constant at about 40%, as seen in Figure 4.1. Spark timing was then retarded to compensate for this increase in unburned charge temperature and maintain CA50 at ∼9° after TDC. This CA50 was chosen to provide near maximum thermal efficiency, which has been shown to decrease as CA50 is advanced or retarded away from this high efficiency phasing [9, 65]. Lavoie et al. [65] showed that combustion with conventional heat transfer is most efficient if CA50 falls between 7° and 10° after TDC, depending on burn duration.

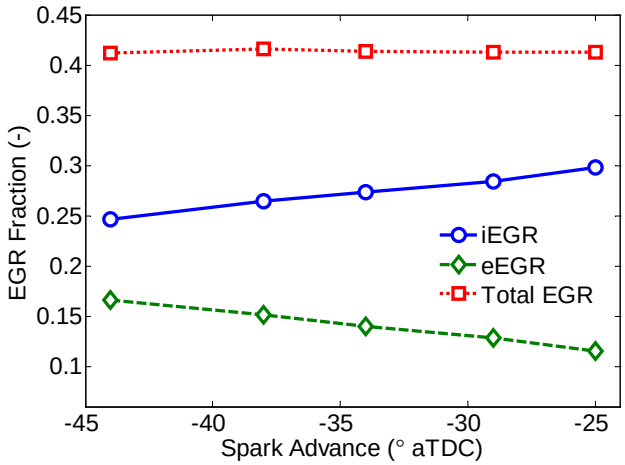

Figure 4.1: Strategy for controlling SACI burn characteristics for the spark/T_u sweep at constant CA50 - simultaneous variation of residual composition (ratio of internal to external EGR) and spark advance while maintaining total EGR dilution rate and $\phi = 1$

Figure 4.2 shows that as the ratio of internal to external EGR increased, the estimated cylinder temperature at IVC increased by about 25 K. This figure also indicates that the spark needed to retard by 19° CA between the lowest and the highest unburned temperature cases in order to maintain CA50. Similar spark timings within the SACI regime have been previously reported [50, 51].

The cylinder pressure and mass-averaged temperature curves for the spark/T_u sweep are seen in Figures 4.3a and 4.3b, respectively. The case with the highest IVC temperature has the most retarded spark timing at 25° before TDC, while the case with the lowest IVC temperature has the most advanced spark timing at 44° before TDC. It is also clear from Figures 4.3a and 4.3b that the case with the lowest IVC temperature exhibits the lowest

peak pressure and temperature rise rates.

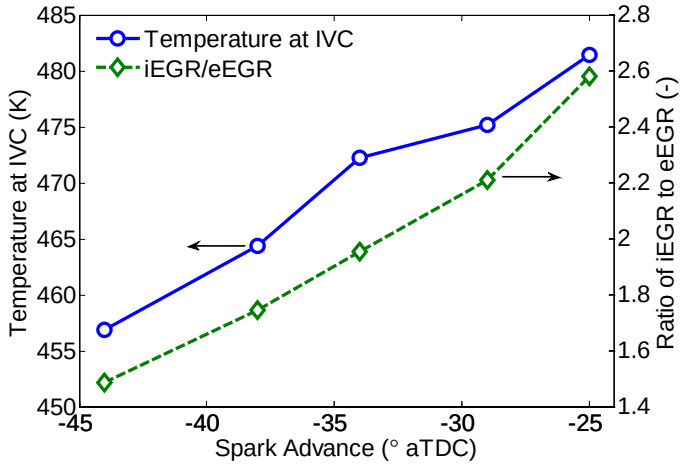

Figure 4.2: The ratio of internal to external EGR and the temperature at IVC vs. spark advance for each case of the spark/T_u sweep - as the temperature at IVC increases the spark must retard to maintain CA50

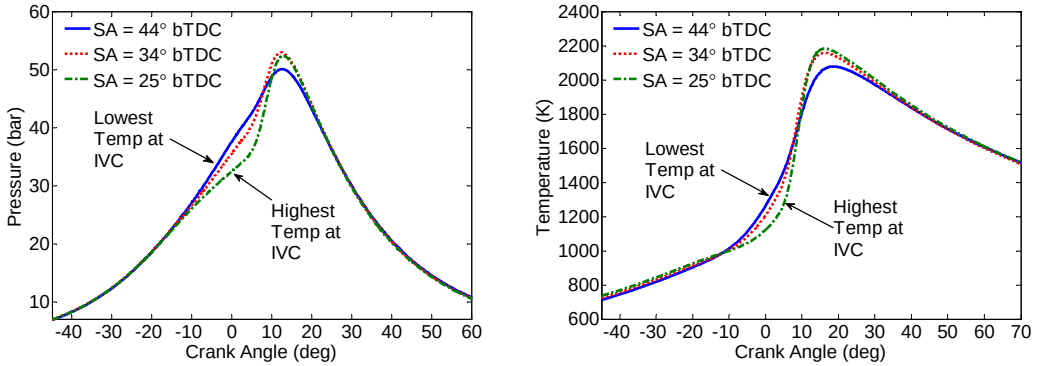

(a) Cylinder pressure

(b) Cylinder mean temperature

Figure 4.3: (a) Cylinder pressure and (b) mass-averaged cylinder temperature curves at constant load (∼6.5 bar $IMEP_n$) and CA50 (∼9° after TDC) for the spark/T_u sweep

Taking a closer look at the temperature curves in Figure 4.4, it becomes clear that the case with the highest fraction of internal EGR has consistently higher temperatures prior to spark ignition than the case with the highest fraction of external EGR. The dots on each curve represent the time of spark, which must advance as the unburned temperature decreases. This spark advance compensates for the decrease in temperature by allowing

more time for flame based heat release to compress the surrounding mixture to the point of auto-ignition, thereby maintaining combustion phasing. Had the spark not been advanced as unburned temperature decreased, CA50 would have retarded.

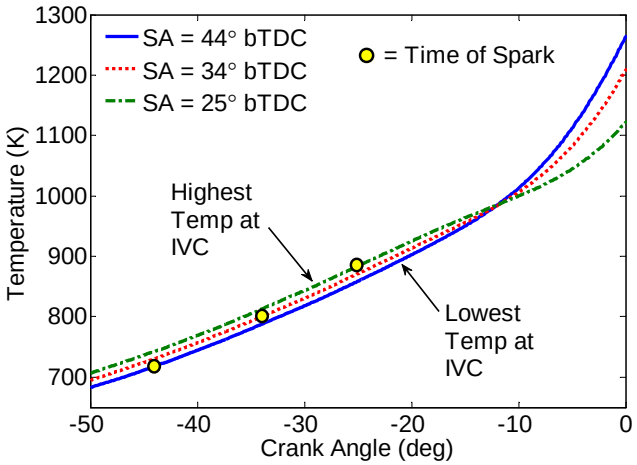

Figure 4.4: Closer view of the mass-averaged cylinder temperature curves at spark ignition for the spark/T_u sweep (dots on each curve represent the time of spark)

With this strategy, it is indeed possible to control SACI burn duration and heat release rates at a constant CA50, as seen in Figure 4.5a. The use of such a strategy clearly addresses one of the major shortcomings of low temperature HCCI combustion, that is the lack of independent control over combustion phasing and burn rate. The lowest unburned temperature case (highest fraction of external EGR) with the most advanced spark timing appears to have the largest fraction of flame based heat release (defined below) as well as the longest burn duration, which is explained by the fact that flame propagation heat release generally occurs at a much slower rate than bulk auto-ignition. The peak rate of heat release for this case is also $\sim$40% lower than the peak rate of heat release for the highest T_u case.

By estimating the crank angle at which auto-ignition occurs (using the method discussed in Chapter 2), the fraction of mass consumed by the flame can be determined from the mass fraction burned curve, seen in Figure 4.5b. The fraction of flame based heat release is highest for the case with the lowest IVC temperature, with $\sim$34% of the mass burned by

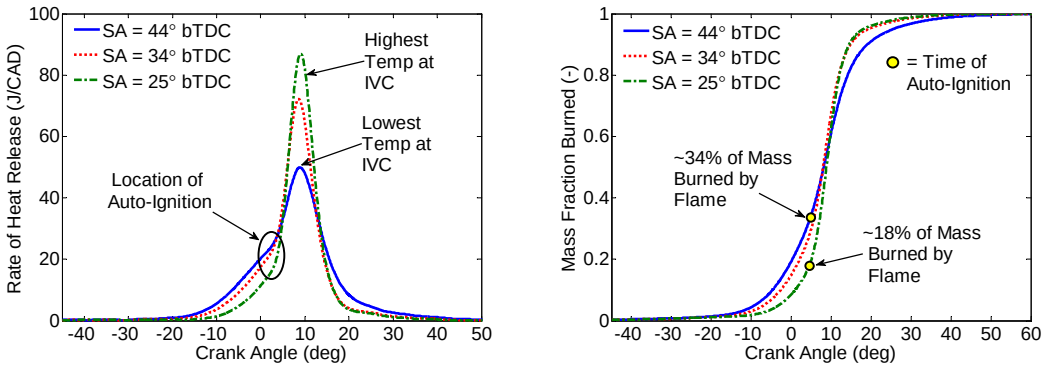

(a) Rate of heat release

(b) Mass fraction burned

Figure 4.5: (a) Rate of heat release and (b) mass fraction burned curves for each case of the spark/T_u sweep (dots represent the location of auto-ignition)

the flame. This case also has the most advanced spark timing, allowing the flame more time to propagate before the end-gas reaches the temperature required for auto-ignition. For the case with the highest IVC temperature, $\sim$18% of the mass is burned by the flame, since the unburned gas temperature is sufficiently high to promote auto-ignition soon after flame propagation has begun. Therefore, a larger percentage of the total fuel energy is released during bulk auto-ignition and a higher peak rate of heat release is seen. This inverse correlation between the fraction of mass burned by flame and the peak rate of heat release is seen in Figure 4.6.

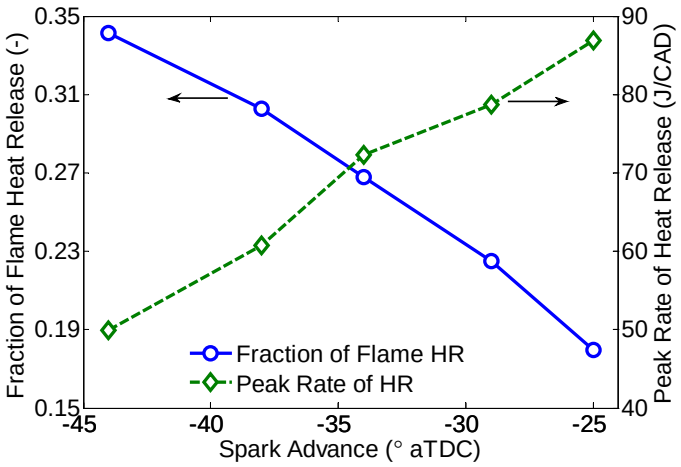

Figure 4.6: Fraction of flame heat release and peak rate of heat release vs. spark advance for the spark/T_u sweep

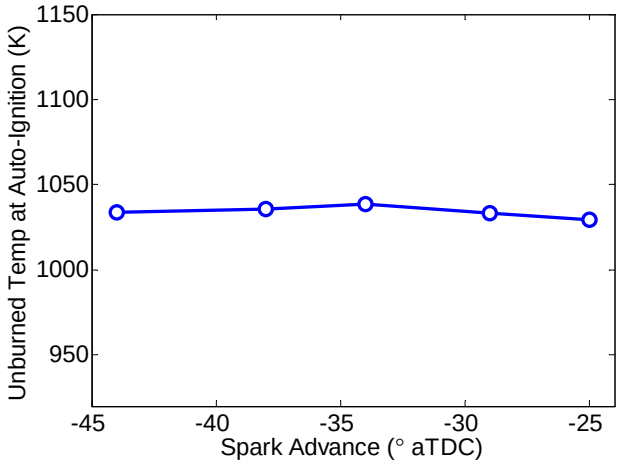

Figure 4.7: Unburned gas temperature (T_u) at the onset of bulk auto-ignition for the spark/T_u sweep

Using a two-zone heat release analysis, the unburned gas temperature at the onset of bulk auto-ignition was estimated and plotted in Figure 4.7. Interestingly, the temperature at which auto-ignition occurs for each case is $\sim$1040 K. As seen in Figure 4.2, the maximum discrepancy in IVC temperature between cases is 25 K ($\sim$5%), while the peak difference in auto-ignition temperature is only 9 K (less than 1%). This observation suggests that the location of auto-ignition depends very much on the temperature of the end-gas, regardless of spark timing and the fraction of flame based heat release. Since the goal of SACI is to use flame based heat release to compress the surrounding mixture to the point of auto-ignition, a more advanced spark is needed if the deflagration event begins at a lower unburned temperature. This advance in spark timing allows the end-gas to be further compressed by the flame front so that it can reach the required temperature for auto-ignition. While the temperatures at auto-ignition in Figure 4.7 seem reasonable, it is possible that they are slightly underpredicted by the two-zone model. By assuming an instantaneous transition between flame propagation and auto-ignition, the analysis cannot account for low temperature heat release in the end-gas prior to thermal runaway. It is possible that this error is more pronounced for some cases than for others.

To better understand the relationship between the initial flame based heat release and

mass fraction burned, estimates of laminar flame speed S_L were made using the correlation by Middleton et al. [89] discussed in Chapter 2. This correlation relies on the unburned gas temperature (T_u), cylinder pressure and composition of the mixture at the point of interest, which in this case was 15° after (spark) ignition timing (AIT). This timing was selected based upon an optical engine flame study of conventional SI combustion by Aleiferis et al. [73]. In this study, the experimentally observed flame growth rate at 15° AIT showed good agreement with calculated S_L, indicating that the flame was not highly wrinkled, and was strongly correlated to the 0-5% mass fraction burned interval. At this timing, a clear minimum in flame growth rate was seen, indicating that flame speeds were no longer influenced by the spark discharge event. Other researchers [110, 111] have noticed similar minima in the vicinity of 1-2 ms AIT, in which flame growth becomes increasingly affected by strain, local flow fields, and laminar burning velocity (a function of the thermodynamic state and composition), and less by the spark plasma. For the experiments presented here, the spark discharge duration is on the order of $\sim$10°; therefore, estimating laminar flame speeds at 15° AIT seems appropriate.

In the current work, similar results to [73] were found under highly dilute combustion conditions. Figure 4.8a shows the unburned gas temperature at 15° AIT decreases by $\sim$160 K as the spark is advanced, resulting in a significant decrease in the estimated S_L at the same location. Cylinder pressure also decreases as spark is advanced (which would act to increase S_L); however, these effects are far outweighed by those of temperature [112]. This S_L decrease is accompanied by an increase in the 0-5% mass fraction burned duration, seen in Figure 4.8b. Although turbulence is likely affecting flame growth rates in this region (e.g. through aerodynamic stretching of the flame kernel), the increase in 0-5% burn duration appears to be due in part to the effect of S_L on initial flame growth. The slower initial flames seen in Figure 4.8b further support the need for advancing the spark as the unburned temperature decreases.

The locations of 5% mass fraction burned, 10% burned, auto-ignition, 50% burned, and

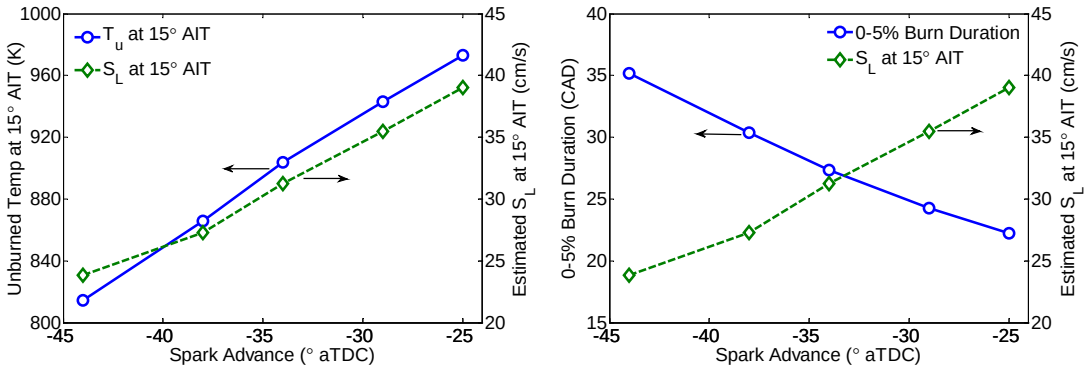

(a) T_u and S_L vs. SA (b) S_L and 0-5% Burn vs. SA

Figure 4.8: Correlations of (a) unburned gas temperature (T_u) and (b) 0-5% burn duration with the predicted S_L from the correlation by Middleton et al. [89] at 15° after spark ignition timing

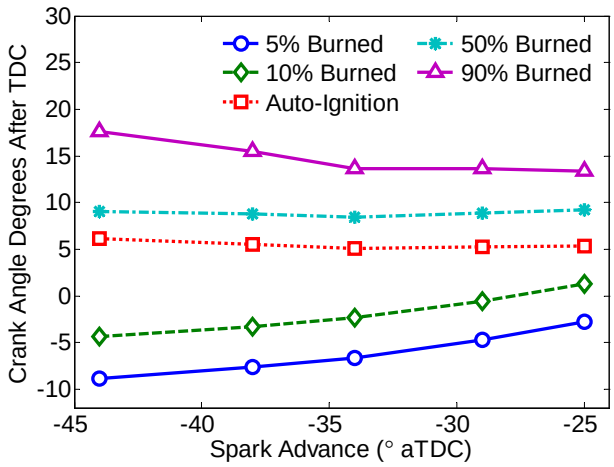

Figure 4.9: Crank angle locations at the time of 5% mass fraction burned, 10% burned, auto-ignition, 50% burned, and 90% burned for the spark/T_u sweep

90% burned were then plotted for every case in Figure 4.9. The location of 50% burned is constant for every case, in accordance with the control strategy, and the crank angle at which the main auto-ignition event begins is relatively similar between cases (within one crank angle degree). However, as seen in Figure 4.5a, it appears that the rates of auto-ignition become slower as the T_u at the time of spark decreases and the fraction of flame based heat release increases. This behavior is reflected in the increased 50-90% burn durations in Figure 4.9. It is possible that, for these lower T_u cases, the increased fraction of deflagrative heat release required for compression heating enhances the level

of thermal stratification in the end-gas, thereby affecting the rates of auto-ignition. For a higher fraction of flame based heat release, the mass consumed by auto-ignition resides closer to the cylinder wall and could include a relatively larger fraction of low temperature zones. These zones could act to slow the heat release in the end-gas, thereby contributing to an increase in the 50-90% burn duration. The slower burn rates could be further augmented by cooling effects from a rapidly expanding piston. An experimental study by Sjöberg et al. [30] demonstrated slower HCCI burn rates with an increased thermal gradient resulting from cooler wall temperatures, while optical engine SACI experiments by Zigler et al. [46] showed that auto-ignition sites appeared with increasing frequency as preheat temperatures increased and the fraction of mass consumed by flame decreased.

Based on the results in Figure 4.9, the case with the lowest IVC temperature and most advanced spark timing demonstrates the longest 0-50% and 0-90% burn durations for a few reasons. First, the combustion process must be initiated earlier in the cycle to account for slower initial rates of flame propagation due in part to decreased S_L. Second, this case requires the greatest amount of time for flame based heat release to promote end-gas auto-ignition due to a lower T_u (and flame propagation is inherently slower than bulk auto-ignition), and third, the rates of end-gas auto-ignition decrease, possibly due to increased levels of thermal stratification introduced by a larger fraction of flame heat release.

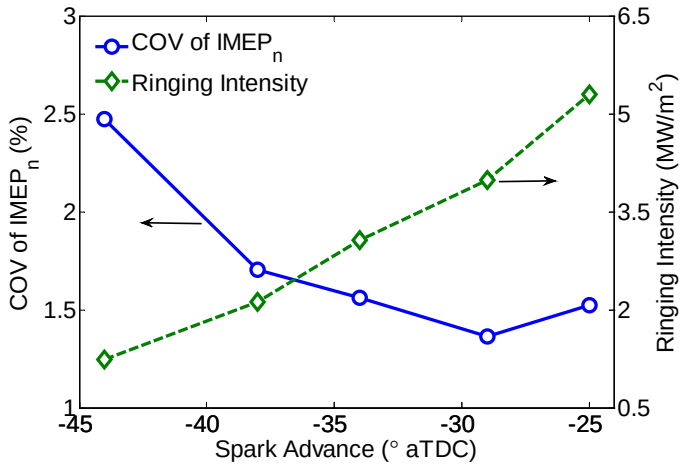

Figure 4.10: Variation in ringing intensity and COV of IMEP$_n$ for the spark/T_u sweep

The ability to manage the fraction of flame heat release at constant phasing is also advantageous in terms of operational constraints. Variations in ringing intensity and COV of $IMEP_n$ are seen in Figure 4.10, plotted against the corresponding spark advance for each case. As T_u decreases and more mass is consumed by the flame, peak rates of pressure rise and peak rates of heat release decrease, and ringing intensity decreases by $\sim$75%, from 5.3 MW/m^2 to 1.2 MW/m^2. On the other hand, the COV of $IMEP_n$ increases, nearing the limit of 3.0%. This increase in unstable behavior could be due to inhomogeneities of temperature, composition, and flow velocity within the vicinity of the spark plug, and these inhomogeneities could increase at earlier spark timings, thus affecting flame development [113]. For lower unburned temperature cases, auto-ignition also becomes more dependent on compression heating from the flame. High variability in initial flame development could result in high variability in the start of auto-ignition and combustion phasing. Additionally, the slower rates of end-gas auto-ignition could contribute to the increased instability.

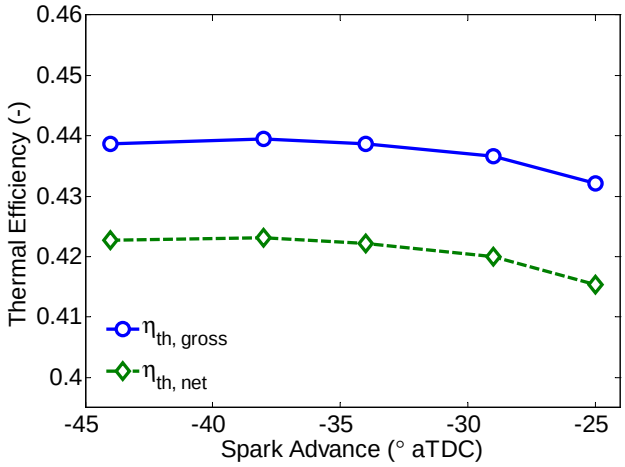

Figure 4.11: Variation in indicated thermal efficiency for the spark/T_u sweep

As seen in Figure 4.11, unburned temperature and spark advance can be used to manipulate combustion behavior and reduce pressure rise rates without compromising thermal efficiency. For this set of data, the gross and net indicated thermal efficiencies remained fairly constant despite major changes in burn duration and combustion stability. In fact, the

most advanced spark timing case, which has the longest burn duration and highest COV of $IMEP_n$, actually appears to be slightly better from an efficiency standpoint than the most retarded spark timing case, possibly due to lower heat losses to the cylinder wall due to lower peak temperatures, seen in Figure 4.3b, or reduced heat loss associated with lower ringing intensity [105]. These lower temperatures could also result in a higher ratio of mixture specific heats γ, acting to further increase thermal efficiency [65].

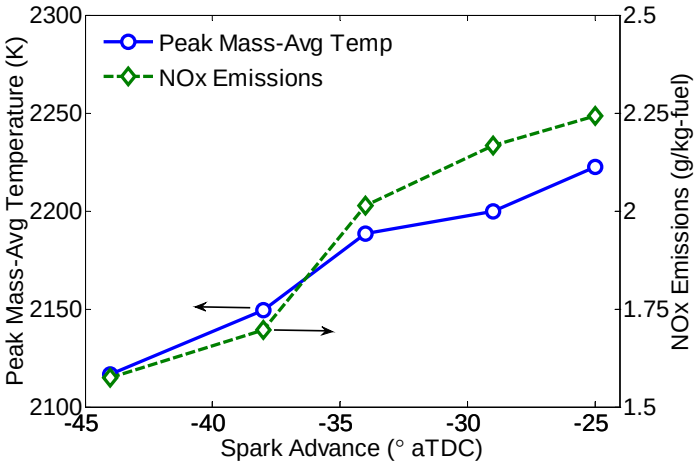

Figure 4.12: Variation in peak mass-averaged cylinder temperature and NO_x emissions for the spark/T_u sweep

Lower peak temperatures also reduce engine-out NO_x, as seen in Figure 4.12. For a given mixture composition, a decrease in the unburned gas temperature corresponds to a decrease in the burned gas temperature, leading to a reduction in NO_x. At this load condition, NO_x emissions typically exceed the limit of 1.0 g/kg fue; however, these emissions can be treated with a standard three-way catalyst due to the stoichiometric nature of the mixture.

4.3 Experiments at Constant Spark Timing and Combustion Phasing with Varying NVO

As discussed in Chapter 1, it is well known that the use of internal EGR can enhance in-cylinder thermal and compositional stratification [26, 27]. In this experiment, the external EGR was introduced into the air system well upstream of the intake runner; the incoming air and external EGR are expected to be well-mixed, while the internal EGR and fresh charge are not. To understand the effect of potential differences in in-cylinder mixing and thermal/compositional non-uniformities associated with the use of NVO and internal EGR, an additional experiment was conducted where internal and external EGR rates were traded off at constant combustion phasing and overall EGR dilution level.

For the additional study, internal EGR (via NVO) was exchanged for preheated external EGR (eEGR) at a constant spark advance of 30° before TDC. For the spark/T_u sweep, NVO changed by a total of ∼20 crank angle degrees (seen in Table 4.1) in order to vary the unburned temperature within a desired range. For this additional experiment, a similar range of NVO was targeted. Table 4.2 lists the operating conditions for this NVO/preheated eEGR sweep, the purpose of which was to determine if any change in combustion characteristics resulted solely from a small (∼20° CA) change in NVO.

To isolate the effects of mixing from those of unburned temperature, mixture composition (masses of fuel, air, and residual) and temperature at IVC were held approximately constant while NVO was varied, as seen in Figures 4.13a and 4.13b, respectively. Figure 4.13a shows that as NVO decreased from 130 to 104 crank angle degrees (a slightly larger range than that shown in Table 4.1), internal EGR decreased and external EGR was increased to maintain a stoichiometric equivalence ratio. At the same time, intake temperature was increased by ∼50°C to compensate for the loss in thermal energy (from internal EGR) and maintain a constant CA50 at ∼9° after TDC.

As seen in Figure 4.13a, the total estimated EGR fraction decreases slightly (from ∼40-38%) as intake temperature increases in order to maintain a stoichiometric mixture. Since

Parameter	*Value*
Engine speed (rpm)	2000
Fuel flow rate (mg/cycle)	19.0
Fuel-to-air equivalence ratio, ϕ	1.0
Fuel pressure (bar)	$\sim$100
Intake pressure (bar)	1.0
Exhaust pressure (bar)	1.05
Intake temperature (°C)	45-95
Negative valve overlap (° CA)	104-130
Intake valve closing (° bTDC)	150
Exhaust valve opening (° aTDC)	150
Valve lift (mm)	6.0
Coolant temperature (°C)	90
Oil temperature (°C)	90
Spark advance (° bTDC)	30
Spark energy from the coil (mJ)	70
Start of fuel injection (° bTDC)	330
External EGR, measured in intake manifold (%)	17.4-18.6
EGR coolant temperature (°C)	55

Table 4.2: Experimental conditions during the NVO/preheated eEGR sweep

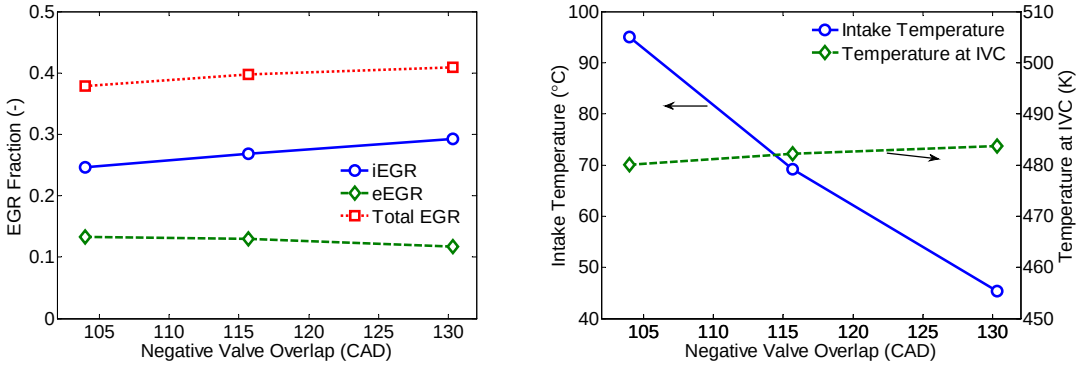

(a) EGR mass fractions

(b) Temperatures at intake and IVC

Figure 4.13: Control strategy for the NVO/preheated eEGR sweep - (a) vary the ratio of internal to external EGR at a constant spark advance (30° before TDC) and (b) increase intake temperature as NVO decreases to maintain temperature at IVC and CA50 ($\sim$9° after TDC)

fueling rate and equivalence ratio were held constant (fuel was injected directly into the cylinder), this decrease in EGR fraction corresponds to a decrease in total EGR mass, hence the total in-cylinder mass decreases. This change is possibly due to a slight decrease in the observed pressure at IVC that may be related to variations in flow dynamics induced by the higher intake temperatures. This change in mass, however, is rather small and should not drastically affect combustion behavior. The temperatures at IVC, seen in Figure 4.13b, are approximately constant for each case, differing by less than 1%. Considering that the spark advance, CA50, mixture composition, and temperature at IVC are held essentially constant while NVO varies in this particular study, if thermal and compositional stratification differences associated with NVO variations significantly influenced flame propagation or auto-ignition, then it would be expected that variations in burn duration would be observed.

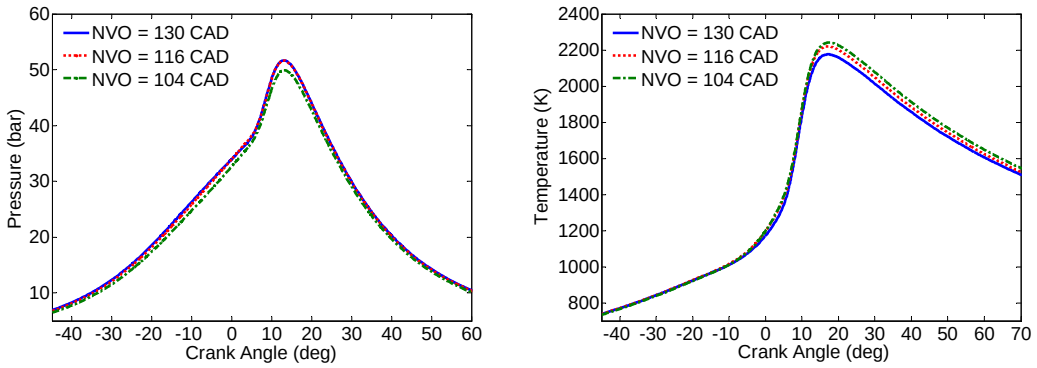

(a) Cylinder pressure

(b) Cylinder mean temperature

Figure 4.14: Curves of (a) cylinder pressure and (b) mass-averaged cylinder temperature at constant spark advance (30° before TDC) and CA50 (∼9° after TDC) for the NVO/preheated eEGR sweep

Figures 4.14a and 4.14b show the cylinder pressure and mass-averaged temperature curves for the cases of the NVO/preheated eEGR sweep described above. Due to the slight decrease in total mass and IVC pressure at increased intake temperatures, the compression pressure prior to combustion decreases slightly, resulting in less than a 2 bar (∼3%) decrease in peak pressure. The bulk temperature curves prior to combustion are in good agreement, as the estimated temperatures at IVC for each case are relatively constant. Im-

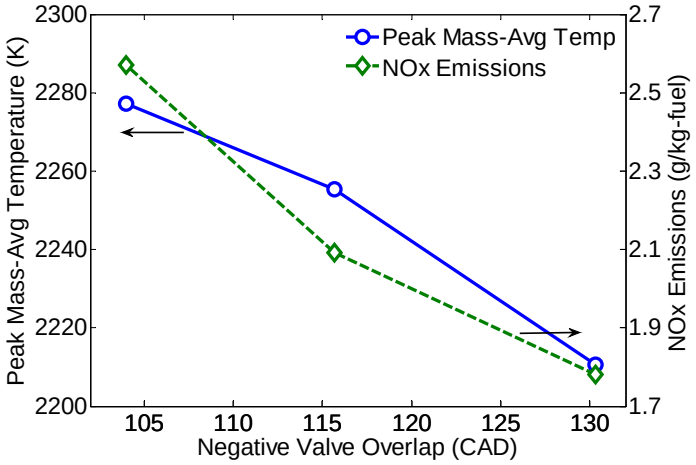

Figure 4.15: Variation in peak mass-averaged cylinder temperature and NO_x emissions for the NVO/preheated eEGR sweep

mediately following combustion, the temperature curves still agree well, however, peak temperatures increase by about 3% as intake temperature increases. Again, this result is likely caused by the decrease in estimated mass and dilution level for a constant fueling rate. With less diluent available to absorb the heat of the combustion reactions, peak temperatures increase and NO_x emissions increase, seen in Figure 4.15.

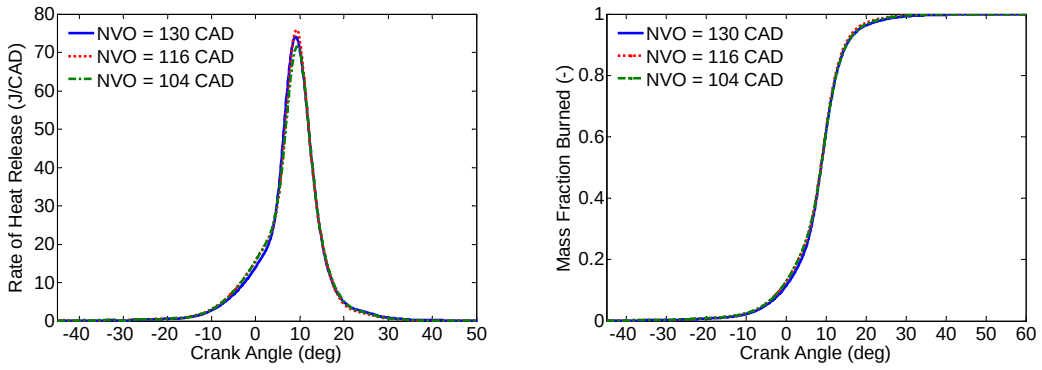

(a) Rate of heat release

(b) Mass fraction burned

Figure 4.16: (a) Rate of heat release and (b) mass fraction burned curves at constant spark advance (30° before TDC) and CA50 (∼9° after TDC) for the NVO/preheated eEGR sweep

Despite these small changes in peak pressure and temperature, the differences in the rates of heat release and mass fraction burned curves (seen in Figures 4.16a and 4.16b,

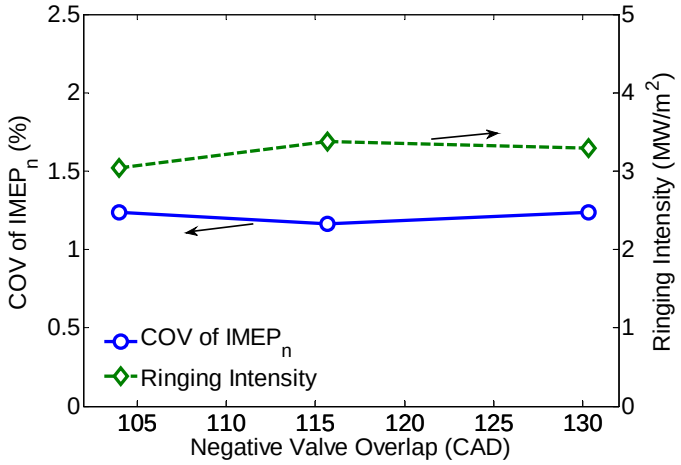

Figure 4.17: Variation in ringing intensity and COV of $IMEP_n$ for the NVO/preheated eEGR sweep

respectively) are fairly negligible. The peak rates of heat release between the cases differ by about 6%, but follow no consistent trend. The mass fraction burned curves are remarkably similar, especially when compared to those of the varying spark/T_u sweep, seen in Figure 4.5b. These results indicate that for the range of NVO examined and the corresponding change in internal EGR from ∼24.5% to 29% (∼18% relative), any change in mixture homogeneity (if it exists) has little to no effect on overall combustion behavior provided the global unburned temperature and mixture composition remain fixed. Even the values for ringing intensity and COV of $IMEP_n$ are quite similar between the cases, seen in Figure 4.17. These results verify that the trends seen in the spark/T_u sweep are due primarily to variations in spark advance and unburned temperature and any accompanying change in flame heat release fraction. The small range of NVO utilized in this experiment does not appear to introduce confounding mixing and/or stratification effects on combustion behavior.

4.4 Summary and Conclusions

Independent control of burn duration and combustion phasing was demonstrated by varying spark timing and unburned temperature (T_u) simultaneously within the SACI regime while holding composition approximately constant. As the unburned gas temperature decreased and spark advanced, a larger portion of flame based heat release and longer 0-90% burn durations were observed. The increase in deflagrative combustion decreased the fuel mass available for auto-ignition, causing a dramatic decrease in peak rates of heat release, ringing intensity, and combustion stability without compromising thermal efficiency. Any variation in mixedness associated with the range of NVO studied was found to have a negligible effect on combustion. The changes in SACI behavior were, therefore, caused primarily by changes in spark timing and temperature.

Bulk end-gas reactions began at a similar unburned zone temperature ($\sim$1040 K) for every case, regardless of the temperature at spark timing. The changes in spark timing with T_u resulted for two reasons. First, for colder charges, an earlier spark advance was required to increase the fraction of flame based heat release to provide the additional compression heating to promote auto-ignition. Second, the early flame based heat release rates following spark ignition decreased for lower T_u. This result can be attributed in part to the change in estimated laminar flame speeds at those conditions and their assumed effect on overall turbulent burning velocity.

Chapter 5

The Effects of Diluent Composition on the Rates of Spark Assisted Compression Ignition Combustion

In this chapter, the effect of unburned charge oxygen-to-fuel ratio on the rate of SACI combustion is examined. The charge oxygen-to-fuel ratio is modified at constant charge energy content, combustion phasing, and spark timing through the careful control of EGR rate and unburned gas temperature (T_u). A similar analysis to that in Chapter 4 is performed in order to better understand the influence of flame propagation and auto-ignition on overall SACI burn rates.

5.1 Previous Studies on the Effect of Diluent Composition on HCCI and SACI Combustion

Recent experimental and computational studies have examined the effects of increased levels of EGR on the rates of HCCI auto-ignition and SI/SACI flame propagation. In the analysis of their HCCI engine experiments where the mass fraction of external EGR in the incoming mixture was increased while all other input parameters were held constant, Dec et al. [11] attributed the retard in combustion phasing and the resulting degradation in combustion stability to the increase in the heat capacity (c_p) of the reactant mixture. The increased heat capacity caused the in-cylinder compression temperatures to decrease and auto-ignition to begin later in the cycle where it becomes more susceptible to high rates of

piston expansion. Dec et al. [11] also suggested that the initial burn rates are slowed by the decrease in O_2 concentration as excess air in the incoming charge is replaced with non-reactive products of combustion. Further studies have shown that excess O_2 can impact chemical reaction rates [7] thereby decreasing auto-ignition delay times [63].

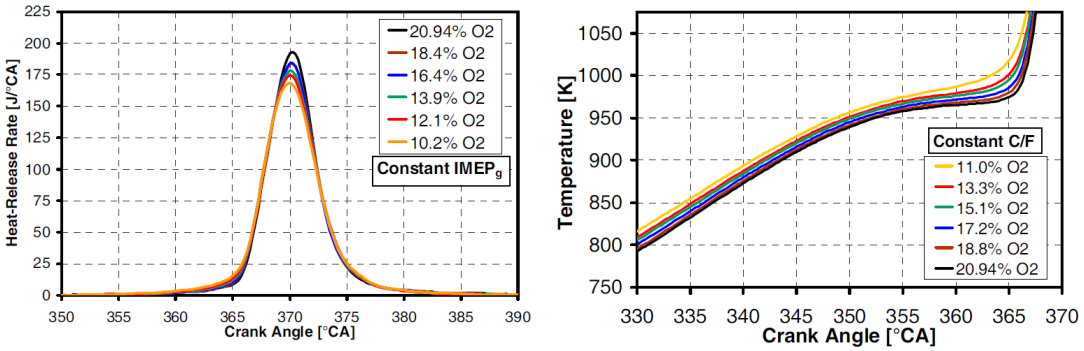

(a) Rate of heat release [11] (b) Cylinder mean temperature [11]

Figure 5.1: (a) Rate of heat release and (b) mass-averaged cylinder temperature curves for the HCCI study by Dec et al. [11] in which excess air dilution is replaced with EGR

The study by Dec et al. [11] also examined the effect of increased EGR dilution on the burn rates of HCCI at constant combustion phasing (CA50). As the fraction of external EGR was increased, the incoming charge temperature (including air and external EGR) was also increased to maintain CA50 at 10° after TDC. This increase in temperature decreased the incoming charge density and hence, the total inducted mass. Therefore, fueling rate was increased slightly to hold $IMEP_g$ constant. In comparing the rate of heat release curves, seen in Figure 5.1a, a slight increase in overall burn duration was seen for the cases with increased levels of EGR dilution, despite the fact that compression temperatures were purposely increased to compensate for the difference in mixture properties, seen in Figure 5.1b. The initial rates of heat release appear to occur more slowly for the more EGR dilute cases (possibly due in part to the increased c_p of the mixture); however, the process quickly transitions to thermal runaway, resulting in equally rapid burning rates for all cases regardless of mixture composition. From the mass-averaged temperature curves of Figure 5.1b, it appears that the auto-ignition event occurs rapidly and at $\sim$1000 K for each case.

These results show that for a premixed auto-igniting combustion mode, small changes in burn rate are possible through the manipulation of composition at constant phasing.

Recent computational work by Middleton et al. [89] has suggested that one dimensional laminar flames are highly affected by variations in mixture composition. It is widely accepted that the laminar flame speed (S_L) is strongly related to T_b, which depends on the overall composition of the mixture including the relative amounts of air and/or EGR dilution [114]. For a given fuel mass, T_u, P, and ϕ', the T_b of an air dilute mixture exceeds that of an EGR dilute mixture primarily due to differences in mixture heat capacity c_p [7]. According to Middleton's correlation, this higher T_b corresponds to a significantly higher computed S_L for air dilute flames [89]. In order to isolate the chemical effects of air dilution on S_L from the thermal effects, Middleton imposed a slightly higher (3%) fuel mass fraction for an EGR dilute case in order to match the computed T_b of an air dilute case. At these conditions, the S_L for the EGR dilute case was still found to be $\sim$17% lower than that of the air dilute case, and this decrease in burning velocity was attributed primarily to the effect of reduced O_2 concentration on flame chemistry [89].

The following study analyzes the effects of diluent composition (air vs. EGR) on the overall rates of SACI combustion as it relates to both flame propagation and auto-ignition. Throughout the literature, the method of dilution has varied considerably between experimental SACI studies. Some studies have focused on lean air dilute cases [46] while others have focused on stoichiometric EGR dilute cases [36, 50, 51, 115]. An explicit comparison of the effects of air dilution versus EGR dilution on SACI burn rates has yet to be performed, hence the effect of diluent composition on the behavior of SACI is relatively unknown. Based on current knowledge of the effects of composition on the rates of flame propagation [89] and auto-ignition [11], it is hypothesized that SACI burn rates will be significantly affected by varying levels of EGR in the diluent mixture. As in the previous chapter, a detailed analysis of the experimental data is conducted to understand the effects of mixture properties (including T_u and EGR rate) on the resulting initial 'flame based'

heat release rates, the onset of auto-ignition, and the tradeoff between the deflagrative and auto-ignition combustion modes.

5.2 The Effect of Diluent Composition on HCCI Behavior

Up to this point, the experiments presented in this thesis have been conducted for stoichiometric EGR dilute fuel-air mixtures ($\phi = 1$). In the following sets of experiments, the fraction of external EGR was reduced in order to increase the fraction of molar O_2 within the diluent mixture, resulting in ϕ less than 1. As seen in Figures 5.2a and 5.2b, an increased fraction of EGR (while holding fuel mass, total dilution level, and intake conditions constant) causes the overall mixture specific heat c_p to increase, thus decreasing in-cylinder compression temperatures. In the case of pure HCCI auto-ignition, this decrease in T_u for a given crank angle causes the main combustion event to retard. It is seen that HCCI combustion retards rather significantly for a relatively small change (3.2% absolute) in the total EGR fraction (including internal and external EGR). If the compression temperatures for the HCCI cases in Figures 5.2a and 5.2b are purposely increased as the EGR fraction is increased, combustion phasing can be advanced to its original location. This effect is seen in Figure 5.3 in which a similar procedure to that of Dec et al. [11] was used to isolate the effects of O_2 concentration on HCCI burn rates by holding CA50 constant.

The HCCI experiments depicted in Figure 5.3 were performed at a constant engine speed (2000 rpm), dilution level ($\phi' \approx 0.4$), negative valve overlap (152° CA), and fueling rate (12.5 mg/cycle), corresponding to a load of ~4.5 bar $IMEP_g$. Combustion phasing was held constant at ~7° after TDC through the simultaneous increase of external EGR and intake temperature. Intake temperature was increased by ~75°C to counteract an 18% absolute increase in the total EGR fraction. With each incremental increase in intake temperature, a slight increase in both the intake and exhaust pressures was required to compensate for variations in incoming charge density. These pressure corrections allowed the total

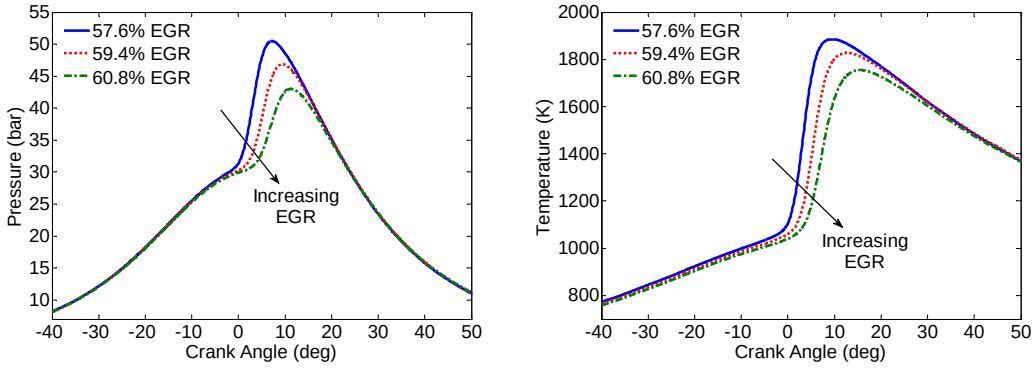

(a) Cylinder pressure (b) Cylinder mean temperature

Figure 5.2: Curves of (a) cylinder pressure and (b) mass-averaged cylinder temperature showcasing the effects of external EGR addition on HCCI combustion while holding all other variables constant (fueling rate = 12 mg/cycle, NVO = 170 CAD, intake temperature = 45°C, and intake/exhaust pressure = 1.0/1.05 bar) – legend indicates total in-cylinder EGR mass fraction, including internal and external EGR

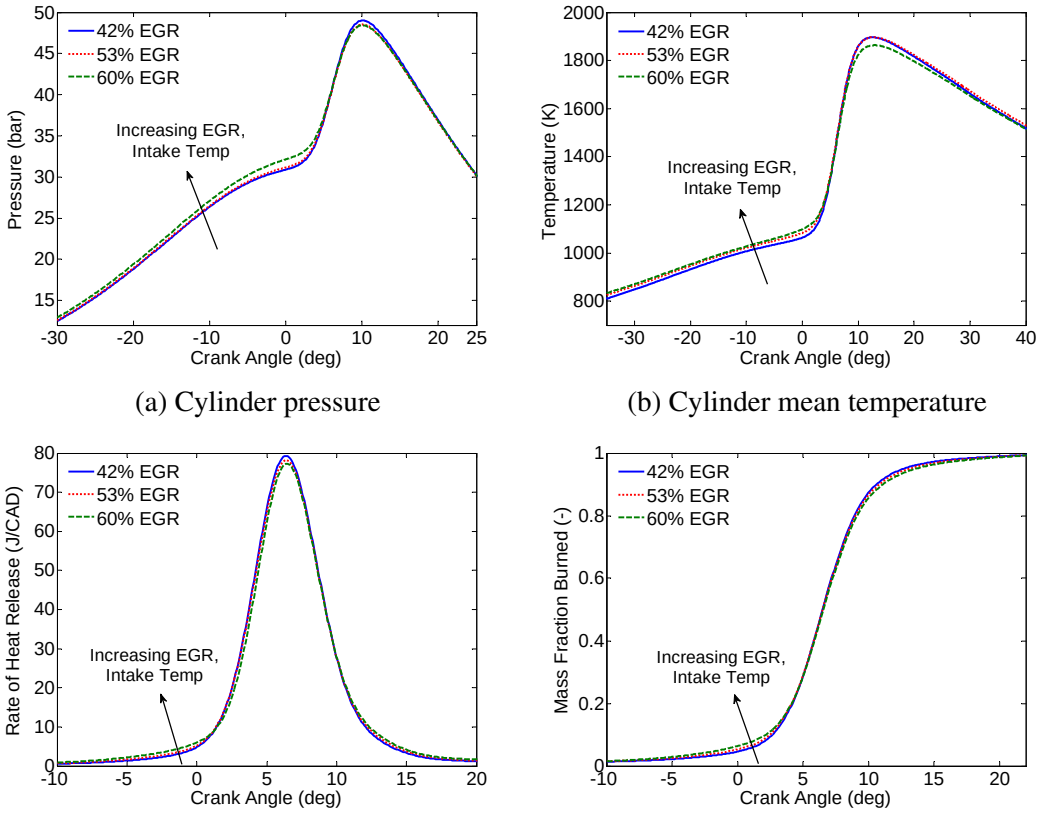

(a) Cylinder pressure (b) Cylinder mean temperature

(c) Rate of heat release (d) Mass fraction burned

Figure 5.3: Curves of (a) cylinder pressure, (b) mass-averaged cylinder temperature, (c) rate of heat release, and (d) mass fraction burned for HCCI combustion at constant CA50 and fueling rate and various reactant O_2 molar fractions

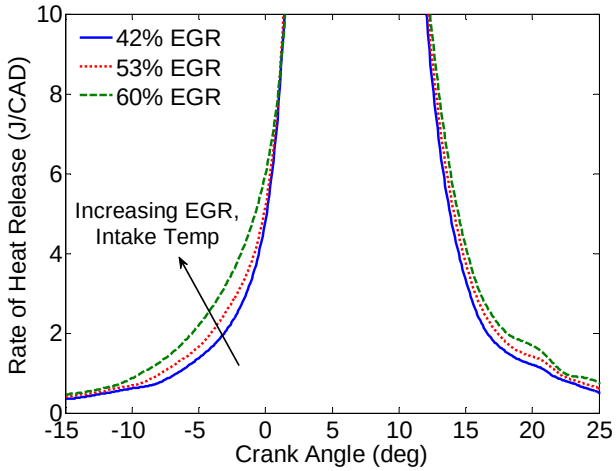

Figure 5.4: More detailed view of the rate of heat release curves for HCCI combustion at constant CA50 and fueling rate and various O_2 molar fractions

charge dilution level to remain constant and the desired EGR flow rates to be obtained. As EGR increased, the estimated molar fraction of O_2 in the reactants (assuming the residual gases were composed of products of complete combustion) decreased by 5.7% absolute. The operating conditions for the HCCI cases plotted in Figure 5.3 are listed in Table 5.1.

In Figure 5.3, it is seen that this experiment yielded similar results to that of Dec et al. [11]. As the total EGR fraction increased, HCCI 10-90% burn durations increased by $\sim$1.5° CA (19% relative), seen in Figure 5.3d, peak rates of heat release decreased by 2.5% (seen in Figure 5.3c), and peak rates of pressure rise decreased by $\sim$8%, seen in Figure 5.3a. Peak rates of temperature rise also decreased for the most EGR dilute case despite the necessary increase in compression temperature, seen in Figure 5.3b. A more detailed view of the rate of heat release curves is given in Figure 5.4. These changes in overall combustion behavior are small despite a 40% relative decrease in molar O_2 fraction. These results indicate that major changes in diluent composition have a small effect on overall HCCI burn rates provided CA50 is held constant by means of compression temperature compensation.

Parameter	*Case 1*	*Case 2*	*Case 3*
Engine speed (rpm)	2000	2000	2000
Fuel flow rate (mg/cycle)	12.5	12.5	12.5
Fuel pressure (bar)	∼100	∼100	∼100
Fuel-to-air equivalence ratio, ϕ	0.66	0.82	0.96
Fuel-to-charge equivalence ratio, ϕ'	0.38	0.39	0.39
Total EGR mass fraction, in-cylinder (%)	42	53	60
Molar O_2 fraction in reactants (%)	15.2	12.1	9.5
Intake pressure (bar)	1.0	1.04	1.1
Exhaust pressure (bar)	1.05	1.06	1.13
Intake temperature (°C)	45	83	121
Negative valve overlap (° CA)	152	152	152
Intake valve closing (° bTDC)	150	150	150
Exhaust valve opening (° aTDC)	150	150	150
Valve lift (mm)	6.0	6.0	6.0
Coolant temperature (°C)	90	90	90
Oil temperature (°C)	90	90	90
Start of fuel injection (° bTDC)	330	330	330
External EGR, measured in intake manifold (%)	0	21	32
EGR coolant temperature (°C)	55	55	55
Ringing intensity (MW/m^2)	4.34	3.59	3.19

Table 5.1: Experimental conditions during the HCCI O_2 sweep

5.3 Procedure to Study the Effects of Diluent Composition on SACI Behavior

As shown previously, an increased fraction of EGR at a given dilution level, intake pressure, and intake temperature causes in-cylinder compression temperatures (i.e. T_u) to decrease, thus phasing the onset of HCCI ignition later in the cycle. In Figure 3.13, it was shown that for a given composition and spark advance, a similar decrease in T_u also has a dramatic impact on SACI combustion, causing initial heat release rates to slow and auto-ignition delay times to increase, resulting in more retarded and unstable SACI combustion. It is, therefore, expected that the addition of EGR (while holding all other variables constant) will have a similar retarding effect on SACI combustion as it does with HCCI.

For this study, a similar procedure to that discussed in the previous section was fol-

lowed in order to isolate the effects of charge O_2-to-fuel ratio on SACI burn rates. SACI experiments were performed at a constant fueling rate of 17.5 mg/cycle, corresponding to a load of $\sim$6 bar $IMEP_g$, well above the high load limit of HCCI. At this load condition, a substantial portion of the charge must be consumed by flame propagation in order to comply with cylinder pressure rise rate/ringing intensity limitations. Combustion phasing was also held constant at $\sim$10° after TDC to provide near maximum thermal efficiency for this spark-ignited combustion mode [65]. Mixture composition was adjusted by carefully modulating the level of external EGR. The engine operating conditions for this study are given in Table 5.2.

Parameter	*Value*
Engine speed (rpm)	2000
Fuel flow rate (mg/cycle)	17.5
Fuel pressure (bar)	$\sim$100
Intake pressure (bar)	1.01-1.12
Exhaust pressure (bar)	1.07-1.24
Intake temperature (°C)	55-130
Negative valve overlap (° CA)	100
Intake valve closing (° bTDC)	150
Exhaust valve opening (° aTDC)	150
Valve lift (mm)	6.0
Coolant temperature (°C)	90
Oil temperature (°C)	90
Spark advance (° bTDC)	32
Spark energy from the coil (mJ)	70
Start of fuel injection (° bTDC)	330
External EGR, measured in intake manifold (%)	7.0-28.5
EGR coolant temperature (°C)	55

Table 5.2: Experimental conditions during the SACI O_2 sweep

For a well controlled experiment, the fewest number of variables were adjusted to counteract the retarding effects of increased EGR and maintain constant phasing. As in the previous HCCI experiment, it was found that an increase in intake charge temperature at higher levels of EGR dilution was necessary to increase T_{IVC} so that phasing could be

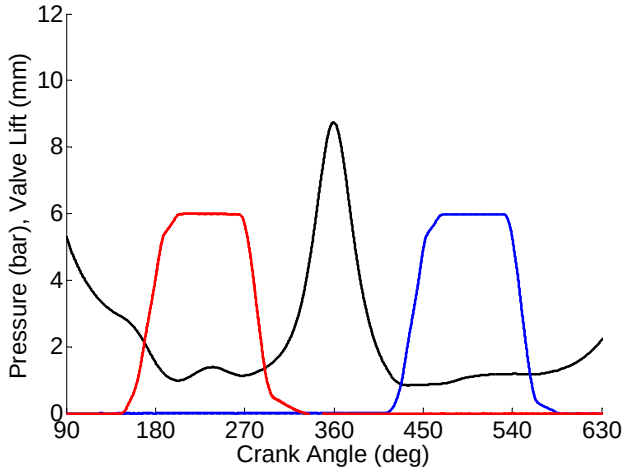

Figure 5.5: Initial valve timings and recompression pressure with 100° CA of negative valve overlap, set to achieve SACI combustion phasing at 10° after TDC

maintained while operating at a constant spark advance of 32° before TDC. This increase in T_{IVC} could have also been achieved through the adjustment of NVO; however, NVO was held constant at 100° CA, as seen in Figure 5.5, so that potential changes in thermal and compositional stratification associated with varying valve events could be minimized. The hot residual gases retained from NVO, in addition to direct intake charge heating, provided the necessary thermal energy to promote end-gas auto-ignition.

Parameter	*Case 1*	*Case 2*	*Case 3*	*Case 4*
Fueling rate (mg/cycle)	17.5	17.5	17.5	17.5
Fuel-to-air equivalence ratio, ϕ	0.71	0.81	0.92	0.99
Fuel-to-O_2 equivalence ratio, φ	0.64	0.73	0.86	0.98
Fuel-to-charge equivalence ratio, ϕ'	0.52	0.51	0.52	0.53
Internal EGR mass fraction, in-cylinder (%)	22.5	24.6	24.8	25.9
External EGR mass fraction, in-cylinder (%)	5.2	12.5	17.9	20.1
Total EGR mass fraction, in-cylinder (%)	27.7	37.1	42.7	46.0
Molar O_2 fraction in reactants (%)	16.6	14.5	12.6	11.5
Molar fraction of stoichiometric combustion products in reactants, X_{SCP} (%)	19.9	30.0	38.8	44.0
Intake temperature (°C)	55	70	100	130
Intake pressure (bar)	1.01	1.05	1.09	1.12
Exhaust pressure (bar)	1.07	1.17	1.20	1.24

Table 5.3: SACI conditions with varying EGR/air dilution rates at constant CA50 (10° after TDC)

The initial SACI condition (Case 1), for which the least amount of external EGR was implemented, corresponds to the first column of Table 5.3. At this condition, the 'fuel-to-air' equivalence ratio was measured to be $\phi = 0.71$ and the calculated 'fuel-to-O_2' equivalence ratio (as described in Eq. 2.22) was $\varphi = 0.64$. The total dilution rate was $\sim$52% by mass, with about $\sim$28% from EGR (including internal and external) and the remaining percentage from excess air. The engine was operated unthrottled at this condition, with about 7 kPa exhaust backpressure. In addition, the molar O_2 fraction in the reactants was estimated to be 16.6% by assuming that the EGR was composed of products of complete combustion (CO_2, H_2O, O_2, and N_2) at the measured 'fuel-to-air' equivalence ratio, ϕ. Similarly, the case with the highest level of EGR dilution (Case 4 in Table 5.3), has an almost stoichiometric 'fuel-to-air' equivalence ratio ($\phi = 0.99$) and an estimated reactant O_2 molar fraction of 11.5%. In the following figures, the various SACI cases in Table 5.3 will be identified in terms of their reactant molar O_2 fraction.

After recording SACI Case 1, for which very little external EGR was implemented, the in-cylinder reactant O_2 molar fraction was then purposely decreased by introducing a larger percentage of external EGR into the intake charge, thereby increasing the total EGR mass fraction in-cylinder, as seen in Figure 5.6a. This was done while attempting to hold total ϕ' constant at $\sim$0.5, seen in Figure 5.6b. When adding EGR, a portion of the incoming air was replaced with stoichiometric products of combustion, causing both the 'fuel-to-air' equivalence ratio ϕ and the 'fuel-to-O_2' equivalence ratio φ to increase, as seen in Figure 5.6b. As a result, the in-cylinder molar fraction of stoichiometric combustion products X_{SCP} (as described in Eq. 2.24) also increased, seen in Figure 5.6c.

In Figure 5.6a, it is seen that the variation in O_2 fraction does not correlate linearly with the total EGR fraction since the EGR contains a small percentage of O_2 for mixtures with 'fuel-to-air' equivalence ratios less than one. As the EGR fraction increases, the molar O_2 fraction decreases at a slightly faster rate as the molar molar O_2 is replaced with stoichiometric combustion products. Figure 5.6c shows a linear increase in X_{SCP} as the O_2

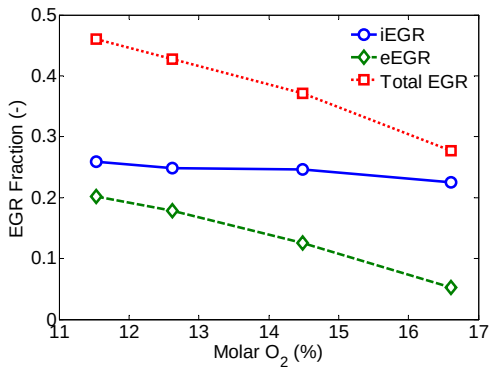

(a) EGR mass fractions

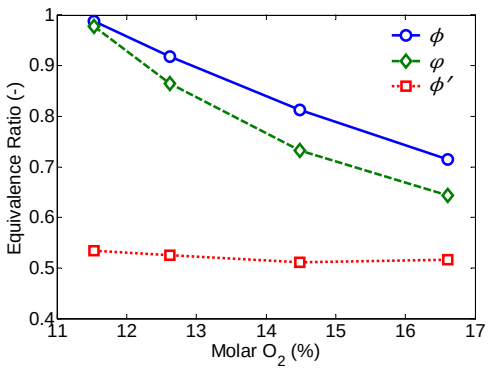

(b) Equivalence ratios

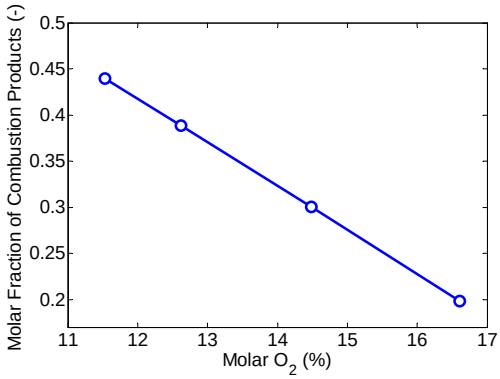

(c) Fraction of combustion products

Figure 5.6: (a) Variation in internal, external, and total EGR mass fractions, (b) variation in 'fuel-to-air' equivalence ratio ϕ, 'fuel-to-O_2' equivalence ratio φ, and 'fuel-to-charge' equivalence ratio ϕ', and (c) variation in the molar fraction of stoichiometric combustion products (X_{SCP}) for the SACI O_2 sweep cases listed in Table 5.3

fraction decreases since X_{SCP} combines linearly with the molar O_2 fraction (X_{O_2}) in Eq. 2.25 to account for the total in-cylinder mass which is held relatively constant. A similar linear increase in the 'fuel-to-air' equivalence ratio, ϕ, is seen since ϕ accounts for all in-cylinder atomic species in both the incoming mass and the residual mass, as described by Babajimopoulos et al. [98]. The 'fuel-to-O_2' equivalence ratio φ only accounts for the reactive atoms (fuel and O_2) in both the incoming and residual masses, hence this value decreases relative to ϕ for lean mixtures operating with EGR dilution.

As the mass fraction of EGR increases, combustion would tend to retard if T_{IVC} were held constant due to an increase in mixture heat capacity which in turn would produce lower TDC temperatures. As with the HCCI experiments, in order to maintain CA50 at

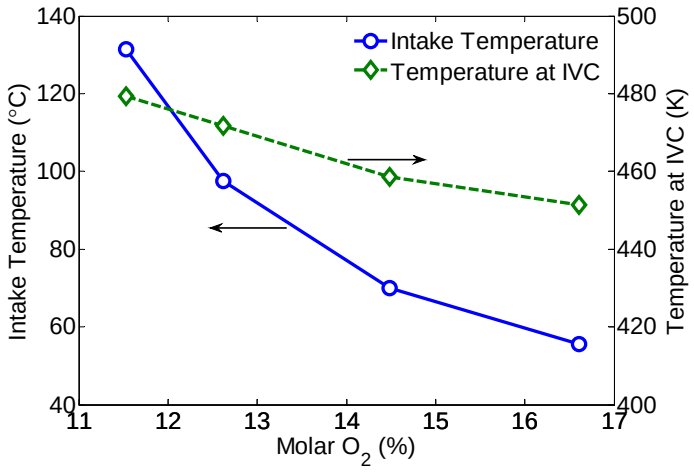

Figure 5.7: Variation in intake temperature and temperature at IVC for the SACI O_2 sweep cases listed in Table 5.3

$\sim$10° after TDC, the incoming charge temperature (including air and eEGR) must also increase, as seen in Figure 5.7. The intake temperature increases by $\sim$75°C between the cases with the lowest and highest EGR fractions, corresponding to a $\sim$30 K increase in temperature at IVC.

The increase in intake temperature with EGR fraction acts to decrease the density of the incoming charge, thus decreasing the inducted charge mass for constant valve timings. In order to compensate for this decrease and maintain the estimated dilution level ϕ', the intake pressure was elevated slightly for each incremental increase in temperature, as seen in Table 5.3. As intake pressure increased, the exhaust back pressure was also increased to maintain the necessary flow of external EGR. The increased exhaust pressure caused a $\sim$3.4% absolute increase in the internal EGR fraction, as seen in Figure 5.6a. Fueling rate was held constant throughout this procedure since fuel was injected directly into the cylinder. Fuel injection occurred early in the intake stroke (330° before TDC), allowing the fuel more time to mix with the incoming charge. Since the intake and exhaust pressures directly affect the masses of incoming air, external EGR, and internal EGR in different ways, simultaneous control of total mass, equivalence ratio, and phasing was quite challenging and as a result, subtle variations in ϕ' were difficult to avoid. However, the maximum difference

in ϕ' between cases (4% relative) is small and is not expected to have a large effect on the overall combustion behavior.

5.4 Experiments with Varying Reactant O_2 Fraction and T_u at Constant Spark Timing and Combustion Phasing

5.4.1 The Effect of Diluent Composition on Overall SACI Burn Rates

From previous experiments presented in this document, it is apparent that unburned temperature T_u has a dramatic effect on the phasing and burn rates of SACI combustion since it affects the initial rates of flame propagation and is the primary factor determining the onset of bulk auto-ignition heat release [63, 115]. In this experiment, the effects of temperature are used to counteract the effects of diluent composition in order to maintain phasing at $\sim$10° after TDC. Figures 5.8a and 5.8b show the cylinder pressure and mass-averaged temperature curves, respectively, for the four SACI cases listed in Table 5.3. The timing of spark ignition is constant for every case, yet it is clear that the shape of the curves and the overall combustion behavior differs substantially.

Taking a closer look at the temperature curves in Figure 5.9, it becomes clear that the case with the highest level of EGR dilution has consistently higher temperatures prior to spark ignition than the case with the lowest level of EGR dilution. At the time of spark ignition, the maximum temperature difference between the cases is $\sim$30 K. This increase in the compression temperature (i.e. T_u, T_{IVC}) is primarily a result of the increase in intake temperature that was necessary to maintain a constant phasing. Considering the higher T_u's, it is understood that the increase in intake temperature more than compensates for the increased mixture c_p with EGR. This same behavior is seen in Figures 5.1b and 5.3b for HCCI combustion. Following the spark, the most EGR dilute case appears to be the least affected by deflagrative heat release, despite having the highest unburned temperature which has been shown to increase rates of flame propagation [116]. This case also

exhibits the highest rates of pressure and temperature rise, resulting in more 'HCCI-like' combustion behavior.

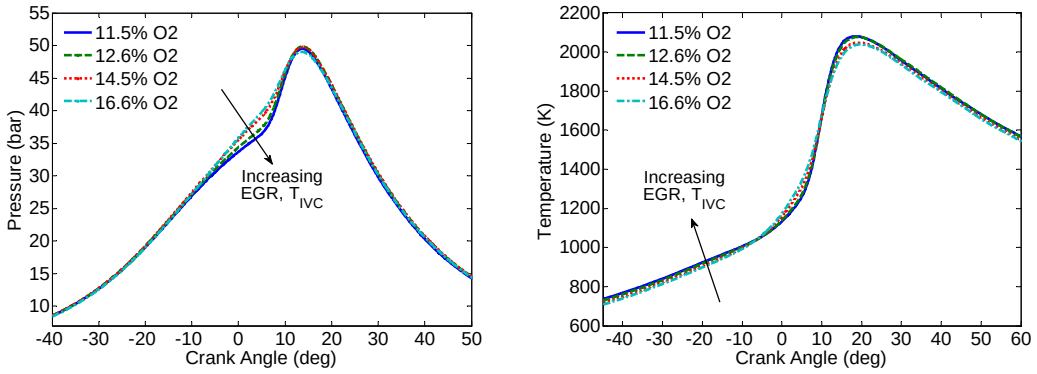

(a) Cylinder pressure (b) Cylinder mean temperature

Figure 5.8: Curves of (a) cylinder pressure and (b) mass-averaged cylinder temperature for the SACI O_2 sweep conditions listed in Table 5.3, with CA50 set to 10° after TDC

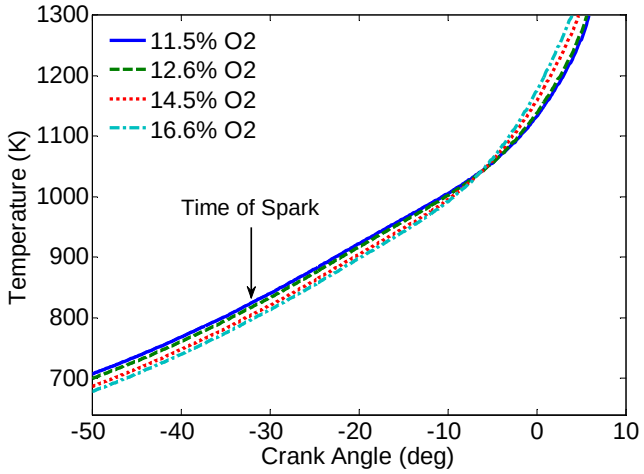

Figure 5.9: Closer view of the mass-averaged cylinder temperature curves at the timing of spark ignition

Further insight is gained from examining the rate of heat release and mass fraction burned (MFB) curves in Figures 5.10a and 5.10b. From these curves, it is seen that overall SACI burn rates can be manipulated at a constant spark timing and CA50 through the careful adjustment of T_u and reactant O_2 molar fraction. As inferred from the pressure and temperature curves in Figures 5.8a and 5.8b, the case with the lowest T_u and highest

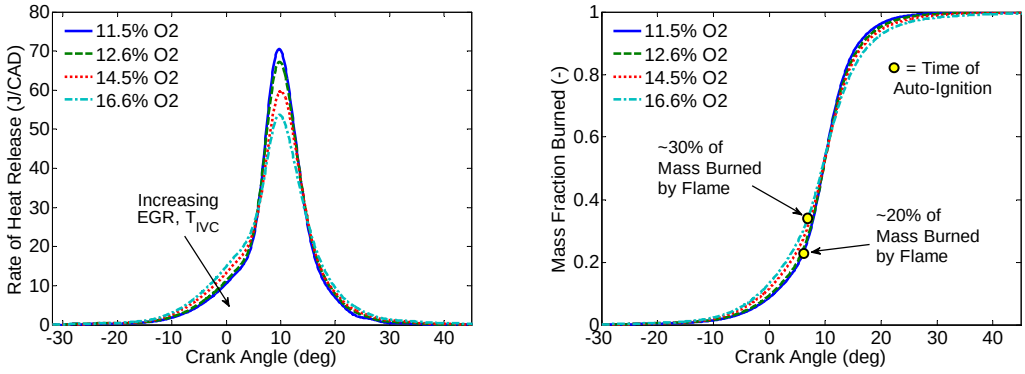

(a) Rate of heat release

(b) Mass fraction burned

Figure 5.10: Curves of (a) rate of heat release and (b) mass fraction burned for the SACI O_2 sweep conditions described in Table 5.3

O_2 fraction has the fastest initial rates of heat release, thought to be associated with flame propagation. The peak rate of heat release for this condition (16.6% molar O_2) is also $\sim$24% lower than the peak rate of heat release for the case with the lowest O_2 fraction (11.5% molar O_2). This finding is contrary to the HCCI results discussed previously [11], in which peak heat release rates were shown to *increase* for a higher O_2 fraction. This opposite behavior likely stems from the relationship between deflagration and auto-ignition, which is discussed below.

The transition from flame propagation to auto-ignition is located in the same manner as in Chapter 4 (and described in Chapter 2), by locating the inflection point in the rate of heat release. At the onset of auto-ignition, it is assumed that a bimodal transition between flame propagation and thermal runaway takes place; SACI combustion modeling with KIVA-3V indicates that this is a reasonable assumption [90, 117]. By estimating the location of auto-ignition, the fraction of mass consumed by flame can be estimated using the mass fraction burned curves in Figure 5.10b. The condition with the highest fraction of O_2 (and lowest T_u) has the highest fraction of flame based heat release, with an average of $\sim$30% of the mass consumed by the flame. On the other hand, for the condition with the lowest O_2 fraction (and highest T_u) $\sim$20% of the mass is consumed by the flame. Since less fuel mass is consumed via deflagration, a larger percentage of the total fuel energy is released during

bulk auto-ignition and a higher peak rate of heat release is seen. This case also has a higher propensity to auto-ignite due to its higher T_u at the time of spark and, therefore, the flame does not need to propagate as far to compress the end-gas to the point of auto-ignition. For this case, a lower percentage of flame propagation heat release is sufficient to promote auto-ignition. Figure 5.11 depicts the inverse relationship between the fraction of flame heat release and the peak rate of heat release, as was observed in Chapter 4. This increased T_u, therefore, contributes to the more 'HCCI-like' behavior of this condition.

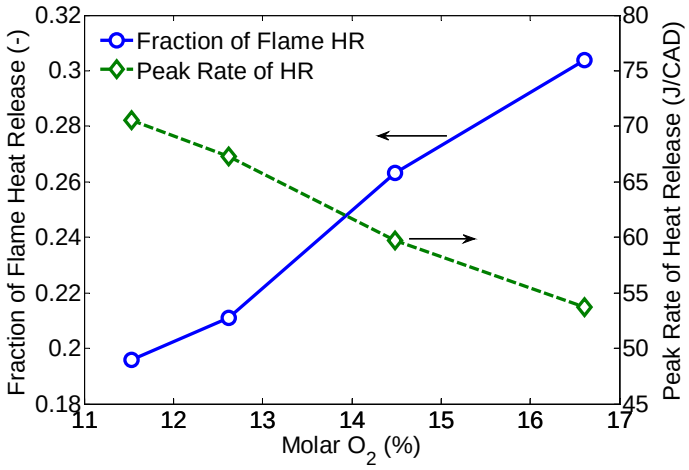

Figure 5.11: Fraction of flame heat release and peak rate of heat release vs. molar O_2 fraction for the SACI O_2 sweep

As in Chapter 4, a two-zone heat release analysis was used to estimate the temperature of the unburned gas at the time of auto-ignition. The results, plotted in Figure 5.12, show that for each case, the end-gases auto-ignite at approximately the same temperature ($\sim$1050 K) and differ by no more than 0.7%. This observation suggests that the location of auto-ignition depends on compression heating from the expanding flame front since the case with the lowest T_u at the time of spark also exhibits the largest fraction of flame based heat release. However, in assuming an instantaneous transition between flame propagation and auto-ignition, it is also possible that the temperatures at auto-ignition are slightly under predicted by the two-zone model, as the analysis cannot account for low temperature heat

release in the end-gas prior to thermal runaway.

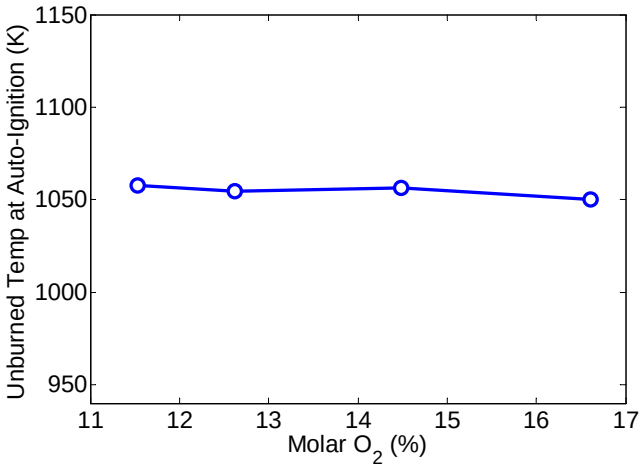

Figure 5.12: Unburned gas temperature (T_u) at the estimated time of auto-ignition for each case of the SACI O_2 sweep

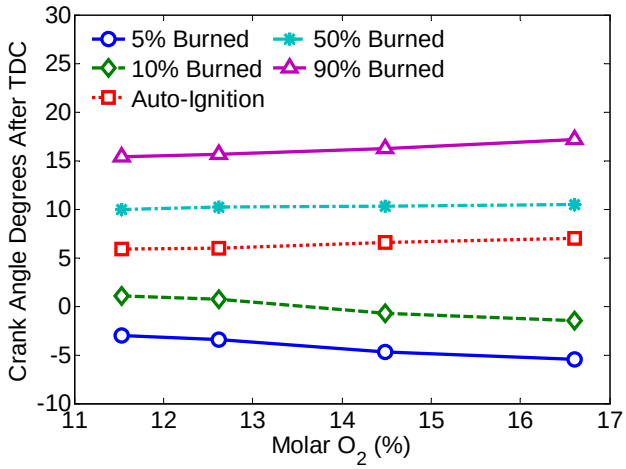

Figure 5.13: Crank angle locations at the time of 5% mass fraction burned, 10% burned, auto-ignition, 50% burned, and 90% burned for each case of the SACI O_2 sweep

From inspection of the rate of heat release curves in Figure 5.10a, the main auto-ignition event appears to occur at approximately the same time for each case. This behavior is confirmed in Figure 5.13, in which the locations of 5% mass fraction burned, 10% burned, auto-ignition, 50% burned, and 90% burned are plotted for every case. The location of 50% burned is constant for every case in accordance with the control strategy and the timing of

the bulk auto-ignition event is shown to occur (on average) at approximately the same location within the cycle using the metric previously described. The maximum difference in the estimated onset of auto-ignition between the cases is $\sim$1.1° CA.

Although auto-ignition/thermal runaway is estimated to begin at about the same time for every SACI case, the rates of bulk heat release, seen in Figure 5.10a appear to decrease for a more O_2 dilute mixture. This is rather interesting, as it was previously shown (in Figures 5.1a and 5.3c) that the rates of HCCI auto-ignition *increase* slightly for a higher O_2 fraction. This contradictory behavior is perhaps due to variations in the thermal characteristics of the end-gas resulting from a large fraction of flame based heat release. As the portion of deflagrative heat release increases (for lower T_u mixtures), more of the hot core charge is consumed by the flame. The mass consumed by auto-ignition decreases, and this mass resides closer to the cylinder wall and potentially contains a larger relative fraction of low temperature zones. For these cases, more compression heating (either by flame propagation or expanding pockets of auto-igniting gas) could be necessary to promote complete combustion, thus lengthening overall bulk heat release rates and perhaps delaying the calculated auto-ignition transition point. For lower rates of auto-ignition, the end-gases are cooled further by high rates of piston expansion and become even less inclined to burn. This theory is supported by the increase in the 50-90% burn durations (and hence, 0-90% burn durations) for increased fractions of O_2 and flame based heat release, as seen in Figure 5.13. Sjöberg et al. saw similar burn lengthening effects in HCCI combustion due to an increased thermal gradient resulting from cooler wall temperatures [30].

Based on the fact that the spark timing and 0-50% burn durations are held constant, the initial rates of auto-ignition must also differ between each case. Prior to the onset of auto-ignition, a smaller mass fraction is consumed by flame propagation for the case with the lowest O_2 fraction (highest T_u). Thus, in order for the 50% MFB location to remain constant, the heat release rates following the initial deflagration must increase relative to the highest O_2 case in order to give the lagging mass burned fraction an opportunity to

catch up. Optical SACI experiments by Zigler et al. [46] showed that local ignition sites in the initial stages of auto-ignition appeared with increasing frequency for a higher T_u.

Based on the results in Figures 5.10a and 5.13, it appears that the increased fraction of flame based heat release and the resulting differences in end-gas thermal stratification outweigh the expected compositional effects on the rates of auto-ignition as suggested by Dec et al. [11] and shown in Section 5.2 (due to changes in mixture c_p and/or O_2 fraction). To better quantify and understand the effects of mixture composition on the timing and burn rates of auto-ignition under SACI conditions, more robust methods of ignition detection and local mixture analysis will be needed.

5.4.2 The Effects of Composition on the Rates of SACI Flame Propagation

The SACI cases described in Table 5.3 have approximately the same crank angle duration between the onset of spark ignition and the onset of auto-ignition. Since the case with the highest O_2 fraction also has the lowest T_u, more compression heating from the flame is necessary to promote auto-ignition within approximately the same crank angle interval. Therefore, the initial flame propagation rates must be faster for this case, which is confirmed in the 0-5% and 0-10% burn durations plotted in Figure 5.13. Since spark advance, valve timings, and engine speed remain constant between each case, the nominal flow conditions during the early stages of flame propagation are expected to be similar [92] and yet, the fastest flames exist despite a decreased T_u. In order to gain more insight into the dominant flame mechanisms at play, it is necessary to investigate the effects of mixture composition on flame temperature and chemical reaction rates, and their resulting impact on laminar flame speeds.

As in Chapter 4, the recently developed laminar flame speed correlation by Middleton et al. [89] was used to investigate the dominant mechanisms affecting laminar flame speed during the initial stages of combustion. As mentioned in Chapter 2, this correlation

was developed using thermal, transport, and kinetic simulations and was validated against available laminar flame speed data at high temperature and high pressure conditions relevant to engine operation [95, 99, 100]. The correlation was developed from simulations which were performed to assess the chemical kinetic influence of O_2 concentration on S_L. Additional simulations were performed where the molar concentration of each reaction with O_2 was scaled up or down in the kinetics to maintain constant O_2 concentration for varying levels of dilution method at a given ϕ' [89]. To decouple chemistry from transport and thermal effects, the O_2 concentration was not perturbed outside of the chemistry. The reactions that showed the strongest sensitivity to changes in O_2 concentration included the high temperature chain branching reaction (O_2 + H $\leftrightarrow$ OH + O) and the competing chain terminating reaction (O_2 + H (+m) $\leftrightarrow$ HO_2 (+m)), where m is a third body. Both of these reactions are most active in the high temperature region of the reaction front. These results are consistent with other studies identifying the importance of these reactions to flame speed and ignition delay [118–120] and indicate that the sensitivity of S_L to dilution method is in part a kinetic effect related to the mixture O_2 concentration.

The S_L correlation relies on the unburned gas temperature, cylinder pressure, and composition of the mixture at the point of interest, which was selected to be 15° after (spark) ignition timing (AIT). As in Chapter 4, this timing was selected based upon an optical engine study of conventional SI combustion by Aleiferis et al. [73] in which the experimentally observed flame growth rate at 15° AIT showed good agreement with calculated S_L, indicating that the flame was not highly wrinkled, and was strongly correlated to the 0-5% mass fraction burned interval. An additional optical study by Aleiferis et al. [92] involving SI combustion for multiple fuels showed that, in general, the trends in flame radii growth early on in the cycle, i.e. for MFB $<$ 5-10% were similar to the trends in the MFB interval obtained from in-cylinder pressure measurements for MFB $>$ 5-10%. This finding shows that trends in early flame growth rates are reflected in the early MFB, and this is expected to be true particularly for cases at constant spark timing and engine speed, in which

the variations in turbulent flow conditions are expected to be minor.

To better understand the relationship between the initial flame heat release period and the mass fraction burned, the burned gas temperature (T_b) and laminar flame speed (S_L) were estimated at 15° AIT using the correlation by Middleton et al. [89]. As seen in Figure 5.14a, the unburned gas temperature (T_u) at 15° AIT decreases by ∼30 K (3%) as the mixture O_2 fraction increases; however, the predicted T_b shows the opposite trend, increasing by ∼110 K (5.5%). This behavior is likely due to the decrease in mixture heat capacity c_p with a higher O_2 fraction (as seen in Figure 5.14b at 40° before TDC) resulting in a greater increase in burned gas temperature despite a lower T_u. It is therefore unclear if the results are more sensitive to the increased O_2 fraction or the increased T_b that accompanies it. It should be noted that it is unlikely that pressure is affecting the flame behavior, as for all cases, the cylinder pressures at 15° AIT were essentially constant at ∼21.5 bar, differing by no more than ± 0.2 bar (0.9%). The corresponding estimations in laminar flame speed follow a similar trend to T_b, increasing in the direction of greater O_2 fraction, as seen in Figure 5.15a. This increase in S_L is accompanied by an 8.6% decrease in the 0-5% mass fraction burned duration, seen in Figure 5.15b. The decrease in 0-5% burn duration appears to be due largely to the effect of S_L on initial flame growth, as spark advance is held constant and nominal flow conditions are expected to be similar [92].

In Figure 5.16a the measured T_u and O_2 fraction and the estimated T_b and S_L at 15° AIT are normalized with respect to the case with the highest O_2 fraction (i.e. Case 1 in Table 5.3). According to the correlation, the change in estimated S_L follows the change in O_2 fraction more closely than the changes in T_u and T_b; however, it is possible that this behavior is also the result of an extreme sensitivity of S_L to T_b. Further investigation into the effects of temperature and composition on S_L was conducted with the S_L correlation. Predictions of S_L were made in which T_u was held constant (at the measured value for Case 1 in Table 5.3) and T_b was held constant at 2000 K. To maintain T_b as the mixture became progressively more EGR dilute (and the mixture c_p increased), the EGR rate was decreased

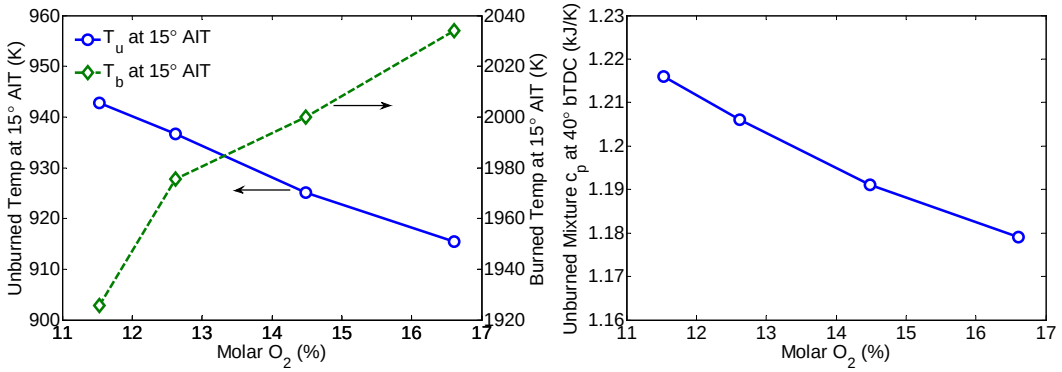

(a) T_u and T_b at 15° AIT (b) Heat capacity c_p at 40° before TDC

Figure 5.14: (a) Variation in measured T_u and estimated T_b at 15° after (spark) ignition timing (AIT) using the correlation of Middleton et al. [89]; (b) the decrease in unburned mixture c_p with increased in-cylinder O_2 fraction likely contributes to the increase in T_b despite the decrease in T_u

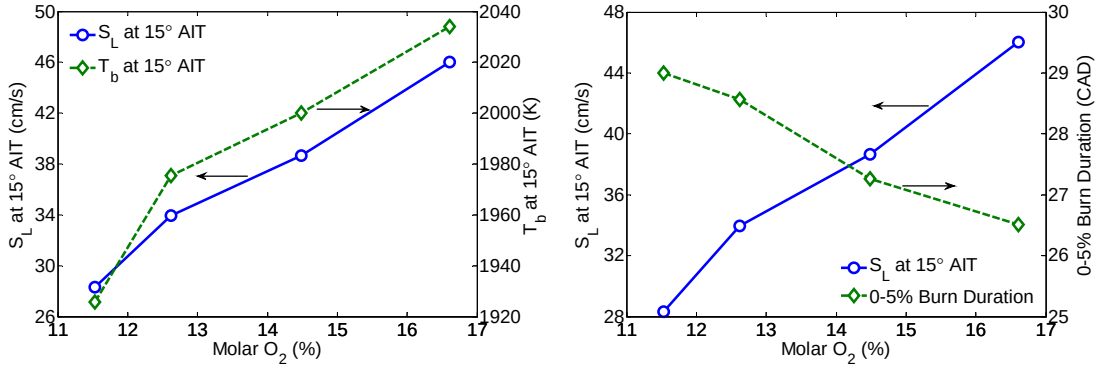

(a) T_b and S_L at 15° AIT (b) S_L and 0-5% burn duration

Figure 5.15: Correlations of (a) burned gas temperature (T_b) and (b) 0-5% burn duration with estimated S_L from the correlation of Middleton et al. [89] at 15° after spark ignition timing

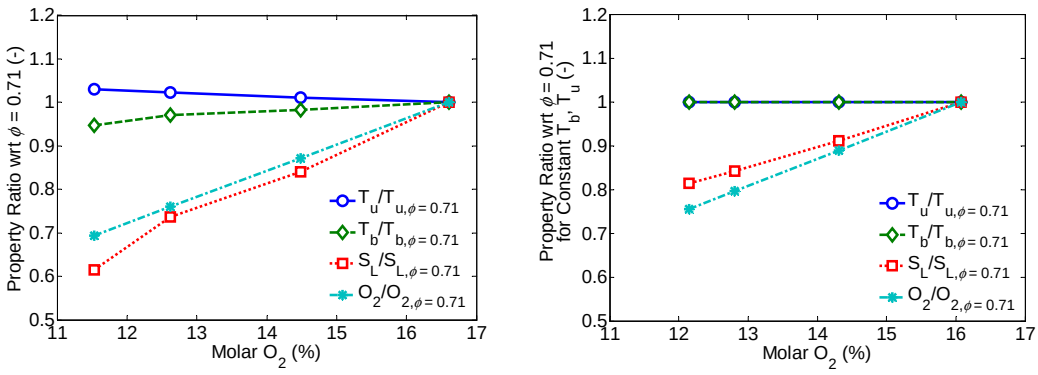

(a) T_b and S_L at 15° AIT

(b) S_L and 0-5% burn duration

Figure 5.16: (a) Normalized curves of T_u, T_b, S_L, and O_2 fraction at 15° AIT with respect to SACI Case 1 from Table 5.3; (b) normalized curves of T_u, T_b, S_L, and O_2 fraction assuming a constant T_u and constant T_b at 2000 K. The curves indicate the dependence of S_L on T_u, T_b, and O_2.

slightly for a given ϕ so that the overall fuel concentration of the mixture increased (ϕ' increased by 18%, from 0.5 for the most air dilute case to 0.59 for the most EGR dilute case). As seen in Figure 5.16b, these adjustments to the mixture composition led to a narrower range of estimated O_2 molar fraction in the reactants than that seen in Table 5.3. Despite the increased ϕ', the predicted S_L decreased by ~20% for a ~25% decrease in O_2 molar fraction. Based on the results in Figures 5.16a and 5.16b, S_L appears to be dependent on both temperature *and* O_2 fraction; however, more work is needed to experimentally isolate the O_2 effect from T_b, since this cannot be accomplished in an engine setting while maintaining dilution level and combustion phasing.

5.4.3 The Effects of Composition on SACI Combustion Limitations and Thermal Efficiency

In Figure 5.13, it is shown that overall SACI burn rates can be manipulated at a constant phasing and dilution level through the simultaneous manipulation of O_2 fraction and T_u. The ability to manage the burn rate and overall fraction of flame based heat release affects various combustion metrics, including ringing intensity, COV of $IMEP_n$, and NO_x

emissions. Variations in ringing intensity and COV of $IMEP_n$ are seen in Figure 5.17, plotted against the corresponding O_2 fraction for each case. As O_2 fraction increases (T_u decreases) and the flame propagates faster and further into the unburned mixture, peak rates of pressure rise and peak rates of heat release decrease and ringing intensity decreases by ~40%, from 2.7 MW/m^2 to 1.6 MW/m^2. In the HCCI experiment presented in Section 5.2, maximum rates of pressure rise decreased by ~8% (ringing intensity decreased by ~26%) through the *addition* of EGR. With the SACI study, for a similar change in O_2 molar fraction, maximum rates of pressure rise decreased by ~33% through a *reduction* in EGR rates. This result indicates the substantial effect of deflagrative heat release on the rates of auto-ignition, possibly through variations in the end-gas thermal distribution.

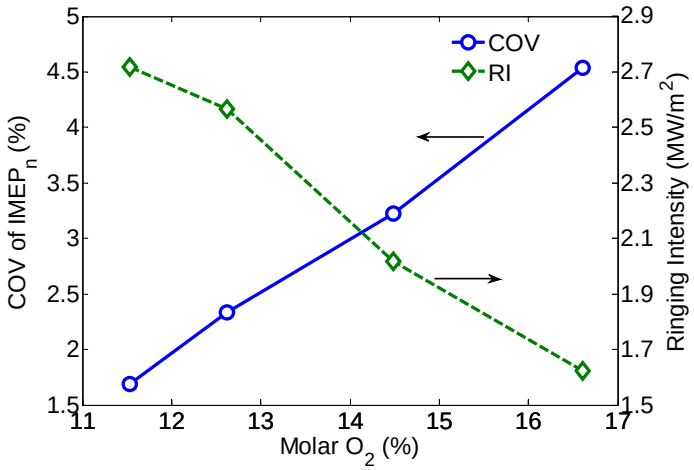

Figure 5.17: Variation in ringing intensity and COV of $IMEP_n$ for the SACI O_2 sweep

The decrease in ringing intensity is accompanied by a substantial increase in the COV of $IMEP_n$. For the most O_2 dilute case, with the lowest T_u and largest fraction of flame based heat release, the COV of $IMEP_n$ becomes borderline unstable at 4.5%. The sources of this instability are relatively unknown; however, as T_u decreases, the auto-ignition event relies more heavily on compression heating from the flame, so subtle variations in flame propagation could result in larger variations in the onset of auto-ignition. In addition, the onset of auto-ignition could become more affected by thermal stratification effects in the

end-gas, slowing the rates of bulk heat release and leading to more incomplete combustion and instability. The auto-ignition process is likely the dominant contributor to the unstable behavior as the case with the highest COV of $IMEP_n$ also has the fastest rates of flame propagation following the spark event.

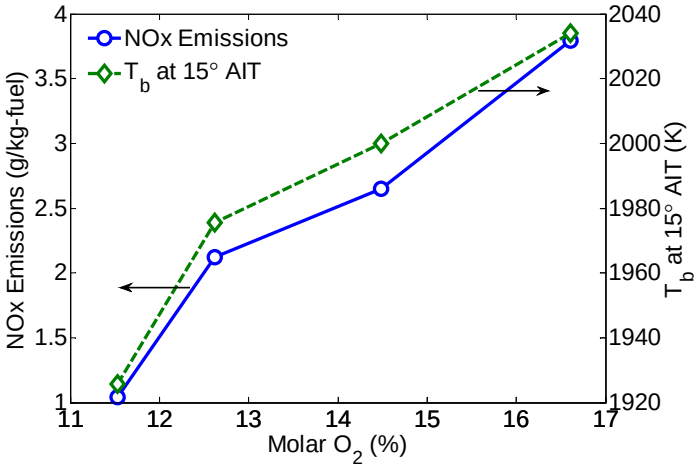

Figure 5.18: Variation in the early T_b and NO_x emissions for the SACI O_2 sweep

As seen in Figure 5.8b, peak mass-averaged cylinder temperatures appear to decrease with a higher O_2 fraction; however, NO_x emissions monotonically increase, seen in Figure 5.18. Between the lowest and highest levels of O_2 dilution, NO_x emissions increase four-fold and closely follow the trend in burned gas temperature shortly after spark ignition. The elevated T_b's early in the combustion process could be contributing to the increased levels of NO_x for more O_2 dilute mixtures. The higher fraction of O_2 itself could also contribute by increasing the chemical reaction rates that lead to NO_x formation [121].

As seen in Figure 5.19a, variations in mixture composition and combustion behavior at constant phasing allow for a 4% relative increase in thermal efficiency as the O_2 fraction increases. For a higher O_2 fraction, the net thermal efficiency increases by 1.6% absolute and the gross thermal efficiency increases by 1.3% absolute. The gross thermal efficiency is seen to decrease slightly for the highest O_2 case possibly due to unstable operating conditions. However, the net thermal efficiency continues to increase for this case due to

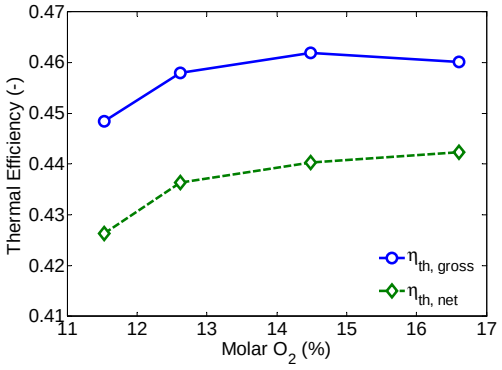

(a) $\eta_{th,gross}$ and $\eta_{th,net}$

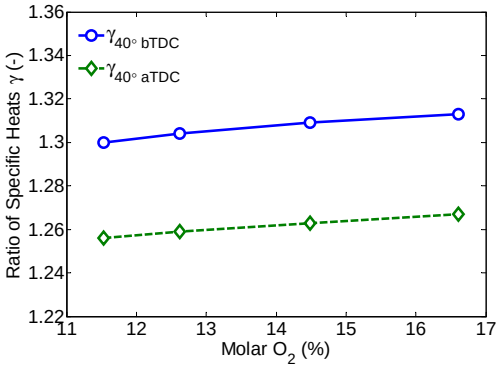

(b) γ at 40° before and 40° after TDC

Figure 5.19: (a) Variation in gross and net indicated thermal efficiency and (b) variation in mixture γ at 40° before TDC and 40° after TDC for the SACI O_2 sweep

decreased pumping losses as a result of lower exhaust back pressures, as seen in Table 5.3. Within a stable operating range, the gross thermal efficiency increases with O_2 fraction despite an increase in burn duration. This increase in efficiency could be due to lower heat losses to the cylinder wall as a result of lower peak mean cylinder temperatures, seen in Figure 5.8b. Additionally, the increased O_2 fraction (along with potentially lower temperatures) leads to differences in mixture properties, including the ratio of specific heats (γ). Figure 5.19b shows the increase in γ at 40° before TDC and 40° after TDC for an increased O_2 fraction. While SACI operation with elevated O_2 dilution appears favorable in light of the improved thermal efficiency, the increased engine instability and NO_x emissions may not be worth the relatively small gains in performance.

5.5 Summary and Conclusions

Independent control of SACI burn duration and combustion phasing was demonstrated by varying the charge oxygen-to-fuel ratio and unburned gas temperature T_u at a constant spark advance. In this interval, flame propagation consumed a substantial portion (20-30%) of the charge. As mixture O_2 fraction increased and T_u decreased, a larger fraction of flame based heat release and slightly longer 0-90% burn durations were seen for a constant

CA50. To maintain phasing, a ∼30 K increase (∼6%) in cylinder temperature at IVC was used to counteract a ∼30% decrease in molar O_2 fraction, indicating a high sensitivity to temperature.

It was shown that a ∼10% absolute change in the fraction of flame based heat release drastically affected the overall heat release behavior, rates of pressure rise, ringing intensity, and combustion stability. This behavior likely resulted from the effect of deflagrative heat release on the rates of auto-ignition, possibly due to a modified thermal distribution in the end-gas. The case with the highest O_2 fraction exhibited the longest burn duration despite faster initial heat release rates from flame propagation. Estimated laminar flame speeds near the time of spark were shown to increase with O_2 fraction despite a decrease in T_u. This increase in flame speed was likely due to both an increased T_b (caused by a lower mixture c_p) as well as increased chemical reaction rates due to an elevated O_2 concentration. Thermal efficiency and NO_x emissions were shown to increase for a higher O_2 fraction, possibly due to increased γ and T_b, respectively.

Chapter 6

Conclusions, Contributions, and Suggestions for Future Work

6.1 Summary and Conclusions

In this thesis, multi-mode SACI combustion was used to 'bridge the gap' between highly dilute HCCI auto-ignition and near stoichiometric SI flame propagation. Preheated flames at dilution levels up to $\sim$55% were initiated with a spark event, and the relatively slower charge consumption rates of these flames (compared to auto-ignition) caused significant increases in overall burn duration compared to pure HCCI combustion. The increase in burn duration allowed load to be substantially increased while complying with cylinder pressure rise rate limitations. Spark assist also offered more robust control over the phasing of largely auto-igniting combustion without the need to change the initial state at IVC, as in HCCI. The results indicate the potential for increased controllability (via spark) with multi-mode operation, as well as increased flexibility in initial conditions without compromising engine performance.

Overall SACI burn rates and peak rates of heat release were substantially modified at a constant combustion phasing, fueling rate, and charge dilution level by controlling the thermodynamic state of the mixture at the time of spark, thereby modifying the initial flame based heat release rates and the timing of auto-ignition. Variations in unburned gas temperature near the time of spark were counteracted by changes in spark advance and overall EGR rates to maintain constant combustion phasing. Initial burn rates were consistent with

the theoretical behavior of laminar flames as engine conditions varied. Auto-ignition was shown to be initiated primarily via compression heating from the expanding flame front - for a lower initial unburned gas temperature, a larger fraction of flame based heat release was required to initiate auto-ignition. Additionally, auto-ignition burn rates were found to be affected by the percentage of deflagrative heat release, possibly due to increased thermal stratification in the end-gas resulting from flame consumption of the hot core charge.

6.1.1 Chapter 3 Summary and Conclusions

In Chapter 3, load extension into the SACI regime was accomplished using a combination of spark assist, internal EGR, and cooled external EGR to control pressure rise rates at a given fueling level. The engine was operated unheated and naturally-aspirated at a constant engine speed of 2000 rpm. The study showed that efficient dilute SACI combustion could be achieved at loads substantially above the allowable limits for naturally-aspirated HCCI by controlling overall burn rates at constant combustion phasing.

The engine was first mapped in lean HCCI mode, and fueling was steadily increased until the high load ringing/instability limit of combustion was reached at $\sim$3.7 bar $IMEP_n$. At each load condition, combustion was phased by changing the initial state at IVC through the addition or removal of internal residual via NVO. Load extension was achieved using spark assist and EGR dilution at a stoichiometric 'fuel-to-air' equivalence ratio ($\phi = 1.0$). The high dilution levels caused maximum in-cylinder temperatures to remain relatively low, increasing γ and allowing for more efficient operation than conventional SI at the same load conditions. Within the SACI regime, a maximum load of $\sim$7.5 bar $IMEP_n$ was achieved. At these elevated load conditions, the high compression ratio (12.5:1) of the engine created problems with end-gas knock. Retarding the spark in an attempt to mitigate this phenomenon only resulted in unstable combustion, and decreasing the effective compression ratio through late IVC led to a reduction in $IMEP_n$. The ringing intensity correlation of Eng (Eq. 2.33) was inappropriate for quantifying the knocking intensity at these

high load SACI conditions, and better metrics should be developed in order to potentially operate closer to the mechanical knock limit, thereby improving combustion stability.

Within the SACI regime, features of both 'slow' flame propagation and 'fast' auto-ignition heat release were observed. As load increased, unburned gas temperatures were purposely decreased by replacing a portion of the internal EGR (via NVO) with cooled external EGR. A lower T_u caused the end-gas mixture to become less prone to auto-ignition and thus, the fraction of flame based heat release increased, the overall burn duration increased, and the spark was advanced to maintain combustion phasing. NO_x emissions increased significantly at high load SACI conditions, a likely result of increased burned gas temperatures at lower levels of dilution (i.e. higher ϕ'). Although NO_x emissions exceeded U.S. standards throughout most of the SACI regime, conventional after-treatment could be used due to the stoichiometric fuel-air mixture.

At each load condition that was examined ($\phi' = 0.45 - 0.7$), spark advance had a noticeable effect on combustion behavior. As the spark was advanced, the onset of auto-ignition occurred earlier in the cycle and overall burn durations decreased, similar to HCCI. Ringing intensity and NO_x emissions also increased due to higher rates of pressure rise and peak in-cylinder temperatures. Combustion phasing was also modified by varying the ratio of internal to external EGR in-cylinder (thereby adjusting T_u) at a constant spark timing; however, combustion was highly sensitive to this parameter due to its effect on both initial flame propagation rates and auto-ignition delay times. Spark advance offered more robust control over combustion phasing, and this finding increases the potential applicability of SACI (over pure HCCI) in transient engine systems.

6.1.2 Chapter 4 Summary and Conclusions

In Chapter 4, SACI burn rates were modified at constant phasing and fueling rate by varying spark timing and unburned gas temperature (T_u) simultaneously while holding composition approximately constant. In doing so, independent control of burn duration and combustion

phasing was demonstrated, addressing a major shortcoming of low temperature HCCI combustion. As T_u decreased and spark advanced, a larger portion of flame based heat release was seen (a result of the increased compression heating required to promote auto-ignition), contributing to longer 0-90% burn durations. This increase in deflagrative combustion decreased the fuel mass available for auto-ignition, causing a decrease in peak rates of heat release, ringing intensity, and combustion stability.

As T_u (and hence, T_b) decreased, the estimated laminar flame speeds (S_L) at 15° after spark timing decreased as well. This reduction in the initial flame propagation rates correlated well to the increase in the 0-5% mass fraction burned durations. Although turbulence likely affected burn rates in this region, the decrease in laminar flame speed could partially explain the need for advancing the spark at lower unburned temperatures to maintain combustion phasing. By advancing the spark, these 'slower' flames were allowed more time to compress a relatively colder unburned mixture to the point of auto-ignition, thereby increasing overall burn durations. Bulk reactions began at a similar time and unburned gas temperature for every case, regardless of the temperature at spark timing. The cases with the highest fractions of flame based heat release also exhibited the longest 50-90% burn durations. At this point, the primary cause for the increase in the later burn durations is unclear, but enhanced end-gas thermal stratification (on a per mass basis) resulting from increased deflagrative heat release is a possible contributing factor. The flame likely consumes the hottest part of the charge, leaving a larger relative portion of the auto-igniting mixture near the cylinder wall.

By controlling the tradeoff between flame propagation and auto-ignition, ringing intensity and combustion stability were managed for a given load and phasing. With HCCI, large variations in ringing and stability were accomplished by varying the combustion phasing, often at an efficiency cost. For a given load and phasing, overall SACI burn rates do not drastically affect engine performance, provided ringing and stability constraints are met. The fact that SACI burn rates can be controlled at a constant CA50 in order to reduce peak

rates of pressure rise without compromising thermal efficiency is an important conclusion of this study.

These dramatic variations in SACI behavior were caused primarily by changes in spark timing and unburned gas temperature rather than varying levels of mixedness associated with small changes in NVO. Burn rates, ringing, and stability were remarkably similar when internal EGR (via NVO) was replaced with preheated external EGR while holding temperature at IVC, spark timing, CA50, and mixture composition constant. This finding suggested that for the range of NVO used to vary the unburned gas temperature (by $\sim$25 K at IVC) for the spark/T_u sweep, any change in mixing characteristics and thermal/compositional stratification caused by varying valve events had a negligible effect on combustion behavior.

6.1.3 Chapter 5 Summary and Conclusions

In Chapter 5, SACI burn rates were again modified at constant phasing and fueling rate through the simultaneous manipulation of T_u and charge oxygen-to-fuel ratio at a constant spark timing. Similar results to Chapter 4 were seen in that as T_u decreased, a larger fraction of flame based heat release was necessary to promote auto-ignition of a relatively colder unburned mixture. This increase in the portion of deflagrative combustion lead to decreased peak rates of heat release, ringing intensity, and combustion stability.

Despite lower unburned gas temperatures, the initial rates of flame propagation increased with a higher fraction of O_2 in the unreacted mixture. These increased rates of heat release are likely due to both an increase in T_b associated with a lower mixture c_p and an increase in kinetic rates within the flame reaction zone due to the elevated concentration of O_2. Estimated laminar flame speeds (S_L) at 15° after spark ignition correlate inversely to the measured 0-5% burn durations, as was seen in Chapter 4, indicating that laminar flame speeds are likely contributing to the observed behavior in the initial stages of combustion. This S_L dependence is expected to be particularly prominent for this set of data, since the

turbulent flow field should be similar at constant spark advance, NVO, and engine speed.

The faster flames associated with an elevated O_2 fraction compress a relatively colder T_u mixture to the point of auto-ignition ($\sim$1050 K) at approximately the same time as slower flames propagating into a higher T_u mixture. However, the rates of auto-ignition are shown to decrease as T_u decreases and O_2 fraction increases, displaying the opposite behavior as that seen in a similar HCCI experiment. This effect on the rates of auto-ignition (seen in the increased 50-90% burn durations) likely results from variations in the end-gas thermal distribution induced by deflagrative heat release, as discussed previously. This effect, in addition to rapid rates of piston expansion, increases the overall burn duration for the case with the highest O_2 fraction despite the fact that this case also has the fastest initial rates of flame propagation.

With this set of data, as in Chapter 4, ringing intensity and combustion stability were managed for a given load and phasing. Thermal efficiency appeared to improve slightly (1-2% absolute) as the O_2 fraction increased, likely due to an increase in mixture γ. However, NO_x emissions also increased fourfold, bringing into question the potential of O_2 dilution for improving controllability and thermal efficiency in a practical engine system. Based on the high cost of lean NO_x after-treatment, SACI engines will likely be operated at globally stoichiometric conditions, as the associated penalty in net thermal efficiency is relatively minor.

6.2 Contributions

With multi-mode combustion, the rates of flame propagation and auto-ignition affect overall burn durations, pressure rise rates, and peak rates of heat release. The successful demonstration of SACI burn rate management through the simultaneous change of only two engine variables is an important contribution of this work. These studies are some of the only examples in the world to demonstrate a high level of range and control of low temperature

combustion in an I.C. engine. Additional important contributions are listed below.

- The SACI studies demonstrated a tradeoff between deflagration and auto-ignition heat release, which was affected by the thermophysical properties of the mixture in a manner consistent with theroetical kinetics. Thus, the hypothesis that SACI is essentially two distinct energy release events coupled by the compression heating from an expanding flame front was validated by the results of this work. Furthermore, the distinct characteristics of auto-ignition and flame propagation were applied to improve overall combustion performance relative to conventional spark-ignition.

- A novel experimental method for extending load into the SACI regime and 'bridging the dilution gap' between HCCI and SI was developed and demonstrated using the advanced features of the research engine. Burn rates were controlled through careful manipulation of spark advance, internal EGR rates (via NVO), and external EGR rates at a given fueling level. The usable load range was doubled compared to pure HCCI combustion while maintaining high thermal efficiency, representing an unprecedented improvement in naturally-aspirated HCCI engine performance.

- New experimental methods were developed for manipulating the burn rates of SACI combustion at a constant phasing (CA50), thus addressing a major shortcoming of conventional HCCI combustion. Control parameters included spark timing, unburned gas temperature, and total EGR rate. These results provided insight into the practical operating range of SACI combustion at constant ϕ' and phasing.

- The effects of thermal/compositional stratification due to NVO variation on SACI burn rates was isolated using a unique experimental approach. Results indicated that burn rates were dominated by the turbulence-flame interactions and the thermal properties of the mixture.

- The composition of the diluent mixture was shown to have a dramatic effect on SACI

burn rates. This is the first study of its kind to directly compare these effects within an engine setting.

- The results indicate the potential to expand the methods used in this work to affect combustion rates through the strategic use of turbulence and flame/auto-ignition combustion chemistry. Such methods are applicable beyond the SACI conditions studied in this work.

6.3 Recommendations for Future Work

This thesis focused on metal engine experiments to gain insight into the SACI combustion processes. These experiments were valuable and informative, and they provide direction for further experimental and computational work that can isolate the important governing mechanisms of SACI. Future work should focus on the following aspects of SACI combustion: (a) quantifying flame kernel development and flame propagation rates at dilute, high temperature conditions, (b) understanding the effects of thermal and compositional stratification on flame propagation and auto-ignition over the broad range of conditions expected during HCCI, SACI, and other advanced low temperature combustion strategies, and (c) understanding flammability limits with respect to overall dilution rates, mixture composition (i.e. air vs. EGR dilution), and turbulence levels.

Optical engine experiments and computational models will be helpful for understanding the initial stages of SACI combustion, including flame kernel formation and turbulent flow interactions at the start of SACI flame propagation. Engine models can be used in determining the local conditions in the vicinity of the spark plug, including temperature and mixture composition, in order to more accurately estimate initial laminar flame speeds. These S_L values can then be compared to the early turbulent burning velocities measured in optical engines, before noticeable heat release is observed. Engine models can also be used to estimate the local turbulent length and time scales to provide further insight into

the trends in initial flame propagation rates.

Optical engine access will also be crucial for understanding the effects of deflagrative heat release on the local onset of auto-ignition and rates of bulk heat release. Optical measurement techniques and engine models can be used to quantify the local conditions at the onset of auto-ignition and the level of thermal stratification in the end-gas as a result of deflagrative heat release. These results can then be compared to the results in Chapters 4 and 5 pertaining to end-gas auto-ignition to better understand the dominant mechanisms governing the rates of auto-ignition. A detailed comparison of optical engine data and measured rates of heat release for a variety of conditions could also lead to the development of an improved metric for determining the 'onset' of auto-ignition based on the *RoHR*.

A more focused study of the effects of thermal/compositional stratification on low temperature combustion could be performed using various methods of mixture preparation. One such method could involve varying the NVO over a larger range than that shown in Chapter 4. Despite the fact that a less than 30° CA change in NVO appeared to have no effect on the rates of SACI combustion, it is possible that a larger change in NVO could affect the behavior of flame propagation and/or auto-ignition. In order to accomplish a study of this nature, greater intake charge heating capabilities will be required to compensate for the large NVO variation. This experiment could also be repeated for pure HCCI combustion to ascertain if HCCI is more or less affected by changes in thermal/compositional stratification than SACI.

As was seen in Chapter 3, the spark continues to affect combustion phasing as ϕ' decreases, even though auto-ignition becomes the dominant mode of combustion. Studies by other researchers (discussed in Chapter 1) have shown that with ultra-dilute mixtures ($\phi' < 0.4$), the spark has a reduced effect on combustion phasing; however, these studies were inconsistent based on the method of dilution (with air or EGR). To gain a better understanding of the SACI flame limiting behavior, an experiment can be performed in which the sensitivity of a given mixture (diluted with various combinations of air and/or EGR at

$\phi' \leq 0.4$) to a change in spark advance is quantified. The results of Middleton et al. [89] suggests that EGR dilute mixtures are less likely to respond to changes in spark advance at low engine loads than mixtures with equivalent amounts of air dilution. In addition, it is possible that dilute flame limits are affected by the level of in-cylinder turbulence, which varies with engine speed. These hypotheses have yet to be investigated experimentally.

Practical implementation of low temperature combustion is still greatly inhibited by a lack of controllability. While spark assist increases the level of combustion control, transient engine operation remains the primary challenge of HCCI and SACI. While the technology for implementing such advanced combustion strategies currently exists, future efforts must focus on advancing engine control algorithms so that multi-mode production engines can become a reality.

Bibliography

[1] R. H. Thring. "Homogeneous-Charge Compression-Ignition (HCCI) Engines". *SAE Technical Paper 892068*. 1989. DOI: 10.4271/892068.

[2] S. Onishi, S. H. Jo, K. Shoda, P. D. Jo, and S. Kato. "Active Thermo-Atmosphere Combustion (ATAC) - A New Combustion Process for Internal Combustion Engines". *SAE Technical Paper 790501*. 1979. DOI: 10.4271/790501.

[3] J.-O. Olsson, P. Tunestål, G. Haraldsson, and B. Johansson. "A Turbo Charged Dual Fuel HCCI Engine". *SAE Technical Paper 2001-01-1896*. 2001. DOI: 10.4271/2001-01-1896.

[4] B. Johansson. "Cycle to Cycle Variations in S.I. Engines - The Effects of Fluid Flow and Gas Composition in the Vicinity of the Spark Plug on Early Combustion". *SAE Technical Paper 962084*. 1996. DOI: 10.4271/962084.

[5] M. Christensen, B. Johansson, P. Amnéus, and F. Mauss. "Supercharged Homogeneous Charge Compression Ignition". *SAE Technical Paper 980787*. 1998. DOI: 10.4271/980787.

[6] A. Cairns and H. Blaxill. "The Effects of Combined Internal and External Exhaust Gas Recirculation on Gasoline Controlled Auto-Ignition". *SAE Technical Paper 2005-01-0133*. 2005. DOI: 10.4271/2005-01-0133.

[7] J. E. Dec. "A Computational Study of the Effects of Low Fuel Loading and EGR on Heat Release Rates and Combustion Limits in HCCI Engines". *SAE Technical Paper 2002-01-1309*. 2002. DOI: 10.4271/2002-01-1309.

[8] J. T. Farrell, J. G. Stevens, and W. Weissman. "A Second Law Analysis of High Efficiency Low Emission Gasoline Engine Concepts". *SAE Technical Paper 2006-01-0491*. 2006. DOI: 10.4271/2006-01-0491.

[9] J. B. Heywood. *Internal Combustion Engine Fundamentals*. New York: McGraw-Hill, 1988.

[10] M. Christensen, B. Johansson, and P. Einewall. "Homogeneous Charge Compression Ignition (HCCI) Using Isooctane, Ethanol and Natural Gas - A Comparison with Spark Ignition Operation". *SAE Technical Paper 972874*. 1997. DOI: 10.4271/972874.

[11] J. E. Dec, M. Sjöberg, and W. Hwang. "Isolating the Effects of EGR on HCCI Heat-Release Rates and NOx Emissions". *SAE Technical Paper 2009-01-2665*. 2009. DOI: 10.4271/2009-01-2665.

[12] J. Lavy, J.-C. Dabadie, C. Angelberger, P. Duret, J. Willand, A. Juretzka, J. Schaflein, T. Ma, Y. Lendresse, A. Satre, C. Schulz, H. Krämer, H. Zhao, and L. Damiano. "Innovative Ultra-low NOx Controlled Auto-Ignition Combustion Process for Gasoline Engines: the 4-SPACE Project". *SAE Technical Paper 2000-01-1837*. 2000. DOI: 10.4271/2000-01-1837.

[13] M. Noguchi, Y. Tanaka, T. Tanaka, and Y. Takeuchi. "A Study on Gasoline Engine Combustion by Observation of Intermediate Reactive Products during Combustion". *SAE Technical Paper 790840*. 1979. DOI: 10.4271/790840.

[14] P. M. Najt and D. E. Foster. "Compression-Ignited Homogeneous Charge Combustion". *SAE Technical Paper 830264*. 1983. DOI: 10.4271/830264.

[15] J. Willand, R.-G. Nieberding, G. Vent, and C. Enderle. "The Knocking Syndrome - Its Cure and Its Potential". *SAE Technical Paper 982483*. 1998. DOI: 10.4271/982483.

[16] A. Hultqvist, M. Christensen, B. Johansson, M. Richter, J. Nygren, J. Hult, and M. Aldjn. "The HCCI Combustion Process in a Single Cycle - Speed Fuel Tracer LIF and Chemiluminescence Imaging". *SAE Technical Paper 2002-01-0424*. 2002. DOI: 10.4271/2002-01-0424.

[17] J. E. Dec, W. Hwang, and M. Sjöberg. "An Investigation of Thermal Stratification in HCCI Engines Using Chemiluminescence Imaging". *SAE Technical Paper 2006-01-1518*. 2006. DOI: 10.4271/2006-01-1518.

[18] S. B. Fiveland and D. N. Assanis. "A Four-Stroke Homogeneous Charge Compression Ignition Engine Simulation for Combustion and Performance Studies". *SAE Technical Paper 2000-01-0332*. 2000. DOI: 10.4271/2000-01-0332.

[19] A. Kulzer, A. Christ, M. Rauscher, C. Sauer, G. Würfel, and T. Blank. "Thermodynamic Analysis and Benchmark of Various Gasoline Combustion Concepts". *SAE Technical Paper 2006-01-0231*. 2006. DOI: 10.4271/2006-01-0231.

[20] M. Sjöberg and J. E. Dec. "An Investigation of the Relationship Between Measured Intake Temperature, BDC Temperature, and Combustion Phasing for Premixed and DI HCCI Engines". *SAE Technical Paper 2004-01-1900*. 2004. DOI: 10.4271/2004-01-1900.

[21] H. Zhao, J. Li, T. Ma, and N. Ladommatos. "Performance and Analysis of a 4-Stroke Multi-Cylinder Gasoline Engine with CAI Combustion". *SAE Technical Paper 2002-01-0420*. 2002. DOI: 10.4271/2002-01-0420.

[22] H. Persson, M. Agrell, J.-O. Olsson, B. Johansson, and H. Ström. "The Effect of Intake Temperature on HCCI Operation Using Negative Valve Overlap". *SAE Technical Paper 2004-01-0944*. 2004. DOI: 10.4271/2004-01-0944.

[23] J. A. Eng. "Characterization of Pressure Waves in HCCI Combustion". *SAE Technical Paper 2002-01-2859*. 2002. DOI: 10.4271/2002-01-2859.

[24] D. Flowers, S. Aceves, R. Smith, J. Torres, J. Girard, and R. Dibble. "HCCI in a CFR Engine: Experiments and Detailed Kinetic Modeling". *SAE Technical Paper 2000-01-0328*. 2000. DOI: 10.4271/2000-01-0328.

[25] J.-O. Olsson, P. Tunestål, B. Johansson, S. Fiveland, R. Agama, M. Willi, and D. Assanis. "Compression Ratio Influence on Maximum Load of a Natural Gas Fueled HCCI Engine". *SAE Technical Paper 2002-01-0111*. 2002. DOI: 10.4271/2002-01-0111.

[26] D. A. Rothamer, J. A. Snyder, R. K. Hanson, R. R. Steeper, and R. P. Fitzgerald. "Simultaneous imaging of exhaust gas residuals and temperature during HCCI combustion". *Proceedings of the Combustion Institute* 32 (2009), 2869–2876. DOI: 10.1016/j.proci.2008.07.018.

[27] A. Babajimopoulos, D. N. Assanis, and S. B. Fiveland. "An Approach for Modeling the Effects of Gas Exchange Processes on HCCI Combustion and Its Application in Evaluating Variable Valve Timing Control Strategies". *SAE Technical Paper 2002-01-2829*. 2002. DOI: 10.4271/2002-01-2829.

[28] T. Amano, S. Morimoto, and Y. Kawabata. "Modeling of the Effect of Air/Fuel Ratio and Temperature Distribution on HCCI Engines". *SAE Technical Paper 2001-01-1024*. 2001. DOI: 10.4271/2001-01-1024.

[29] L. M. Olesky, J. Vavra, D. Assanis, and A. Babajimopoulos. "Effects of Charge Preheating Methods on the Combustion Phasing Limitations of an HCCI Engine With Negative Valve Overlap". *Journal of Engineering for Gas Turbines and Power* 34 (2012), 112801. DOI: 10.1115/1.4007319.

[30] M. Sjöberg, J. E. Dec, A. Babajimopoulos, and D. Assanis. "Comparing Enhanced Natural Thermal Stratification Against Retarded Combustion Phasing for Smoothing of HCCI Heat-Release Rates". *SAE Technical Paper 2004-01-2994*. 2004. DOI: 10.4271/2004-01-2994.

[31] E. Hellström, J. Larimore, A. Stefanopoulou, J. Sterniak, and L. Jiang. "Quantifying Cyclic Variability in a Multicylinder HCCI Engine With High Residuals". *Journal of Engineering for Gas Turbines and Power* 34 (2012), 112803. DOI: 10.1115/1.4007164.

[32] L. Koopmans, O. Backlund, and I. Denbratt. "Cycle to Cycle Variations: Their Influence on Cycle Resolved Gas Temperature and Unburned Hydrocarbons from a Camless Gasoline Compression Ignition Engine". *SAE Technical Paper 2002-01-0110*. 2002. DOI: 10.4271/2002-01-0110.

[33] J.-O. Olsson, P. Tunestål, J. Ulfvik, and B. Johansson. "The Effect of Cooled EGR on Emissions and Performance of a Turbocharged HCCI Engine". *SAE Technical Paper 2003-01-0743*. 2003. DOI: 10.4271/2003-01-0743.

[34] T. W. Ryan and T. J. Callahan. "Homogeneous Charge Compression Ignition of Diesel Fuel". *SAE Technical Paper 961160*. 1996. DOI: 10.4271/961160.

[35] J. E. Dec and Y. Yang. "Boosted HCCI for High Power without Engine Knock and with Ultra-Low NOx Emissions - using Conventional Gasoline". *SAE International Journal of Engines* 3 (2010), 750–767. DOI: 10.4271/2010-01-1086.

[36] L. Manofsky, J. Vavra, D. Assanis, and A. Babajimopoulos. “Bridging the Gap between HCCI and SI: Spark-Assisted Compression Ignition”. *SAE Technical Paper 2011-01-1179*. 2011. DOI: 10.4271/2011-01-1179.

[37] H. Persson, R. Pfeiffer, A. Hultqvist, B. Johansson, and H. Ström. “Cylinder-to-Cylinder and Cycle-to-Cycle Variations at HCCI Operation With Trapped Residuals”. *SAE Technical Paper 2005-01-0130*. 2005. DOI: 10.4271/2005-01-0130.

[38] J. Allen and D. Law. “Variable Valve Actuated Controlled Auto-Ignition: Speed Load Maps and Strategic Regimes of Operation”. *SAE Technical Paper 2002-01-0422*. 2002. DOI: 10.4271/2002-01-0422.

[39] M. Sjöberg and J. E. Dec. “An investigation into lowest acceptable combustion temperatures for hydrocarbon fuels in HCCI engines”. *Proceedings of the Combustion Institute* 30 (2005), 2719–2726. DOI: 10.1016/j.proci.2004.08.132.

[40] J. Hyvönen, G. Haraldsson, and B. Johansson. “Supercharging HCCI to Extend the Operating Range in a Multi-Cylinder VCR-HCCI Engine”. *SAE Technical Paper 2003-01-3214*. 2003. DOI: 10.4271/2003-01-3214.

[41] J.-O. Olsson, P. Tunestål, and B. Johansson. “Boosting for High Load HCCI”. *SAE Technical Paper 2004-01-0940*. 2004. DOI: 10.4271/2004-01-0940.

[42] T. Aroonsrisopon, P. Werner, J. O. Waldman, V. Sohm, D. E. Foster, T. Morikawa, and M. Iida. “Expanding the HCCI Operation With the Charge Stratification”. *SAE Technical Paper 2005-01-1756*. 2004. DOI: 10.4271/2004-01-1756.

[43] T. Urushihara, K. Yamaguchi, K. Yoshizawa, and T. Itoh. “A Study of a Gasoline-fueled Compression Ignition Engine - Expansion of HCCI Operation Range Using SI Combustion as a Trigger of Compression Ignition”. *SAE Technical Paper 2005-01-0180*. 2005. DOI: 10.4271/2005-01-0180.

[44] J. Hiltner, S. Fiveland, R. Agama, and M. Willi. “System Efficiency Issues for Natural Gas Fueled HCCI Engines in Heavy-Duty Stationary Applications”. *SAE Technical Paper 2002-01-0417*. 2002. DOI: 10.4271/2002-01-0417.

[45] P. W. Bessonette, C. H. Schleyer, K. P. Duffy, W. L. Hardy, and M. P. Liechty. “Effects of Fuel Property Changes on Heavy-Duty HCCI Combustion”. *SAE Technical Paper 2007-01-0191*. 2007. DOI: 10.4271/2007-01-0191.

[46] B. T. Zigler, P. E. Keros, K. B. Helleberg, M. Fatouraie, D. Assanis, and M. Wooldridge. “An experimental investigation of the sensitivity of the ignition and combustion properties of a single-cylinder research engine to spark-assisted HCCI”. *International Journal and Engine Research* 12 (2011), 353–375. DOI: 10.1177/1468087411401286.

[47] H. Persson, A. Hultqvist, B. Johansson, and A. Remón. “Investigation of the Early Flame Development in Spark Assisted HCCI Combustion Using High Speed Chemiluminescence Imaging”. *SAE Technical Paper 2007-01-0212*. 2007. DOI: 10.4271/2007-01-0212.

[48] D. L. Reuss, T.-W. Kuo, G. Silvas, V. Natarajan, and V. Sick. "Experimental metrics for identifying origins of combustion variability during spark-assisted compression ignition". *International Journal and Engine Research* 9 (2008), 409–434. DOI: 10.1243/14680874JER01108.

[49] G. A. Lavoie, J. Martz, M. Wooldridge, and D. Assanis. "A multi-mode combustion diagram for spark assisted compression ignition". *Combustion and Flame* 157 (2010), 1106–1110. DOI: 10.1016/j.combustflame.2010.02.009.

[50] H. Yun, N. Wermuth, and P. Najt. "Extending the High Load Operating Limit of a Naturally-Aspirated Gasoline HCCI Combustion Engine". *SAE International Journal of Engines* 3 (2010), 681–699. DOI: 10.4271/2010-01-0847.

[51] J. P. Szybist, E. Nafziger, and A. Weall. "Load Expansion of Stoichiometric HCCI Using Spark Assist and Hydraulic Valve Actuation". *SAE International Journal of Engines* 3 (2010), 244–258. DOI: 10.4271/2010-01-2172.

[52] H. Yun, N. Wermuth, and P. Najt. "High Load HCCI Operation Using Different Valving Strategies in a Naturally-Aspirated Gasoline HCCI Engine". *SAE International Journal of Engines* 4 (2011), 1190–1201. DOI: 10.4271/2011-01-0899.

[53] Z. Wang, J.-X. Wang, S.-J. Shuai, G.-H. Tian, X. An, and Q.-J. Ma. "Study of the effect of spark ignition on gasoline HCCI combustion". *Proceedings of the Institution of Mechanical Engineers, Part D: Journal of Automobile Engineering* 220 (2006), 817–825. DOI: 10.1243/09544070JAUTO151.

[54] J. Hyvönen, G. Haraldsson, and B. Johansson. "Operating Conditions Using Spark Assisted HCCI Combustion During Combustion Mode Transfer to SI in a Multi-Cylinder VCR-HCCI Engine". *SAE Technical Paper 2005-01-0109*. 2005. DOI: 10.4271/2005-01-0109.

[55] Y. Huang, C. J. Sung, and J. A. Eng. "Dilution limits of n-butane/air mixtures under conditions relevant to HCCI combustion". *Combustion and Flame* 136 (2004), 457–466. DOI: 10.1016/j.combustflame.2003.10.011.

[56] J. B. Martz, R. J. Middleton, G. A. Lavoie, A. Babajimopoulos, and D. N. Assanis. "A computational study and correlation of premixed isooctane–air laminar reaction front properties under spark ignited and spark assisted compression ignition engine conditions". *Combustion and Flame* 158 (2011), 1089–1096. DOI: 10.1016/j.combustflame.2010.09.014.

[57] A. Quader. "What Limits Lean Operation in Spark Ignition Engines-Flame Initiation or Propagation?" *SAE Technical Paper 760760*. 1976. DOI: 10.4271/760760.

[58] Z. Wang, J.-X. Wang, S.-J. Shuai, and Q.-J. Ma. "Effects of Spark Ignition and Stratified Charge on Gasoline HCCI Combustion With Direct Injection". *SAE Technical Paper 2005-01-0137*. 2005. DOI: 10.4271/2005-01-0137.

[59] M. Weinrotter, E. Wintner, K. Iskra, T. Neger, J. Olofsson, H. Seyfried, M. Aldén, M. Lackner, F. Winter, A. Vressner, A. Hultqvist, and B. Johansson. "Optical Diagnostics of Laser-Induced and Spark Plug-Assisted HCCI Combustion". *SAE Technical Paper 2005-01-0129*. 2005. DOI: 10.4271/2005-01-0129.

[60] H. Kopecek, E. Wintner, M. Lackner, F. Winter, and A. Hultqvist. “Laser-Stimulated Ignition in a Homogeneous Charge Compression Ignition Engine”. *SAE Technical Paper 2004-01-0937*. 2004. DOI: 10.4271/2004-01-0937.

[61] P. F. Flynn, G. L. Hunter, R. P. Durrett, L. A. Farrell, and W. C. Akinyemi. “Minimum Engine Flame Temperature Impacts on Diesel and Spark-Ignition Engine NOx Production”. *SAE Technical Paper 2000-01-1177*. 2000. DOI: 10.4271/2000-01-1177.

[62] G. A. Lavoie and P. N. Blumberg. “Measurements of NO Emissions From a Stratified Charge Engine: Comparison of Theory and Experiment”. *Combustion Science and Technology* 8 (1973), 25–37. DOI: 10.1080/00102207308946628.

[63] X. He, M. T. Donovan, B. T. Zigler, T. R. Palmer, S. M. Walton, M. S. Wooldridge, and A. Atreya. “An experimental and modeling study of iso-octane ignition delay times under homogeneous charge compression ignition conditions”. *Combustion and Flame* 142 (2005), 266–275. DOI: 10.1016/j.combustflame.2005.02.014.

[64] R. M. Wagner, K. D. Edwards, C. S. Daw, J. B. Green, and B. G. Bunting. “On the Nature of Cyclic Dispersion in Spark Assisted HCCI Combustion”. *SAE Technical Paper 2006-01-0418*. 2006. DOI: 10.4271/2006-01-0418.

[65] G. Lavoie, E. Ortiz-Soto, A. Babajimopoulos, J. B. Martz, and D. N. Assanis. “Thermodynamic sweet spot for high-efficiency, dilute, boosted gasoline engines”. *International Journal of Engine Research* (2012). DOI: 10.1177/1468087412455372.

[66] W. Dai, S. G. Russ, N. Trigui, and K. V. Tallio. “Regimes of Premixed Turbulent Combustion and Misfire Modeling in SI Engines”. *SAE Technical Paper 982611*. 1998. DOI: 10.4271/982611.

[67] A. Buschmann, F. Dinkelacker, T. Schäfer, M. Schäfer, and J. Wolfrum. “Measurement of the instantaneous detailed flame structure in turbulent premixed combustion”. *Symposium (International) on Combustion* 26 (1996), 437–445. DOI: 10.1016/S0082-0784(96)80246-3.

[68] A. Soika, F. Dinkelacker, and A. Leipertz. “Measurement of the resolved flame structure of turbulent premixed flames with constant reynolds number and varied stoichiometry”. *Symposium (International) on Combustion* 27 (1998), 785–792. DOI: 10.1016/S0082-0784(98)80473-6.

[69] J. F. Driscoll. “Turbulent premixed combustion: Flamelet structure and its effect on turbulent burning velocities”. *Progress in Energy and Combustion Science* 34 (2008), 91–134. DOI: 10.1016/j.pecs.2007.04.002.

[70] S. A. Filatyev, J. F. Driscoll, C. D. Carter, and J. M. Donbar. “Measured properties of turbulent premixed flames for model assessment, including burning velocities, stretch rates, and surface densities”. *Combustion and Flame* 141 (2005), 1–21. DOI: 10.1016/j.combustflame.2004.07.010.

[71] A. Ratner, J. F. Driscoll, J. M. Donbar, C. D. Carter, and J.A. Mullin. "Reaction zone structure of non-premixed turbulent flames in the "intensely wrinkled" regime". *Proceedings of the Combustion Institute* 28 (2000), 245–252. DOI: 10.1016/S0082-0784(00)80217-9.

[72] W. L. Roberts, J. F. Driscoll, M. C. Drake, and L. P. Goss. "Images of the quenching of a flame by a vortex - To quantify regimes of turbulent combustion". *Combustion and Flame* 94 (1993), 58–69. DOI: 10.1016/0010-2180(93)90019-Y.

[73] P. G. Aleiferis, A. M. K. P. Taylor, K. Ishii, and Y. Urata. "The nature of early flame development in a lean-burn stratified-charge spark-ignition engine". *Combustion and Flame* 136 (2004), 283–302. DOI: 10.1016/j.combustflame.2003.08.011.

[74] B. Zigler. "An experimental investigation of the ignition properties of low temperature combustion in an optical engine". Ph.D. Thesis. The University of Michigan, Ann Arbor, 2008.

[75] L. Koopmans and I. Denbratt. "A Four Stroke Camless Engine, Operated in Homogeneous Charge Compression Ignition Mode with Commercial Gasoline". *SAE Technical Paper 2001-01-3610*. 2001. DOI: 10.4271/2001-01-3610.

[76] D. L. Stivender. "Development of a Fuel-Based Mass Emission Measurement Procedure". *SAE Technical Paper 710604*. 1971. DOI: 10.4271/710604.

[77] G. J. Patterson and R. S. Davis. "Geometric and Topological Considerations to Maximize Remotely Mounted Cylinder Pressure Transducer Data Quality". *SAE International Journal of Engines* 2 (2009), 414–420. DOI: 10.4271/2009-01-0644.

[78] E. Ortiz-Soto. "A Comprehensive Heat Release Analysis Framework for Experimental Research and Model Development of Advanced Combustion Engines". In preparation. 2012.

[79] R. P. Fitzgerald, R. Steeper, J. Snyder, R. Hanson, and R. Hessel. "Determination of Cycle Temperatures and Residual Gas Fraction for HCCI Negative Valve Overlap Operation". *SAE International Journal of Engines* 3 (2010), 124–141. DOI: 10.4271/2010-01-0343.

[80] *NIST-JANAF Thermochemical Tables*. 2000. URL: http://kinetics.nist.gov/janaf/.

[81] A. Burcat. *Prof. Burcat's Thermodynamic Data*. 2006. URL: http://garfield.chem.elte.hu/Burcat/burcat.html.

[82] J. Brettschneider. "Berechnung des luftverhaeltnisses lambda von luft-krarftstoffgemischen und des einflusses von messfehler auf lambda (Calculation of the air ratio lambda of air fuel mixtures and its effect on measurement errors)". *Bosch Technische Berichte* 6 (1979), 177–186.

[83] E. A. Ortiz-Soto, J. Vavra, and A. Babajimopoulos. "Assessment of Residual Mass Estimation Methods for Cylinder Pressure Heat Release Analysis of HCCI Engines With Negative Valve Overlap". *Journal of Engineering for Gas Turbines and Power* 134 (2012), 082802. DOI: 10.1115/1.4006701.

[84] H. J. Yun and W. Mirsky. “Schlieren-Streak Measurements of Instantaneous Exhaust Gas Velocities from a Spark-Ignition Engine”. *SAE Technical Paper 741015*. 1974. DOI: 10.4271/741015.

[85] G. Woschni. “A Universally Applicable Equation for the Instantaneous Heat Transfer Coefficient in the Internal Combustion Engine”. *SAE Technical Paper 670931*. 1967. DOI: 10.4271/670931.

[86] J. Chang, O. Güralp, Z. Filipi, D. Assanis, T.-W. Kuo, P. Najt, and R. Rask. “New Heat Transfer Correlation for an HCCI Engine Derived from Measurements of Instantaneous Surface Heat Flux”. *SAE Technical Paper 2004-01-2996*. 2004. DOI: 10.4271/2004-01-2996.

[87] G. F. Hohenberg. “Advanced Approaches for Heat Transfer Calculations”. *SAE Technical Paper 790825*. 1979. DOI: 10.4271/790825.

[88] G. Eichelberg. “Some New Investigations on Old Combustion Engine Problems”. *Engineering* 148 (1939), 446–463.

[89] R. J. Middleton, J. B. Martz, G. A. Lavoie, A. Babajimopoulos, and D. Assanis. “A computational study and correlation of premixed isooctane air laminar reaction fronts diluted with EGR”. *Combustion and Flame* 159 (2012), 3146–3157. DOI: 10.1016/j.combustflame.2012.04.014.

[90] J. B. Martz, G. A. Lavoie, H. G. Im, R. J. Middleton, A. Babajimopoulos, and D. N. Assanis. “The propagation of a laminar reaction front during end-gas autoignition”. *Combustion and Flame* 159 (2012), 2077–2086. DOI: 10.1016/j.combustflame.2012.01.011.

[91] J. B. Martz, H. Kwak, H. G. Im, G. A. Lavoie, and D. N. Assanis. “Combustion regime of a reacting front propagating into an auto-igniting mixture”. *Proceedings of the Combustion Institute* 33 (2011), 3001–3006. DOI: 10.1016/j.proci.2010.07.040.

[92] P. G. Aleiferis, J. Serras-Pereira, and D. Richardson. “Characterisation of flame development with ethanol, butanol, *iso*-octane, gasoline and methane in a direct-injection spark-ignition engine”. *Fuel* In Press (2013). DOI: 10.1016/j.fuel.2012.12.088.

[93] M. Metghalchi and J. C. Keck. “Burning velocities of mixtures of air with methanol, isooctane, and indolene at high pressure and temperature”. *Combustion and Flame* 48 (1982), 191–210. DOI: 10.1016/0010-2180(82)90127-4.

[94] S. P. Marshall, S. Taylor, C. R. Stone, T. J. Davies, and R. F. Cracknell. “Laminar burning velocity measurements of liquid fuels at elevated pressures and temperatures with combustion residuals”. *Combustion and Flame* 158 (2011), 1920–1932. DOI: 10.1016/j.combustflame.2011.02.016.

[95] S. Jerzembeck, N. Peters, P. Pepiot-Desjardins, and H. Pitsch. “Laminar burning velocities at high pressure for primary reference fuels and gasoline: Experimental and numerical investigation”. *Combustion and Flame* 156 (2009), 292–301. DOI: 10.1016/j.combustflame.2008.11.009.

[96] D. Bradley, R. A. Hicks, M. Lawes, C. G. W. Sheppard, and R. Woolley. "The Measurement of Laminar Burning Velocities and Markstein Numbers for Iso-octane–Air and Iso-octane–n-Heptane–Air Mixtures at Elevated Temperatures and Pressures in an Explosion Bomb". *Combustion and Flame* 115 (1998), 126–144. DOI: 10.1016/S0010-2180(97)00349-0.

[97] J. T. Farrell, R. J. Johnston, and I. P. Androulakis. "Molecular Structure Effects On Laminar Burning Velocities At Elevated Temperature And Pressure". *SAE Technical Paper 2004-01-2936*. 2004. DOI: 10.4271/2004-01-2936.

[98] A. Babajimopoulos, D. N. Assanis, D. L. Flowers, S. M. Aceves, and R. P. Hessel. "A fully coupled computational fluid dynamics and multi-zone model with detailed chemical kinetics for the simulation of premixed charge compression ignition engines". *International Journal of Engine Research* 6 (2005), 497–512. DOI: 10.1243/146808705X30503.

[99] K. Kumar, J. E. Freeh, C. J. Sung, and Y. Huang. "Laminar Flame Speeds of Preheated iso-Octane/O_2/N_2 and n-Heptane/O_2/N_2 Mixtures". *Journal of Propulsion and Power* 23 (2007), 428–436. DOI: 10.2514/1.24391.

[100] D. Bradley, P. H. Gaskell, X. J. Gu, M. Lawes, and M. J. Scott. "Premixed turbulent flame instability and NO formation in a lean-burn swirl burner". *Combustion and Flame* 115 (1998), 515–538. DOI: 10.1016/S0010-2180(98)00024-8.

[101] M. Sjöberg and J. E. Dec. "Influence of Fuel Autoignition Reactivity on the High-Load Limits of HCCI Engines". *SAE International Journal of Engines* 1 (2008), 39–58. DOI: 10.4271/2008-01-0054.

[102] A. J. Weall and J. P. Szybist. "The Effects of Fuel Characteristics on Stoichiometric Spark-Assisted HCCI". *Journal of Engineering for Gas Turbines and Power* 134 (2012), 072805. DOI: 10.1115/1.4006007.

[103] Z. Wang, J. Wang, S. Shuai, X. He, F. Xu, D. Yang, and X. Ma. "Research on Spark Induced Compression Ignition (SICI)". *SAE Technical Paper 2009-01-0132*. 2009. DOI: 10.4271/2009-01-0132.

[104] N. Kalian, H. Zhao, and C. Yang. "Effects of spark-assistance on controlled auto-ignition combustion at different injection timings in a multicylinder direct-injection gasoline engine". *International Journal of Engine Research* 10 (2009), 133–148. DOI: 10.1243/14680874JER03209.

[105] T. Tsurushima, E. Kunishima, Y. Asaumi, Y. Aoyagi, and Y. Enomoto. "The Effect of Knock on Heat Loss in Homogeneous Charge Compression Ignition Engines". *SAE Technical Paper 2002-01-0108*. 2002. DOI: 10.4271/2002-01-0108.

[106] P. F. Flynn, G. L. Hunter, L. Farrel, R. P. Durrett, O. Akinyemi, A. O. Zur Loye, C. K. Westbrook, and W. J. Pitz. "The inevitability of engine-out NO_x emissions from spark-ignited and diesel engines". *Proceedings of the Combustion Institute* 28 (2000), 1211–1218. DOI: 10.1016/S0082-0784(00)80332-X.

[107] J. Vavra, S. V. Bohac, L. Manofsky, G. Lavoie, and D. Assanis. “Knock In Various Combustion Modes in a Gasoline-Fueled Automotive Engine”. *Journal of Engineering for Gas Turbines and Power* 134 (2012), 082807. DOI: 10.1115/1.4006694.

[108] E. W. Kaiser, J. Yang, T. Culp, N. Xu, and M. M. Maricq. “Homogeneous charge compression ignition engine-out emission - does flame propagation occur in homogeneous charge compression ignition?” *International Journal of Engine Research* 3 (2002), 185–195. DOI: 10.1243/146808702762230897.

[109] Z. Wang, X. He, J.-X. Wang, S. Shuai, F. Xu, and D. Yang. “Combustion visualization and experimental study on spark induced compression ignition (SICI) in gasoline HCCI engines”. *Energy Conversion and Management* 51 (2010), 908–917. DOI: 10.1016/j.enconman.2009.11.029.

[110] H. Shen and D. Jiang. “Investigation on the Flame Initiation and Early Development in a Spark Ignition Engine”. *SAE Technical Paper 922239*. 1992. DOI: 10.4271/922239.

[111] R. Herweg and G. F. W. Ziegler. “Flame kernel formation in a spark-ignition engine”. *Proceedings of the 2nd International Symposium on Diagnostics and Modeling of Combustion in Internal Combustion Engines (COMODIA)*. (Kyoto, Sept. 3–5, 1990). Vol. 90. 1990, 173–178.

[112] R. Herweg and R. R. Maly. “A Fundamental Model for Flame Kernel Formation in S. I. Engines”. *SAE Technical Paper 922243*. 1992. DOI: 10.4271/922243.

[113] H. Shen, P. C. Hinze, and J. B. Heywood. “A Model for Flame Initiation and Early Development in SI Engine and its Application to Cycle-to-Cycle Variations”. *SAE Technical Paper 942049*. 1994. DOI: 10.4271/942049.

[114] C. K. Law. *Combustion Physics*. New York: Cambridge University Press, 2006.

[115] L. M. Olesky, J. B. Martz, G. A. Lavoie, J. Vavra, D. N. Assanis, and A. Babajimopoulos. “The effects of spark timing, unburned gas temperature, and negative valve overlap on the rates of stoichiometric spark assisted compression ignition combustion”. *Applied Energy* 105 (2013), 407–417. DOI: 10.1016/j.apenergy.2013.01.038.

[116] D. Bradley. “How fast can we burn?” *Symposium (International) on Combustion* 24 (1992), 247–262. DOI: 10.1016/S0082-0784(06)80034-2.

[117] J. B. Martz. “Simulation and Model Development for Auto-Ignition and Reaction Front Propagation in Low-Temperature High-Pressure Lean-Burn Engines”. Ph.D. Thesis. The University of Michigan, Ann Arbor, 2010.

[118] C. K. Westbrook. “Prediction of laminar flame properties of methanol-air mixtures”. *Combustion and Flame* 37 (1980), 171–192. DOI: 10.1016/0010-2180(80)90084-X.

[119] H. J. Curran, P. Gaffuri, W. J. Pitz, and C. K. Westbrook. “A comprehensive modeling study of iso-octane oxidation”. *Combustion and Flame* 129 (2002), 253–280. DOI: 10.1016/S0010-2180(01)00373-X.

[120] C. K. Westbrook. “Numerical modeling of ethylene oxidation in laminar flames”. *Combustion and Flame* 52 (1983), 299–313. DOI: 10.1016/0010-2180(83)90140-2.

[121] G. A. Lavoie, J. B. Heywood, and J. C. Keck. “Experimental and Theoretical Study of Nitric Oxide Formation in Internal Combustion Engines”. *Combustion Science and Technology* 1 (1970), 313–326.